Title
High Resolution Optical Characterization of Graphene Functionalization

Author
Li, Yunqi

Publication Date
2022

Peer reviewed|Thesis/dissertation

High Resolution Optical Characterization of Graphene Functionalization

by

Yunqi Li

A dissertation submitted in partial satisfaction of the

requirements for the degree of

Doctor of Philosophy

in

Chemistry

in the

Graduate Division

of the

University of California, Berkeley

Committee in charge:

Professor Ke Xu, Chair
Professor Junqiao Wu
Professor Naomi Ginsberg

Fall 2022

Abstract

High Resolution Optical Characterization of Graphene Functionalization

by

Yunqi Li

Doctor of Philosophy in Chemistry

University of California, Berkeley

Professor Ke Xu, Chair

The past decades have witnessed the exponential growth of studies utilizing optical techniques to characterize graphene functionalization. The promise and potential application of graphene and related materials are substantially expanded through chemical functionalization. However, due to the fact that graphene is a single layer of carbon atoms, it is difficult to study the *in situ* dynamics of graphene chemistry. Moreover, the inertness of the graphene basal plane has notably limited its viable chemical modification pathways. This dissertation describes efforts by the author and colleagues to overcome these limitations. Part I of this dissertation demonstrates the direct optical visualization of *in situ* dynamics of graphene chemistry through interference reflection microscopy. Specifically, we uncover the unique dynamics of the redox reaction, diazonium reaction and solution-enclosing blister generation process of substrate-supported graphene at high spatiotemporal resolution. Part II of this dissertation reports facile approaches to the chemical modifications of the inert graphene basal plane under ambient conditions. Optical characterizations techniques including interference reflection microscopy, transmission microscopy, fluorescence microscopy, and Raman spectroscopy are utilized here to help establish the successful modifications of graphene through our facile approaches. These approaches include direct azidation and chlorination of the graphene basal plane through the electrochemical oxidation of an aqueous sodium azide and sodium chloride solution as well as a photocatalytic approach for the facile azidation and chemical patterning of graphene surface.

Table of Contents

List of Figures

Acknowledgements

I am deeply grateful to my incredible advisor Prof. Ke Xu, who has been such a supportive and inspiring mentor throughout my whole PhD program. He has guided and supported me every step of the way in my PhD studies. My thanks also go to all the colleagues I have encountered in the Xu lab. Their kindness and welcome helped me settled into the lab quickly. I really appreciate the help from Dr. Wan Li and Dr. Michal Wojcik, who have collaborated and guided me on many of the projects I have been involved in. I also want to thank my family and friends for being there for me when I needed them.

Introduction

In 2004, two physics, Andre Geim and Konstantin Novoselov first extracted graphene from a piece of graphite. Using regular adhesive tape they managed to obtain a flake of one atom thick graphene, for which they received the Nobel Prize in 2010. In simple terms, graphene is a sheet of a single layer of carbon atoms, tightly bound in a hexagonal honeycomb lattice. Graphene is the strongest compound discovered, the best conductor of heat at room temperature, and also the best conductor of electricity known. Graphene's outstanding electrical, optical, and mechanical properties makes it a potential candidate in application areas including electronics and biosensors. The potential of graphene can be substantially expanded through chemistry. However, the facts that graphene is a single layer of atom and graphene uniformly absorbs 2.3% of light across the visible and near-infrared parts of the spectrum create difficulty for its *in situ* studies. Existing techniques offer limited signal contrast and/or spatial-temporal resolution, and are difficult to apply to *in situ* studies.

In part I of this dissertation, we demonstrate the direct optical visualization of *in situ* dynamics of graphene chemistry through interference reflection microscopy (IRM). IRM is a facile, label-free optical microscopy method originated in cell biology. By repurposing IRM for imaging graphene, we experimentally achieved excellent contrast. IRM was performed on a standard inverted fluorescence microscope equipped with a standard lamp, a field diaphragm, a bandpass filter and a 50/50 beam splitter. The incident single color light enters the sample from the substrate side and encounters the graphene and top medium. The IRM signal is based on the absorption and interference of light at the sample.

By employing IRM, we first quantitatively monitor the redox reaction dynamics of graphene and graphene oxide (GO) *in situ* with diffraction-limited (~300 nm) spatial resolution and video-rate time resolution. Remarkably, we found that the oxidation kinetics of graphene are characterized by a seeded, autocatalytic process that gives rise to unique, wave-like propagation of the reaction in two dimensions. The reaction is initially slow and confined to highly localized, nanoscale hot spots associated with structural defects, but then self-accelerates while propagating outwards, hence flower-like, micrometer-sized reaction patterns over the entire sample. In contrast, the reduction of GO is spatially homogeneous and temporally pseudo-first-order, and through *in situ* data we further identify pH as a key reaction parameter.

We next apply IRM to study the *in situ* reaction dynamics of the representative diazonium reaction of graphene with 4-nitrobenzenediazonium tetrafluoroborate (4-NBD) at high spatiotemporal resolution, and further correlate results with atomic force microscopy, Raman spectroscopy, and infrared scattering scanning near-field optical microscopy. Interestingly, we find the reaction to be significantly promoted by a low (0.5 W/cm^2) level of blue visible light, whereas at the same intensity level, red light has negligible effects on reaction rate. We further report rich spatial heterogeneities for the reaction, including enhanced reactivity at graphene edges and an unexpected flake-to-flake variation in reaction rate. Moreover, we demonstrate direct photo-patterning for the 4-NBD functionalization, achieving 400 nm patterning resolution.

The fast, spontaneous generation of solution-enclosing blisters/bubbles for monolayer and few-layer graphene on common silicon and glass substrates in acidic solutions is another system

illustrating that IRM is a powerful tool for direct optical visualization of *in situ* dynamics of graphene chemistry. Using IRM, we monitor the blister-generating process *in situ*, and show that at pH<~2, nanoscale to micrometer-sized graphene blisters, up to ~100 nm in height, are universally generated with high surface coverages on hydrophilic, but not hydrophobic, surfaces. The spontaneously generated blisters are highly dynamic, with growth, merging, and reconfiguration occurring at second-to-minute time scales. Moreover, we show that in this dynamic system, graphene behaves as a semipermeable membrane that allows the relatively free passing of water, impeded passing of the NaCl solute, and no passing of large dye molecules. Consequently, the blister volumes can be fast and reversibly modulated by the solution osmotic pressure.

In part II of this dissertation, we shift the focus from direct optical visualization and *in situ* dynamics to discussions of facile chemical modifications of graphene under ambient conditions. It has become clear over the past decade that the full potential of graphene and related materials can only be released through chemical functionalization and modification. However, the basal plane of graphene is notoriously inert; limited approaches are available for its covalent chemistry, and they often cannot be done in a controlled fashion. In this section, we report facile approaches of covalent functionalization of graphene basal plane, which are successfully characterized by several optical methods including IRM, transmission microscopy, fluorescence microscopy, and Raman spectroscopy and X-ray photoelectron spectrum.

We first report direct azidation and subsequent click chemistry of the graphene basal plane through the electrochemical oxidation of an aqueous sodium azide solution at the graphene surface. A ~20% nitrogen-to-carbon ratio is achieved for monolayer graphene under ambient conditions and neutral pH, and the degree of functionalization is tunable through the applied voltage. The functionalized azide groups enable both copper-catalyzed and copper-free alkyne cycloaddition click chemistry, as well as subsequent bioconjugation, and fluorescence microscopy indicates uniform functionalization across the graphene surface. Notably, we find that as the azidation, cycloaddition, and bioconjugation processes substantially shift the graphene doping level, high electrical conductivity and carrier mobility are maintained throughout the different functionalization states. By integrating the electrochemical azidation scheme with electrochemical exfoliation, we further demonstrate one-step bulk production of azidated graphene flakes from graphite.

In contrast to the traditional toxic and corrosive methods to graphene chlorination, we report a facile approach to directly chlorinate graphene from an aqueous sodium chloride solution under ambient conditions. By applying a moderate anodic voltage to substrate-supported monolayer graphene, the resultant chlorine radicals generated at the graphene surface enable efficient chlorination: the X-ray photoelectron spectrum confirms the formation of C-Cl bonds, and reaction voltage-tunable Cl:C atomic ratios of up to 17% are achieved. In comparison, we find the corresponding electrochemical graphene bromination and iodination reactions much less viable. Electrical and Raman characterizations show substantial *p*-doping for the chlorinated graphene, yet good basal-plane integrity and electrical properties are maintained. Interference reflection microscopy and pH-dependent experiments next help elucidate the competition between the radical-mediated electrochemical chlorination and oxidation in the process, and rationalize acidic conditions for optimal chlorination. Reaction in a mixed NaCl-NaN_3 solution shows the electrochemical

chlorination to be fully suppressed by azidation, yet a sequential, two-step chlorination-azidation approach permits facile bi-functionalization.

The past few years have seen focused interest in the chemical patterning of graphene. However, tightly focused laser beams are used to achieve the required high local light intensity, and spatial patterning was then performed by scanning the focused beam. Such approaches are both technically challenging and of very low throughput. To overcome these limitations, we report a photocatalytic approach for the facile azidation and chemical patterning of graphene. Employing the classic photoredox catalysis tris(bipyridine)ruthenium(II) chloride $[Ru(bpy)_3]Cl_2$, azidyl radicals are generated in an aqueous solution of sodium azide under low illumination of blue light, *e.g.*, filtered out from a white lamp. The photogenerated azidyl radicals efficiently azidate monolayer graphene, and the resultant azidated graphene further enables chemically defined derivations through click chemistry and subsequent bioconjugation. By controlling the illumination pattern in the wide field, we further demonstrate the direct photopatterning of graphene functionalization with low light, removing the need to focus an intense laser beam into a tight spot.

Publications reproduced in this dissertation are listed below. Permission has been granted by all critical co-authors for the reproduction of the work in this dissertation.

M. Wojcik[||]*, Y. Li*[||]*, W. Li, K. Xu, "Spatially resolved in situ reaction dynamics of graphene via optical microscopy," J. Am. Chem. Soc.,* ***139****, 5836-5841, 2017.*

Y. Li, W. Li, M. Wojcik, B. Wang, L.-C. Lin, M. B. Raschke, K. Xu, "Light-assisted diazonium functionalization of graphene and spatial heterogeneities in reactivity," J. Phys. Chem. Lett., ***10****, 4788-4793, 2019.*

Y. Li, B. Wang, W. Li, K. Xu, "Dynamic, spontaneous blistering of substrate-supported graphene in acidic solutions," ACS Nano, ***16****, 6145-6152, 2022.*

W. Li, Y. Li, K. Xu, "Azidated graphene: direct azidation from monolayers, click chemistry, and bulk production from graphite," Nano Lett., ***20****, 534-539, 2020.*

W. Li, Y. Li, K. Xu, "Facile, electrochemical chlorination of graphene from an aqueous NaCl solution," Nano Lett., ***21****, 1150-1155, 2021.*

W. Li[||]*, Y. Li*[||]*, B. Wang, K. Xu, "Visible-Light Azidation and Chemical Patterning of Graphene via Photoredox Catalysis," J. Phys. Chem. (in press), 2022.*

[||] denotes equal contribution.

Part I: Direct optical visualization of in situ dynamics of graphene chemistry via interference reflection microscopy

In this section, we demonstrate the direct optical visualization of *in situ* dynamics of graphene chemistry through interference reflection microscopy (IRM),[1-4] a label-free optical technique. We start with utilizing IRM to uncover the unique, spatially and temporally highly heterogeneous redox reaction dynamics of graphene and GO since the IRM signal heavily depends on the complex index of refraction of the sample. As this method is also sensitive to the thickness of the thin film material, we then apply IRM to study the *in situ* dynamics of the representative diazonium reaction of graphene with 4-nitrobenzenediazonium tetrafluoroborate (4-NBD) [5-13] at high spatiotemporal resolution. The fast, spontaneous blister-generating process of substrate-supported graphene in acidic solutions of pH<~2 is another system that elucidates IRM as a strong tool for *in situ* imaging and dynamic measurements.

Chapter 1: Spatially resolved in situ reaction dynamics of graphene oxidation and GO reduction

The work in this chapter was conducted in collaboration with Michal Wojcik, Wan Li and Ke Xu. It is reproduced in part here from ref[14] with permission from all co-authors.

1.1 Introduction

Graphene and its derivatives have attracted broad research and commercial interests over the past decade for their exceptional electrical, optical, and mechanical properties.[16,17] The promise of graphene can be substantially expanded through chemistry: chemical modifications provide pathways to the fine-tuning of bandgaps, and chemical functionalization enables new applications.[18-25] Meanwhile, chemical reduction of graphene oxide (GO) provides a promising route to graphene mass production.[18,26,27] Moreover, understanding the chemical reactivity of graphene on substrates is critical to establishing the performance limitations of graphene-based devices.

The fact that graphene is a single layer of carbon atoms creates challenges for studying its reaction dynamics. X-ray photoelectron spectroscopy (XPS) provides elemental compositions and chemical states,[28-30] but offers no spatial information and is limited by ultrahigh vacuum operating conditions. Raman spectroscopy provides an accessible means to study the doping and defect levels of the graphene lattice,[31] and thus an indirect way to probe reaction progress.[8,10,29,30,32-35] However, the absolute progression of reaction is difficult to quantify, limited spatial and temporal resolutions are achieved, and *in situ* application to solution-phase reactions[34] is difficult. Scanning electrochemical microscopy maps out local reactivity in solutions,[36-38] but reports on the reactions of solute molecules at the graphene surface as opposed to the reactions of graphene *per se*.

In this chapter, we attained spatially resolved, *in situ* redox reaction dynamics of graphene and GO on common glass substrates through IRM.

1.2 Results and discussion

IRM signal is based on the interference of light at the sample[4] (Figure 1a), which depends strongly on the complex index of refraction of the sample, n_2 (Figure 1b). Consequently, IRM should be sensitive to changes in local chemical compositions, as long as associated changes in index of refraction exist. Specifically, for the chemical conversion between monolayer graphene (n_2 = 2.65+1.27i)[39,40] and GO (n_2 = 1.75+0.17i),[41] the theoretical contrast I/I_0 (I and I_0 being the IRM signal at the sample vs. at a bare substrate, respectively) is 0.70−0.73 for the former and 0.97 for the latter (Figure 1b) when the top medium is an aqueous solution (n_3 = 1.355−1.330). This ~30% signal difference is readily detectable. By performing video-rate IRM recording of graphene and GO under the immersion of a solution-phase oxidizing/reducing agent, we thus achieved quantitative, spatially resolved recording of the dynamics of graphene redox reactions *in situ*.

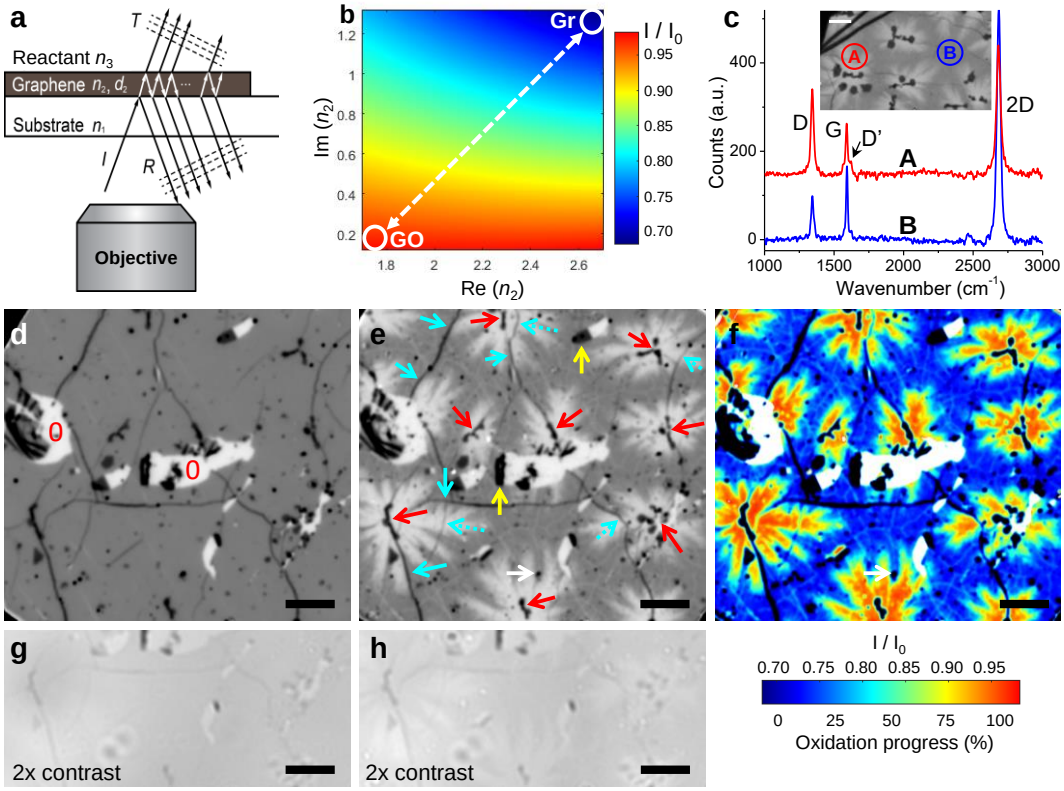

Figure 1. IRM reveals spatially inhomogeneous oxidation of graphene. (a) Schematic of IRM. The complex indices of refraction are denoted as n_1, n_2, and n_3 for the substrate, graphene sample, and reactant solution, respectively. (b) Theoretical IRM signal (I/I_0) for monolayers of different complex n_2 values. Circles mark values corresponding to pristine graphene (Gr) and GO. (c) Raman spectroscopy of graphene after 1 h oxidation in Clorox, taken close to (Spot A) and far away from (Spot B) centers of the flower-like patterns visualized by IRM (inset), respectively. (d,e) IRM images of graphene on glass, before (d) and after (e) 1 h oxidation in Clorox. "0"s mark areas with no graphene. (f) Result of (e) converted to oxidation progress map (color-scale bar below). (g,h) Conventional transmission light microscopy of the bottom half of the same areas as (d,e), with 2x artificial enhancement of image contrast. Scale bars: 5 μm.

We first examined the oxidation of copper-grown graphene[42] that was wet-transferred[42,43] onto glass, using household bleach Clorox as the oxidant. Experimental IRM signal of the starting graphene monolayer (Figure 1d) gave $I/I_0 = 0.71$, in agreement with theory. After 1 h of oxidation, micrometer-sized flower-like patterns appeared with significantly increased local intensity in IRM signal (Figure 1e), consistent with the predicted signal change for GO (Figure 1b). In comparison, conventional transmission light microscopy achieved only 2% contrast for graphene[44-46] (Figure 1g), and after reaction barely discerned the flower-like patterns as brighter areas (Figure 1h), attributable to the much lower light absorption of GO when compared to graphene.[41] Raman spectroscopy showed a stronger D peak, the appearance of a D' peak, and a reduced 2D peak for areas close to the flower-like patterns (Figures 1c and 2), indicating greater local reaction progresses.[8,10,32-35] XPS results showed ~20% graphene oxidation for samples similarly prepared on a silicon substrate (Figure 2), consistent with the observed reaction patterns.

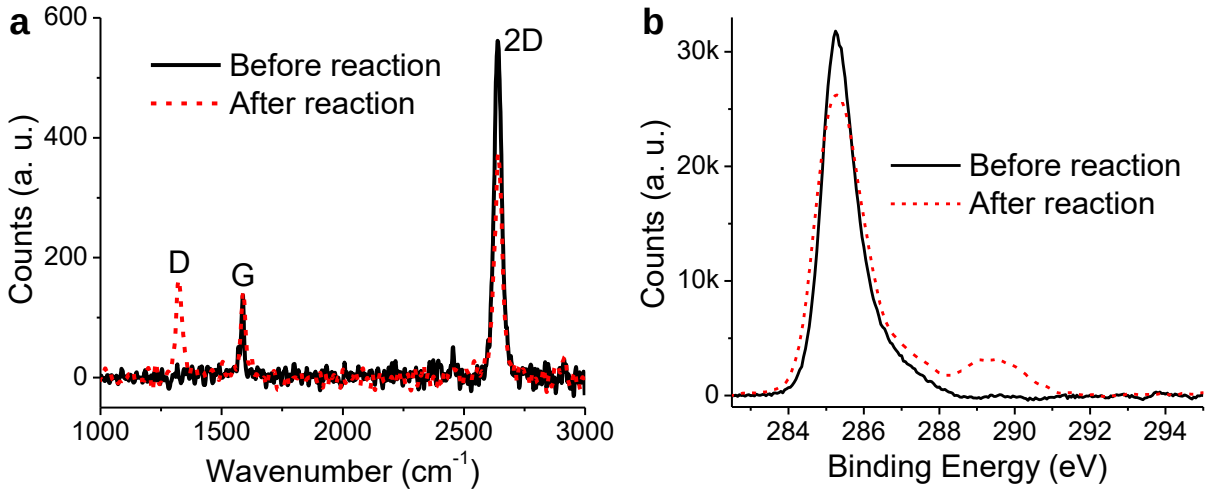

Figure 2. Raman spectroscopy and X-ray photoelectron spectroscopy (XPS) of graphene samples before (black) and after (red) 1 h oxidation in Clorox. (a) Raman spectroscopy: a significant increase in D peak and a decrease in 2D peak were observed after reaction. Here spectra were averaged from eight random locations of the sample, thus included areas close to and far away from reaction centers (Figure 1c). (b) XPS data show the appearance of a significant peak at ~289 eV, an increase in the shoulder peak at ~286 eV, and a decrease in the original peak at ~285 eV after reaction. These results are in general agreement with previous results on partial oxidation of graphene,[15] and we estimate ~20% of the graphene surface to be oxidized, consistent with the reaction patterns observed by IRM. Note that for the XPS experiments, conductive silicon substrates were used in lieu of the glass substrates used in all other experiments, so as to eliminate sample charging.

The excellent IRM contrast offers a possibility to quantify local reaction progress. As IRM achieves diffraction-limited spatial resolution of ~300 nm,[4] its signal is the local average of the contrast from graphene and GO within the diffraction-limited spot, and so is linearly dependent on the local fraction of GO. We thus directly converted the measured I/I_0 into a map of the local GO percentage and thus the oxidation progress (Figure 1f). As shown below, this treatment allows for good descriptions of both reaction progress and dynamics.

The reaction progress map (Figure 1f) revealed notable spatial heterogeneity. The reaction progress was near 100% in the central areas of each flower-like pattern, but gradually decreased to a lower extent towards the outer areas, with areas far away from the flower-like patterns remaining largely unreacted. This result suggests that the oxidation initiates from certain locations and propagates in the two-dimensional system.

The high sensitivity of IRM for nanoscale defects[4] enabled us to identify the reaction-initiation centers as nanoscale bilayers formed during graphene growth (red arrows in Figure 1e). Stacked bilayers, e.g., those formed due to local tearing and folding-over of monolayers (yellow arrows in Figure 1e), were not reaction centers, suggesting that it is not the presence of bilayers, but rather local defects that seeds the reaction hot spots: It is likely that these local defects also initiated the growth of the second layer in the first place. Edges of graphene were generally not reaction-initiation centers, an observation in line with earlier results on gas-phase oxidation of graphene.[32]

This result suggests that the oxidation of graphene is guided by different dynamics compared to electrochemical reactions of solute molecules at the graphene surface.[36-38] Wrinkles in graphene were also not reaction-initiation centers. Remarkably, the more prominent wrinkles apparently blocked the propagation of reaction in the two-dimensional graphene sheet (solid cyan arrows in Figure 1e), whereas the lesser wrinkles were less effective in blocking reaction propagation (dashed cyan arrows). AFM results indicate that the more prominent wrinkles are ~1 nm in height, whereas the lesser wrinkles visualized by IRM are difficult to probe with AFM due to surface roughness.[4]

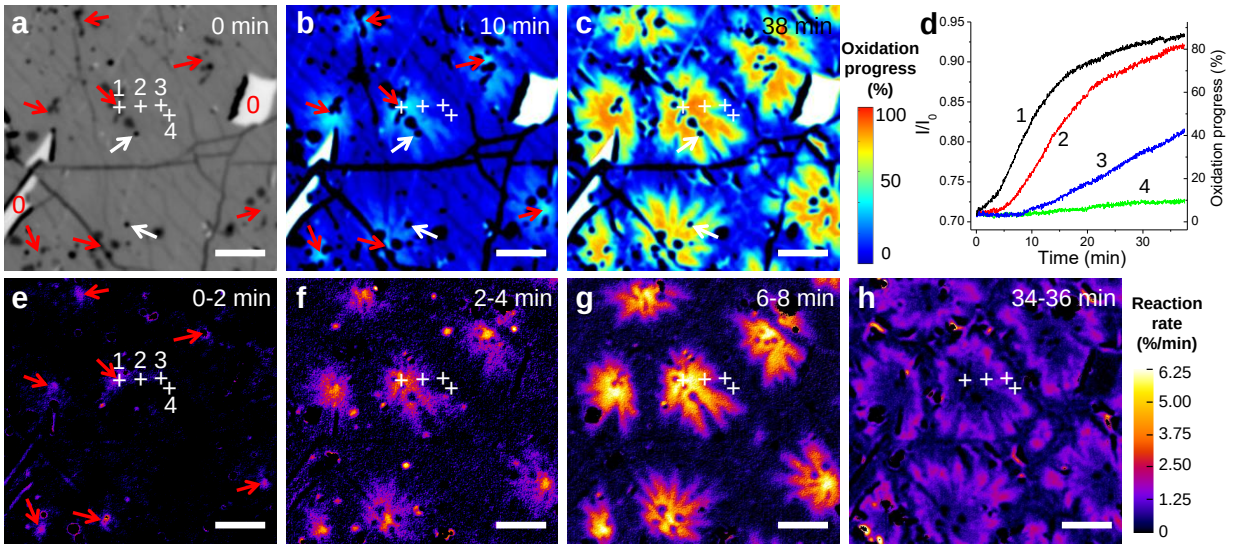

Figure 3. *In situ* recording of the oxidation kinetics of graphene. (a) IRM image of the starting monolayer graphene. "0" marks an area with no graphene coverage. (b,c) IRM-derived oxidation progress map of the same area after 10 min (b) and 38 min (c) reaction with Clorox. (d) IRM signal (left axis) and the converted oxidation progress (right axis) as a function of time for the four pixels marked as 1−4 in (a-c, e-h). (e-h) Map of local reaction rates, obtained by calculating the slopes of reaction progress of every pixel during the time frame indicated in each figure. Red arrows in (a,b,e) point to reaction-initiation centers. Scale bars: 5 µm.

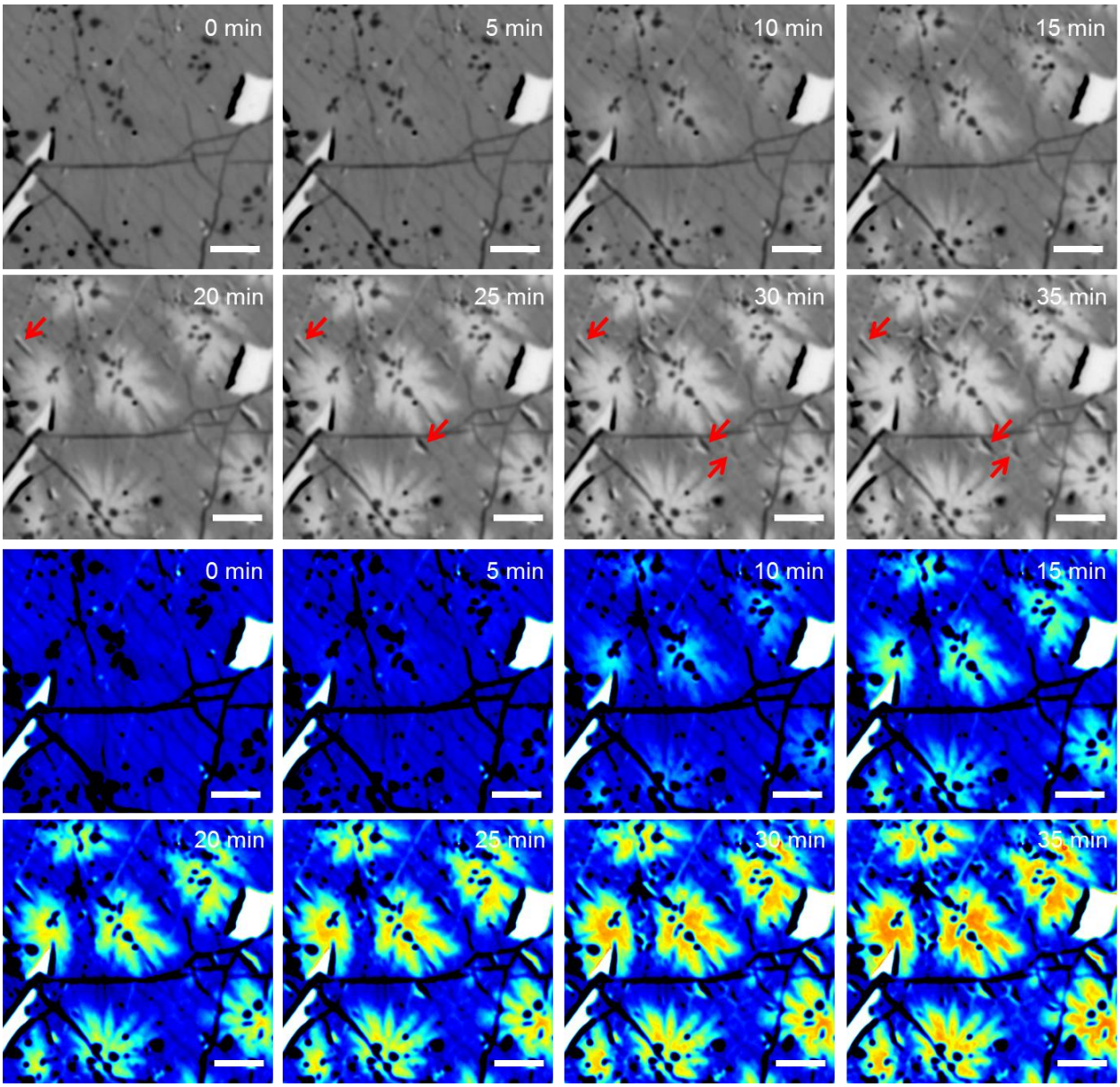

Figure 4. Additional IRM images (top two rows) and corresponding converted oxidation progress maps (bottom two rows) for the sample shown in Figure 3 at different time points. Color scale for oxidation progress is the same as Figure 3bc. Scale bars: 5 μm. Red arrows point to microscopic tears/cracks generated during the reaction. Most tears/cracks are formed along preexisting wrinkles, attributable to local mechanical instability.[29]

To understand the kinetics of how the reaction propagates in this unique two-dimensional system, we performed *in situ* IRM recording of the reaction in real time (Figures 3 and 4). After 10 min of reaction, notable local oxidation was apparent close to hot spots surrounding nanoscale bilayers (Figure 3ab). The reaction continued at these initiation centers while propagating in two dimensions, thus forming flower-like patterns with greater reaction progress at the center (Figure 3c). The formation of microscopic tears/cracks was also occasionally observed (Figure 4), attributable to tension/strain generated from the reaction. Plotting the reaction progress for different positions as a function of time (Figure 3d for Pixels 1-4 marked in Figure 3a-c) showed

sigmoidal dependence with initially low reaction rates, acceleration at different time points, and reduced rate as the reaction approaches completion.

To visualize the apparent heterogeneity in reaction rate over both space and time, we calculated and color-mapped the local reaction rate at every pixel of the image from the slopes of single-pixel reaction progress curves (e.g., Figure 3d) at different time points (Figure 3e-h). Remarkably, at the onset of the reaction, finite (~2%/min) reaction rates were observed at highly confined local hot spots in the vicinity of local bilayers (red arrows in Figure 3e; also Curve 1 in Figure 3d). The initial reaction quickly propagated in the two-dimensional system (Figure 3f); meanwhile, the reaction rates at the initiation centers accelerated and reached maxima of ~6%/min at 6-8 minutes (Figure 3g).

The initially slow, but later accelerating reactions at the initiation centers are characteristic of autocatalytic reactions. Defects at bilayers apparently act as initial seeds of reaction; as the reaction progresses, more defects are locally created to promote further reaction. Areas surrounding these initiation centers initially lack defects to start the reaction, and so "wait" for periods of varied lengths (Curves 2, 3 in Figure 3d; Figure 3e-h) for the reaction-induced defects to propagate to their locations to seed the reaction. As the locally available reaction sites are consumed, reaction rates start to drop, hence the sigmoidal local reaction progress curves and a peculiar "wavefront" of reaction rate at the edges of the flower patterns at later time points (Figure 3h). This unique reaction propagation mechanism of the two-dimensional graphene system is reminiscent of two-dimensional crystal growth at nucleation sites, although our mechanism involves a gradual progression of local reactions and defects as opposed to rapid crystallization.

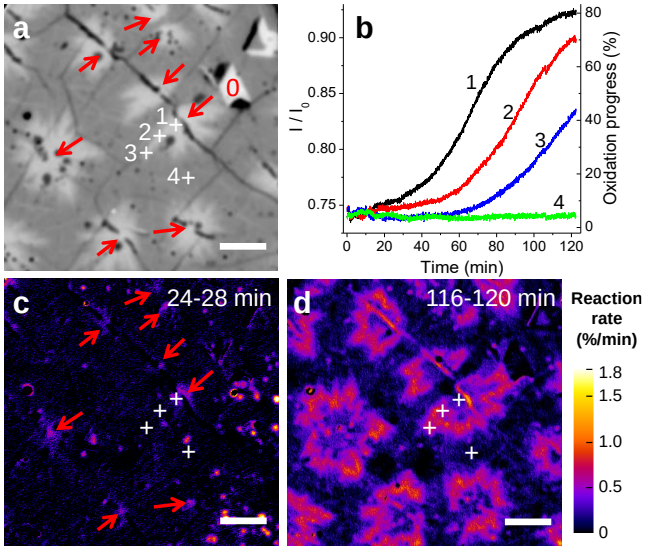

Figure 5. Reaction kinetics with a diluted oxidant. (a) IRM image of monolayer graphene after 2 h oxidation by 10% Clorox. (b) IRM-monitored oxidation progression as a function of time for the four pixels marked as 1−4 in (a). (c,d**)**, Map of local reaction rate for 24-28 min (c) and 116-120 min (d), respectively. Red arrows in (a,c) point to reaction-initiation centers. Scale bars: 5 μm.

We observed similar reaction mechanisms for diluted (10%) Clorox, but noting significantly lower reaction rates (Figure 5). Finite reaction rates were only detected after ~20 min, again first at highly

confined local hot spots in the vicinity of bilayers (Figure 5c), indicating a much slower autocatalytic process. Slower propagation and prolonged delay time were observed across the sample (Figure 5b-d).

Together, these results show that the oxidation kinetics of graphene is characterized by an oxidant concentration-dependent autocatalytic process that results in wave-like propagation of reaction in two dimensions.

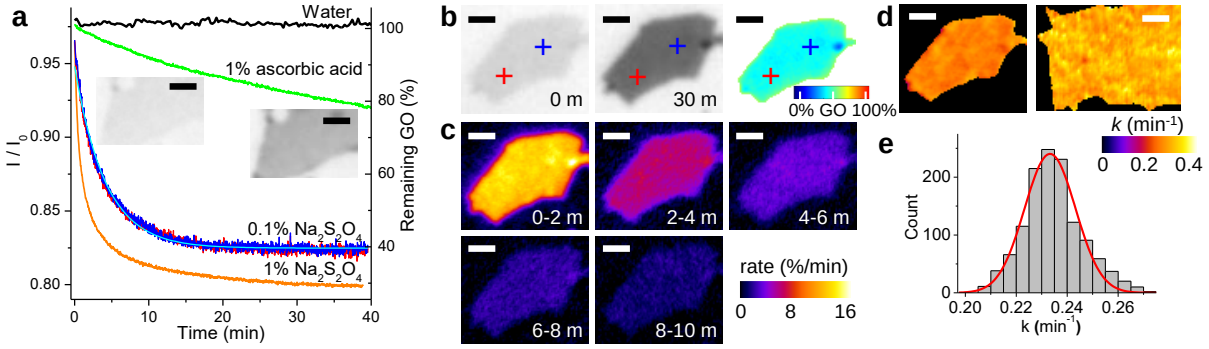

Figure 6. *In situ* recording of the reduction kinetics of GO. (a) IRM signal (left axis) and the converted reaction progress (right axis) for the reduction of GO with a 1% solution of ascorbic acid and 0.1% and 1% solutions of $Na_2S_2O_4$. Result in water is shown for comparison. The 0.1% $Na_2S_2O_4$ data (red and blue) were drawn for two different pixels marked in (b). Other time traces are given as local (~0.1 μm^2) averages. Cyan line is fit to the 0.1% $Na_2S_2O_4$ data to a simple exponential decay. Insets: IRM images of a GO flake before and after 40 min reduction in 1% ascorbic acid. (b) IRM images of a GO flake before (left) and after (center) 30 min reduction in 0.1% $Na_2S_2O_4$, together with the converted map of remaining GO at 30 min (right). (c) Maps of local reaction rates of the same sample at 0–2, 2–4, 4–6, 6–8, and 8–10 min, respectively. (d) Maps of the local first-order reaction rate constant k in 0.1% (left) and 1% (right) $Na_2S_2O_4$, respectively, obtained by fitting the reaction time trace of each pixel to a simple exponential decay. (e) Distribution of the fitted k values for reduction in 0.1% $Na_2S_2O_4$. Scale bars: 1 μm.

The flower-like (as opposed to radially symmetric) patterns we observed suggest strong anisotropy: the autocatalytic nature of the reaction amplifies differences in local reaction rate during radial propagation. In our IRM results we occasionally noticed point-like nanoscale defects (white arrows in Figures 1ef and 3a-c) and wrinkles (solid cyan arrows in Figure 1e) that blocked the propagation of reaction and so contributed to the flower-like patterns. Other factors, including graphene crystallographic orientations and atomic structural defects[47] may also lead to anisotropic increases or decreases in local reaction rate.

From a different perspective, our observed wave-like, two-dimensional propagation of reaction in graphene also bears a striking resemblance to chemical waves in reaction–diffusion systems:[48] The autocatalytic oxidation mechanism makes graphene an excitable media, but here propagation of reaction is through the generation of new defects at the wavefront within the two-dimensional material as opposed to the diffusion of chemicals. Consequently, the spatial dimensions of our reaction patterns are orders of magnitude smaller.[48]

We next examined the reduction kinetics of GO. Starting monolayer GO flakes, as produced by the conventional Hummers' method,[49] exhibited typical IRM signal of I/I_0 = 0.96−0.98, in agreement with theory (Figure 1b). A steady decrease in I/I_0 was observed as GO was reduced, whereas no change in I/I_0 was found when the top medium was water (Figure 6a). For quantification, we again converted I/I_0 to reaction progress, here as the local percentage of remaining GO (right-side y-axis of Figure 6a).

A 1% solution of ascorbic acid (vitamin C)[50] exhibited a modest reaction rate that gradually decreased from 1%/min to 0.4%/min to reach ~20% reduction progress (~80% remaining GO) at 40 min. Spatially uniform reduction was observed for the process (Figure 6a inset).

In contrast, a solution of 0.1% sodium dithionite ($Na_2S_2O_4$; also known as sodium hydrosulfite)[51] showed a much higher initial reaction rate of >15%/min, but this rate quickly slowed down as the reduction progressed towards a limit of ~40% remaining GO (Figure 6a). Despite this significant temporal variation in reaction rate, the reduction process is characterized by spatial homogeneity: different locations showed near-identical reaction dynamics (red and blue curves in Figure 6a), and maps of the time-dependent reaction progress (Figure 6b) and rates (Figure 6c) were homogeneous across the sample at all time.

The initially fast, then quickly decelerating reaction dynamics was well fit by a simple exponential decay (Figure 6a), suggesting a pseudo-first-order reaction mechanism in which the reaction rate is directly proportional to the remaining reaction sites in the two-dimensional GO system. By fitting an exponential decay to the reaction time trace of every pixel, we thus mapped out local first-order reaction rate constant k (Figure 6d). Spatial homogeneity was again observed, with the distribution of k between pixels (Figure 4e) within a few percent (0.233±0.005 min^{-1}). Reduction with 1% $Na_2S_2O_4$ showed similar, spatially homogeneous, exponential reaction dynamics with faster rates (Figure 4ad), and the reduction proceeded further to reach ~30% remaining GO (Figure 6a).

We next employed IRM to probe the effects of different reaction parameters, and in this process identified a strong pH-dependence for the reduction of GO. An unadjusted 1% ascorbic acid solution had pH~3. Increasing pH to 7 (neutral) and 14 (basic) led to significantly enhanced reaction rates (Figure 7a). Spatially homogeneous reaction dynamics were observed across all samples under different conditions (Figure 7b).

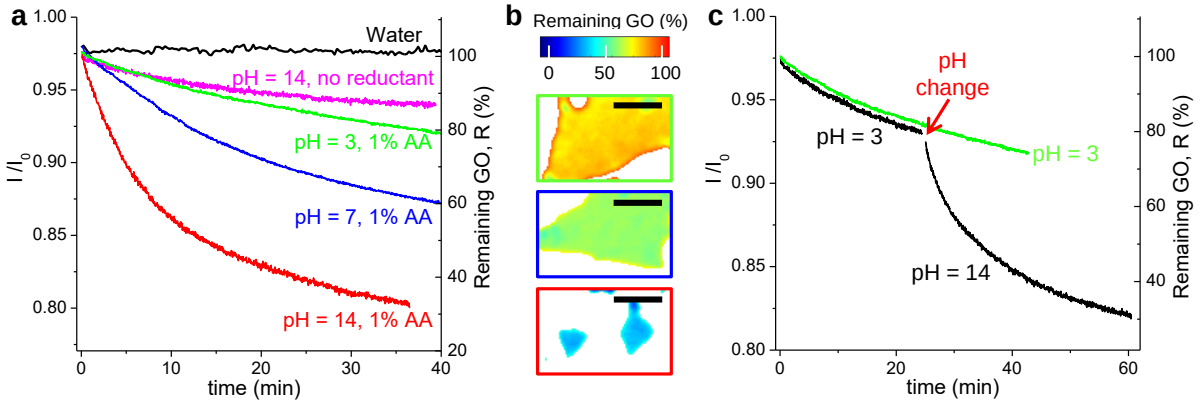

Figure 7. *In situ* recording identifies pH as a key parameter in GO reduction. (a) IRM signal (left axis) and the converted reaction progress (right axis) for the reduction of GO in 1% solutions of ascorbic acid at pH 3, 7, and 14, in comparison to results in water and a pH 14 solution with no reductants added. (b) IRM mapping of the local reaction progress for pH 3, 7, and 14 at ~40 min. Scale bars: 2 μm. (c) IRM monitoring of the reduction progress of GO in 1% ascorbic acid as pH is altered from ~3 (unadjusted) to 14.

We further monitored the reduction of GO by 1% ascorbic acid as pH was altered *in situ* from 3 to 14 (Figure 7c). A sudden jump in reaction rate was noted, thus pinpointing pH as a key parameter of the reaction. In comparison, Raman spectroscopy only showed minor increases in D peak for reduced GO (Figure 8), in agreement with previous results,[28,29] and no noticeable differences were found for reduction at pH=3 vs. pH=14.

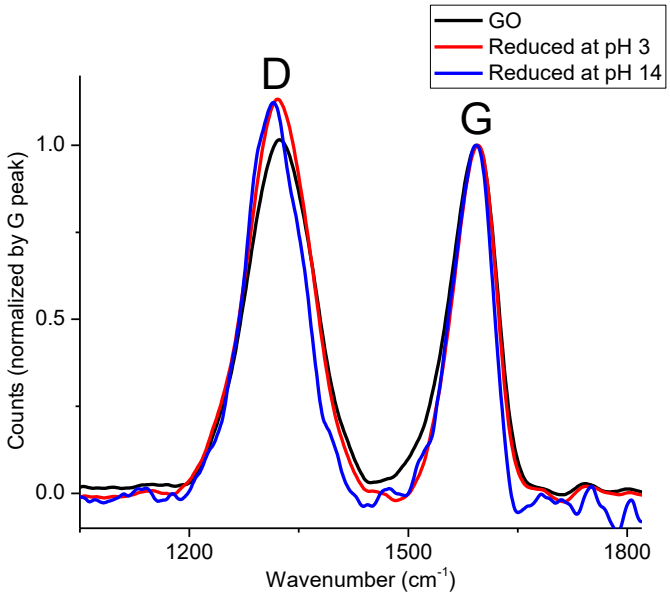

Figure 8. Raman spectroscopy of graphene oxide (GO) before (black) and after 40 min reduction in 1% solutions of ascorbic acid at pH 3 (red) and pH 14 (blue). Results are normalized to the height of the G peak.

Previous work reported the auto-reduction of GO under alkaline conditions.[52] With IRM we found GO to be slowly reduced in a pH 14, NaOH-only solution to reach a reduction progress of ~12% at 40 min (magenta trace in Figure 7a). Our results thus suggest that alkaline conditions activate GO to a more reactive state, which results in both discernable auto-reduction and significantly faster reactions with reductants.

1.3 Conclusion

In summary, through IRM we have attained spatially resolved *in situ* reaction dynamics for the solution-phase oxidation of graphene and reduction of GO. Starting from a two-dimensional crystal with few structural defects, we found the oxidation process of graphene to be spatially and temporally heterogeneous. Reaction initiated at highly localized, nanoscale hotspots associated with structural defects, and then propagated away as new defects are locally created at the wave

front, thus resulting in microscopic, flower-like patterns unique to the two-dimensional system. In contrast, spatially homogeneous, yet pH-dependent pseudo-first-order reaction dynamics was found for the reduction of GO, indicating that active reaction sites exist uniformly across the sample at high densities, conceivably a result of the harsh oxidation reactions during GO preparation. While the ability to reveal these striking, spatially resolved reaction dynamics *in situ* is already fascinating, our work also opens the door to future studies of other chemical reactions of two-dimensional materials.

1.4 Materials and methods

Sample preparation. Graphene samples: graphene CVD-grown on copper foils[42] was spin-coated with a ~200 nm layer of polymethyl methacrylate (PMMA 495 A2, MicroChem, Newton, MA). The copper-graphene-PMMA stack[42,43] was placed in a copper etchant solution (5% HCl + 20% $FeCl_3$) to remove copper, and then transferred to a fresh water bath. Water bath transfer was repeated three times to remove contaminants. A glass coverslip was subsequently used to pick the graphene-PMMA stack off of the surface of the water. The coverslip-graphene-PMMA stack was allowed to dry in air, and then PMMA was removed by immersion in acetone (1 hour) followed by a rinse in isopropanol. The sample was dried with nitrogen gas. GO samples: GO solutions, as prepared by the conventional Hummers' method,[49] were spin-coated onto glass coverslips. A droplet of diluted GO solution was placed on the surface of a coverslip and allowed to rest for 5 minutes. The coverslip was then spun for 60 seconds with an acceleration of 50 RPM/s and a final rotational speed of 3000 RPM.

Interference reflection microscopy (IRM). IRM was performed on an inverted wide-field epifluorescence microscope.[4] The Olympus IX73 microscope was configured with an UplanFl 100x oil-immersion objective (NA ~0.9 with iris diaphragm) and a standard lamp for fluorescence microscopy (U-HGLGPS). The filter cube contained a 50/50 beam splitter (Chroma 21000), a 530/10 nm band-pass filter (Chroma D532/10x) as the excitation filter, and no emission filter. The filtered light passed through the sample and was reflected at the substrate-sample-top medium interfaces (Figure 1a). Interference between these interfaces led to wide-field IRM images, which were recorded using an Andor Zyla 4.2 sCMOS camera at 1024x1024 pixels with 16-bit depth and typical integration time of 20-500 ms. Effective pixel size was 65 nm. The microscope field diaphragm was closed down to slightly smaller than the 1024x1024 frame size to reject stray light. Prepared sample coverslips with either graphene films or GO flakes were placed on the microscope, and first overlaid with a layer of water for IRM identification of suitable imaging areas. Continuous IRM recording was started, and then the water layer was replaced with a reactant solution. The reaction process was thus recorded *in situ*.

Data Analysis. Collected data files contained a series of raw images 1024x1024 in size that were captured every ~100 ms (typical file size: 20-100 gigabytes). Consecutive frames were first averaged to reduce file size and further enhance signal to noise, so that the effective time resolution of the processed data was a few seconds, more than sufficient for the reaction dynamics in this study. The images were background-corrected and drift-corrected. Light intensity (I) of each pixel was normalized to that of the blank areas of the coverslip (I_0) for each frame. Measured I_0/I was converted into reaction progress (local percentage of GO) through a comparison with the I_0/I values of graphene and GO, as discussed in text. Local linear reaction rates (in the unit of %/min) were

obtained through linear fits to the reaction progress of each pixel during different time spans as indicated. Local first-order reaction rate constants k (in the unit of min^{-1}) were obtained by fitting the full time-dependent reaction progress of each pixel with a simple exponential decay.

Chapter 2: Light-assisted diazonium functionalization of graphene and spatial heterogeneities in reactivity

The work in this chapter was conducted in collaboration with Wan Li, Michal Wojcik, Bowen Wang, Liang-Chun Lin, Markus. B. Raschke, and Ke Xu. It is reproduced in part here from ref[53] with permission from all co-authors.

2.1 Introduction

The promise of graphene, a key two-dimensional material with outstanding optical, electrical, and mechanical properties,[16,17] is substantially expanded through chemistry, from the tuning of electronic properties to the addition of different functionalities towards applications.[20,22,24,54] To overcome the low chemical reactivity of the graphene basal plane, reaction with the highly reactive radicals produced from aryl diazonium salts has been one of the most common approaches for the functionalization of graphene under ambient conditions.[5-13,55] However, it has been difficult to monitor the reaction dynamics of this important system, given that graphene is only a single layer of carbon atoms. We recently developed a facile, label-free approach based on interference reflection microscopy (IRM) to record *in situ* the mechanical properties[4] and reaction dynamics[14,15] of graphene with ~300 nm spatial resolution and video-rate temporal resolution. In particular, for the oxidation of graphene, we have visualized rich spatiotemporal heterogeneities and demonstrated how it could be driven reversibly through electrochemistry[14,15].

In this chapter, we apply IRM to study the prototype diazonium reaction of graphene with 4-nitrobenzenediazonium tetrafluoroborate (4-NBD).[5-13] Unexpectedly, we find a light-driven mechanism that is highly effective at low light intensities. The reaction is sensitive to the illumination wavelength, so that at the same intensity level, blue visible light strongly promotes the reaction, whereas red light has no apparent effects when compared to the dark reaction. Moreover, we report rich spatial heterogeneity for the reaction, including substantially faster reactions at graphene edges and an unexpected flake-to-flake variation in reaction rate. Finally, we demonstrate the direct photo-patterning of 4-NBD functionalization, achieving ~400 nm patterning resolution.

2.2 Results and discussion

Copper-grown monolayer graphene[42] was transferred onto a glass coverslip substrate, which was then mounted onto an IRM system based on a wide-field inverted microscope.[4,14] The sample was immersed under an aqueous solution of 4 mg/mL (16.9 mM) 4-NBD. The illumination light entered from the bottom through the glass substrate as a near-parallel beam, and was reflected and interfered with itself at the graphene sample (Figure 9a).

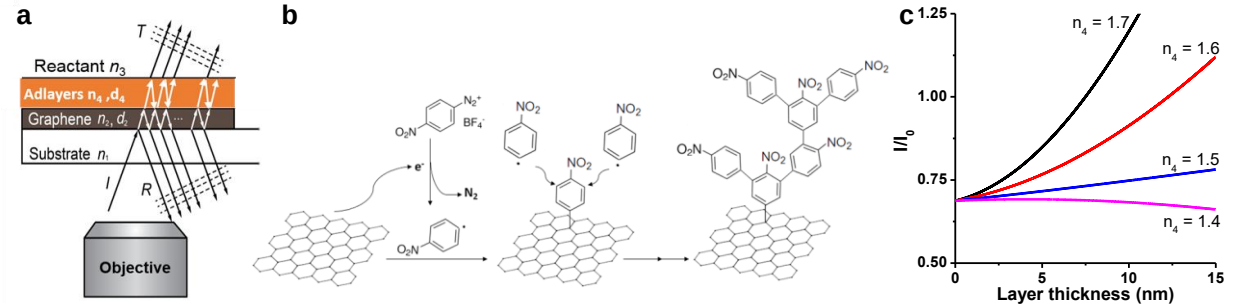

Figure 9. IRM visualization of the diazonium functionalization of graphene. (a) Schematic of the system. n_1, n_2, n_3, and n_4 denote the complex indices of refraction for the substrate, graphene, the reactant solution, and the functionalized layer on top of graphene, respectively. (b) Reaction scheme for the reaction of graphene with 4-NBD. (c) The predicted IRM signal at 450 nm wavelength for monolayer graphene as a function of the thickness of the functionalized layer, for layers of different refractive indices n_4.

According to the general mechanism of the diazonium reaction (Figure 9b),[11,56] a delocalized electron is transferred from graphene to the aryl diazonium cation, thus generating an aryl radical after the release of N_2. The aryl radical covalently reacts with the graphene surface, but also reacts with the already attached aryl molecules to form a nanometer-thick polymer layer.[7,12,56] Through transfer-matrix analysis based on modifications to our previous model,[4] the presence of a thin dielectric layer on top of monolayer graphene would substantially alter the local IRM signal:

$$I = \left| \frac{e^{i(\varphi_2+\varphi_4)} r_{12} + e^{-i(\varphi_2-\varphi_4)} r_{24} + e^{-i(\varphi_2+\varphi_4)} r_{43} + e^{i(\varphi_2-\varphi_4)} r_{12} r_{24} r_{43}}{e^{i(\varphi_2+\varphi_4)} + e^{-i(\varphi_2-\varphi_4)} r_{12} r_{24} + e^{-i(\varphi_2+\varphi_4)} r_{12} r_{43} + e^{i(\varphi_2-\varphi_4)} r_{24} r_{43}} \right|^2 I_I \qquad (1)$$

Here I_I is the intensity of the incident light, $r_{12}=(n_1-n_2)/(n_1+n_2)$, $r_{24}=(n_2-n_4)/(n_2+n_4)$, and $r_{43}=(n_4-n_3)/(n_4+n_3)$, with n_1, n_2, n_3, and n_4 being the complex refractive indices of the substrate, graphene, reaction solution, and the functionalized layer, respectively. $\varphi_2=2\pi n_2 d_2/\lambda$ and $\varphi_4=2\pi n_4 d_4/\lambda$ correspond to phase changes, with d_2 = 0.335 nm and d_4 being the thickness of graphene and the functionalized layer, respectively, and λ being the wavelength of the incident light. Meanwhile, the IRM signal measured at a bare glass substrate (an n_1-n_3 interface) is:[4]

$$I_0 = \left| \frac{n_1 - n_3}{n_1 + n_3} \right|^2 I_I \qquad (2)$$

Plotting the normalized IRM signal (I/I_0) as predicted by Eqns. 1 and 2 as a function of d_4 (Figure 9c) suggests monotonic changes in the IRM signal for increased thickness of the functionalized layer, with particularly high sensitivities for n_4 > ~1.6.

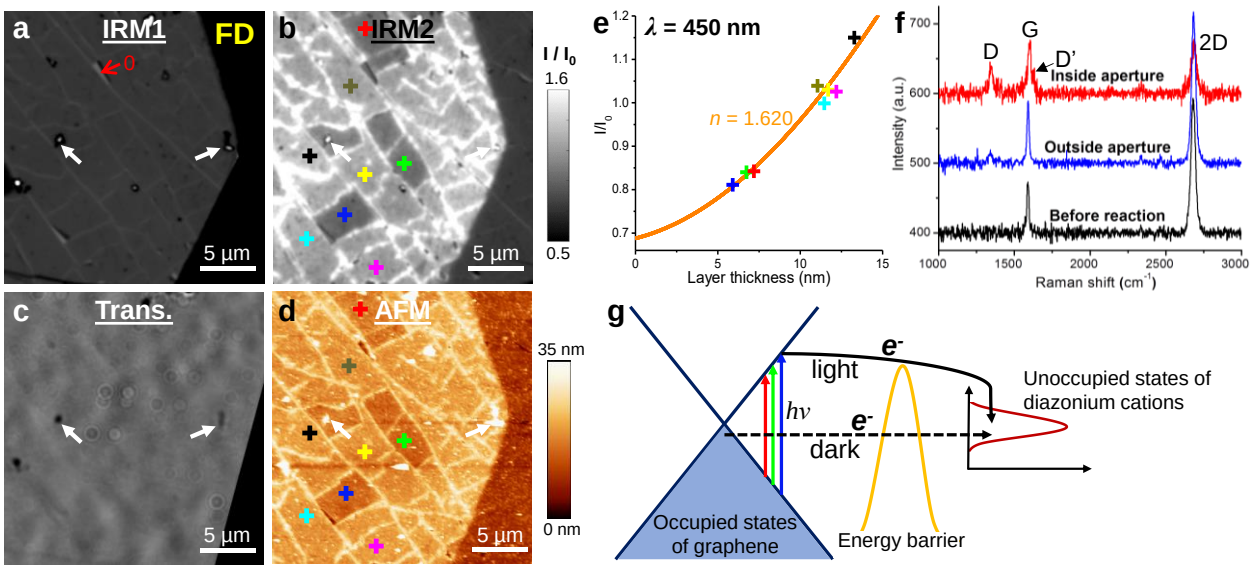

Figure 10. IRM unveils a strong light dependence of the diazonium reaction. (a-b) IRM images of monolayer graphene, before (a) and after (b) 220 s of reaction in the 4-NBD solution under continuous illumination of 0.5 W/cm^2 at 450 nm. Note that in (a), a field diaphragm aperture (marked as "FD" in the image) confined the illumination area, whereas in (b), this confinement was removed to image the full view. "0" points to exposed glass surface due to a local tear in graphene. (c-d) Transmission light microscopy (c) and AFM (d) images of the same region as (b) after the reaction. White arrows in (a-d) point to debris that were observed across different microscopy modes, which aided alignment. (e) Local IRM contrast vs. the AFM-determined height of the functionalized layer, for different parts of the sample marked by the colored crosses in (b,d). Orange curve: fit to Eqn. 1, yielding n_4 = 1.620. (f) Raman spectra after the reaction, for regions inside (red line) and outside (blue line) the optical aperture, compared to pristine graphene (black line). (g) A possible hot electron transfer mechanism for the reaction.

We started by monitoring the reaction using 450 nm illumination obtained by applying a 10 nm-bandwidth bandpass filter on a lamp, thus achieving a relatively low illumination intensity of ~0.5 W/cm^2 in the wide field. A rapid increase in the IRM signal (I/I_0) was observed (Figure 10ab and Figure 11), suggesting reaction at the graphene surface. Unexpected, after 220 s of reaction, we observed a sharp contrast in IRM signal between regions inside and outside the 450 nm-illuminated area, hence a clear boundary defined by the illumination aperture (field diaphragm) (Figure 10b). Meanwhile, conventional transmission microscopy showed limited contrast (Figure 10c); detailed analysis indicated that graphene absorbed ~2% of the transmitted light,[44] which did not change significantly before and after the reaction.

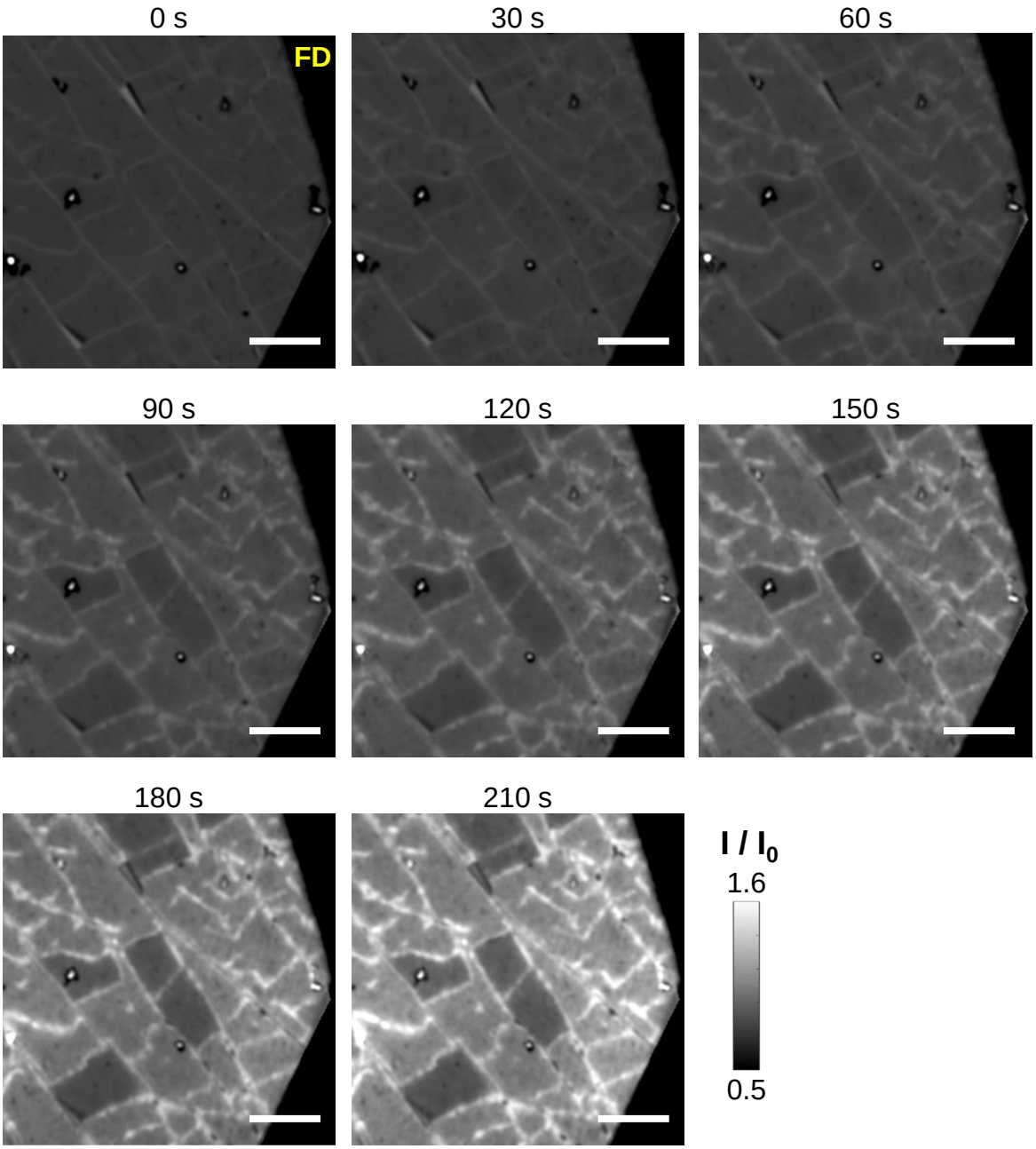

Figure 11. A sequence of IRM images from the *in situ* data, for the diazonium functionalization of graphene under 0.5 W/cm^2 of 450 nm illumination, shown in 30 s increments. "FD": field diaphragm aperture. Scale bars: 5 μm.

Raman spectroscopy, carried out after rinsing and air-drying the sample, showed a strong D peak, the appearance of a D′ peak, and a significantly reduced 2D peak for a region inside the illumination aperture (Figure 10f), indicating substantial reaction. In contrast, only a small D peak showed up for regions outside the optical aperture (Figure 10f), consistent with the known low reaction rate of this system at room temperature.[5,9,10] Meanwhile, atomic force microscopy (AFM) showed a ~10 nm height increase for the 450 nm-exposed region (Figure 10d); local variations in height were noted, which correlated well with the local IRM signal (Figure 10e). Infrared

scattering scanning near-field optical microscopy (s-SNOM)[57] further showed that such local variations in layer height correlated well with the strength of the local nitro (–NO_2) infrared signal arising from the NO symmetric stretch vibrational mode (Figure 12), consistent with the expected surface polymerization process of 4-NBD (Figure 9b). Whereas we will discuss the local height variations in further detail below, here fitting the IRM signal-AFM height relationship for different parts of the sample to Eqn. 1 (Figure 10e) gave n_4 = 1.620, a value comparable to polymers of related structures (e.g., 1.614 at 450 nm for polystyrene).

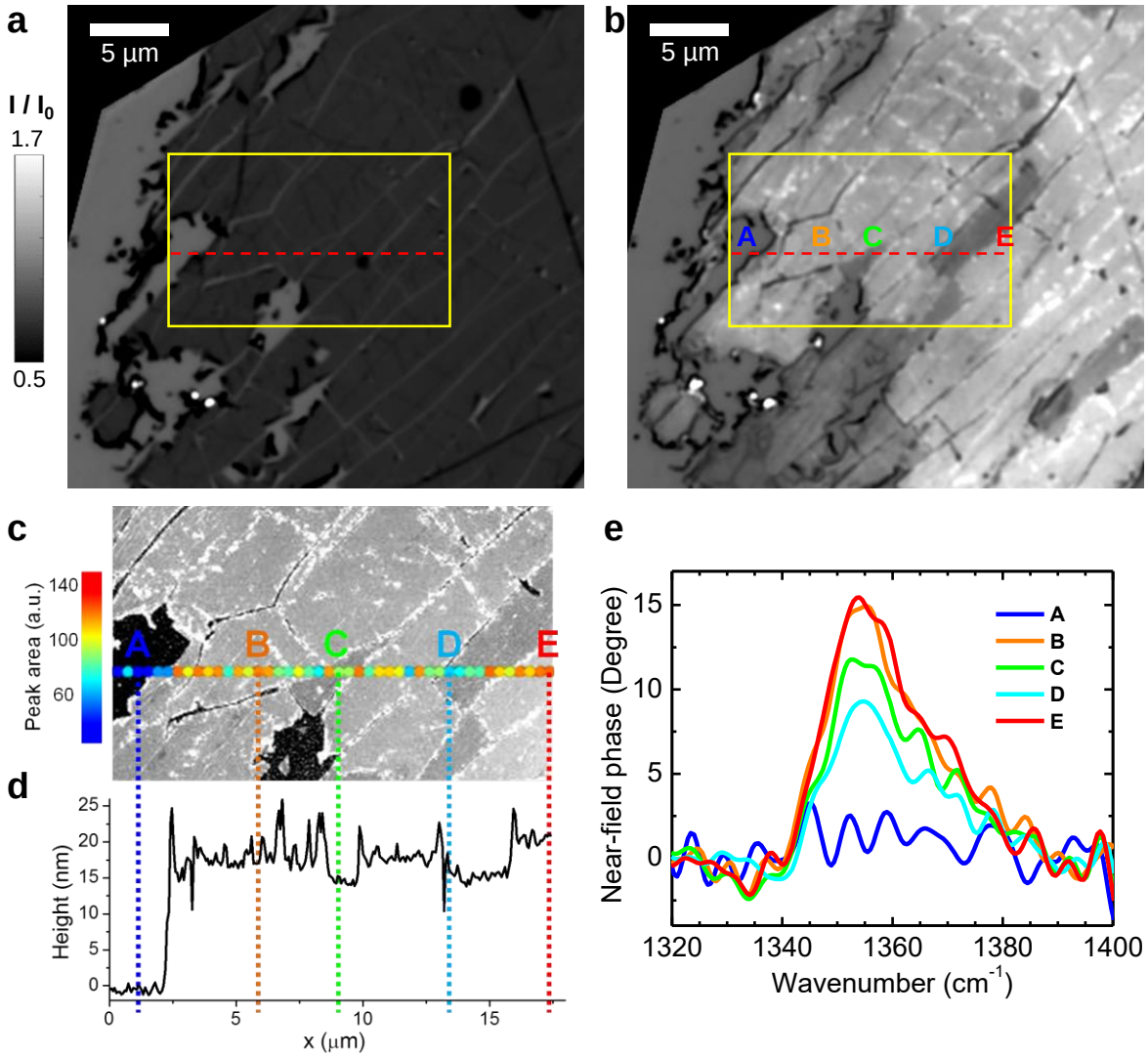

Figure 12. Infrared *s*-SNOM results. (a,b) IRM images for a monolayer graphene sample before and after diazonium functionalization under 450 nm illumination. (c) AFM image after the reaction, corresponding to the yellow boxes in (a,b). Color dots mark points along a line [red dashed lines in (a,b)] where local infrared *s*-SNOM spectra were measured, with the color presenting the locally measured peak area for the nitro (–NO_2) peak at ~1350 cm^{-1}. (d) Height profile along the line. (e) Local infrared *s*-SNOM spectra for the representative spots A-E marked in (b) and (c), showing reduced local nitro (–NO_2) signal for graphene flakes with thinner reacted layers (C,D).

Together, our results indicate that the diazonium functionalization of graphene is strongly promoted by 450 nm illumination. The photochemical addition reaction of graphene has been previously examined for peroxides and halogens for its potential controllability and patterning capability.[58-62] In our case, since 4-NBD is transparent over the visible range, similar to the case of benzoyl peroxide (BPO), a similar hot electron transfer mechanism[58,62] may be invoked, in which the photoexcited graphene transfers a hot electron to the unoccupied states in aryl diazonium cations (Figure 10g) to facilitate the radical generation and subsequent reaction with graphene (Figure 9b). Although the Fermi energy of undoped graphene is comparable to that of the unoccupied states in 4-NBD,[11] the dark reaction is slow at room temperature,[5,9,10] possibly due to an energy barrier that needs to be overcome for the electron transfer process (Figure 10g), as discussed previously for the BPO system.[62] However, we note that the light intensity in our work (~0.5 W/cm^2) is five orders of magnitude lower than previously used for BPO (~10^5 W/cm^2 by focusing a ~1 mW laser into a ~1 μm spot).[58,62] This substantial difference may be related to a higher reactivity of 4-NBD, and/or the ease of transferring electrons to diazonium cations in the aqueous solution when compared to BPO in organic solutions. A comparison of the reaction rate and the amount of light absorbed by graphene (~2.3%[44]) gave an apparent quantum yield of ~1×10^{-3}, reasonably high for the electron transfer mechanism.

We next found the reaction kinetics to be highly dependent on the illumination light wavelength. At a comparable intensity level, illumination with a 532 nm green light for 1 h (Figure 13a) led to substantially less reaction when compared to that achieved within 220 s under the 450 nm blue illumination (Figure 10b). Plotting the layer thickness, as converted from the *in situ* IRM data (Figure 11 and Figure 14), against the reaction time (Figure 13d) showed a ~7-fold difference in reaction rate for the initial reaction, with the reaction rate under the 532 nm illumination further dropping by more than one-half after the first ~0.6 nm. Even lower reactivity was observed for the 610 nm red light (Figure 13b and Figure 15), under which condition the reaction kinetics was similar to that in the dark (Figure 13cd).

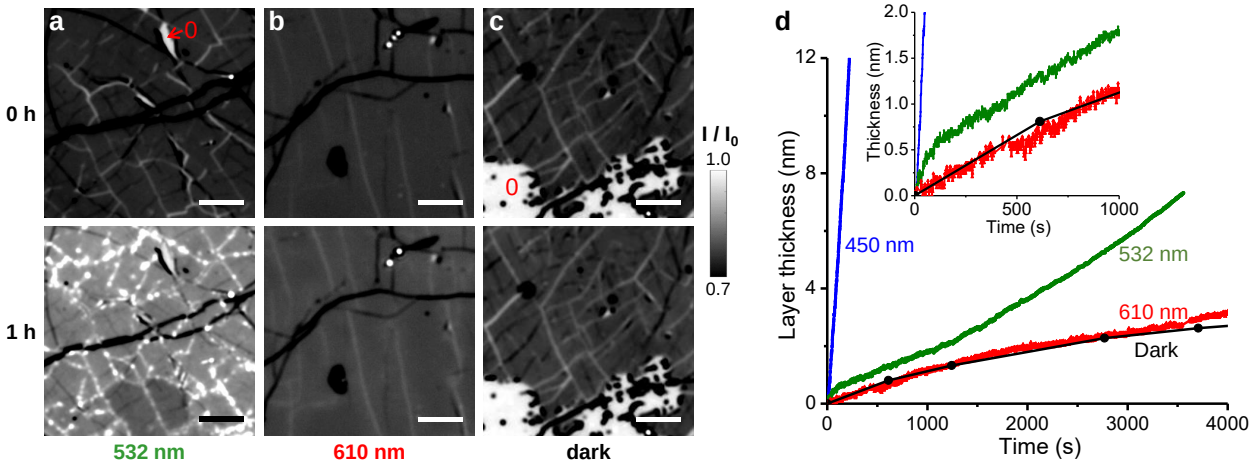

Figure 13. IRM unveils a marked dependence of reaction rate on illumination wavelength. (a-c) IRM images of monolayer graphene before (top panels) and after (bottom panels) 1 h reaction with 4-NBD under 532 nm (a) and 610 nm (b) illuminations at 0.6 W/cm^2, and under dark (c). Scale bars: 5 μm. Note that when compared to Figure 2ab, here a narrower range of I/I_0 is chosen to better present the lower levels of reaction. "0"s in (a,c) mark areas with no graphene coverage. (d) *In situ* IRM results of layer thickness for typical basal-plane regions for the reaction under 450 nm

(blue), 532 nm (green), and 610 nm (red) and in the dark (black). For the "dark" sample, short (~10 s) exposures at 610 nm were intermittently applied to inspect the reaction for just a few time points, whereas continuous illumination was used for the other conditions. Inset: zoom-in for the first 1000 s.

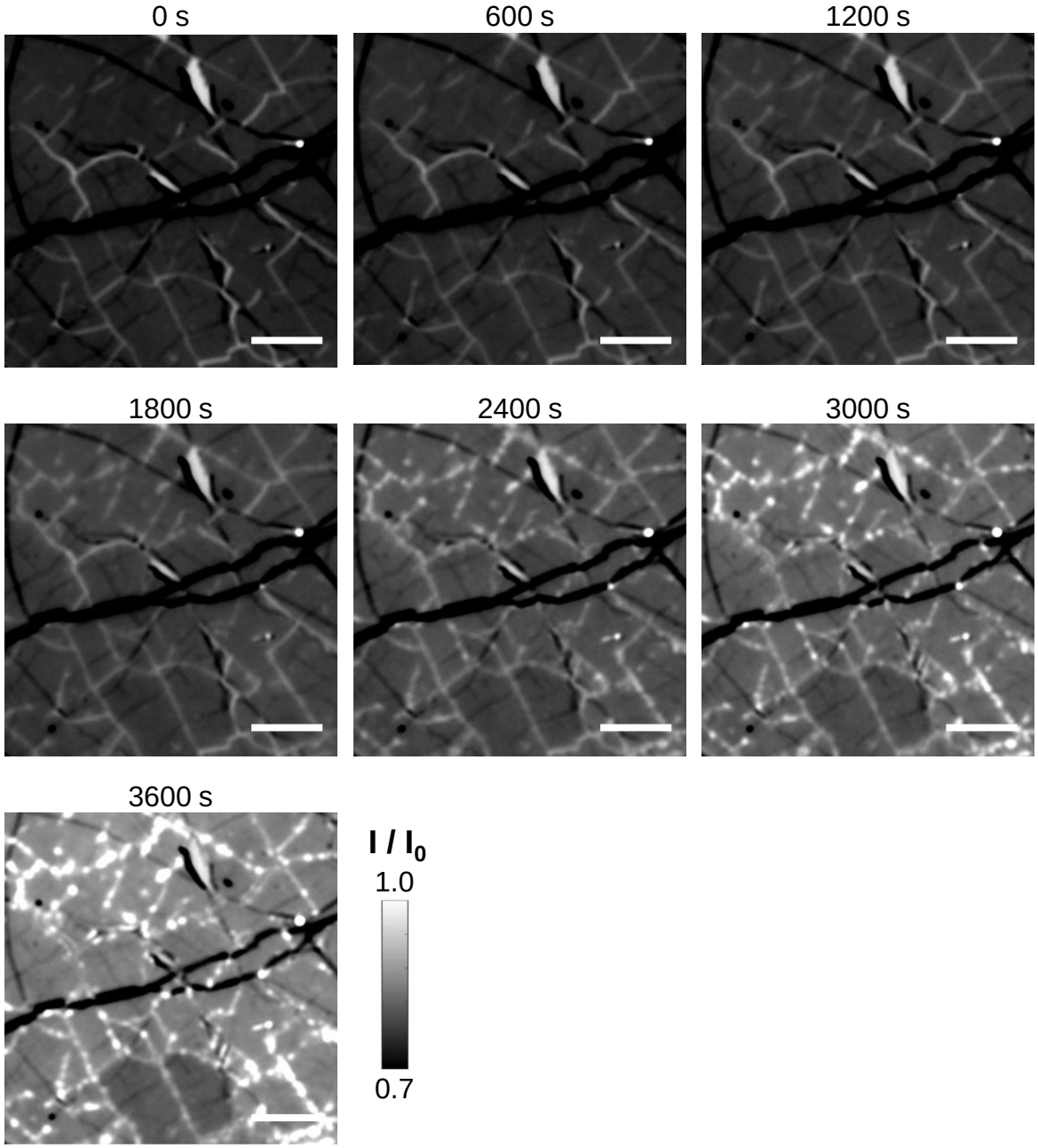

Figure 14. A sequence of IRM images from the *in situ* data, for the diazonium functionalization of graphene under 0.6 W/cm^2 of 532 nm illumination, shown in 600 s increments. Scale bars: 5 μm.

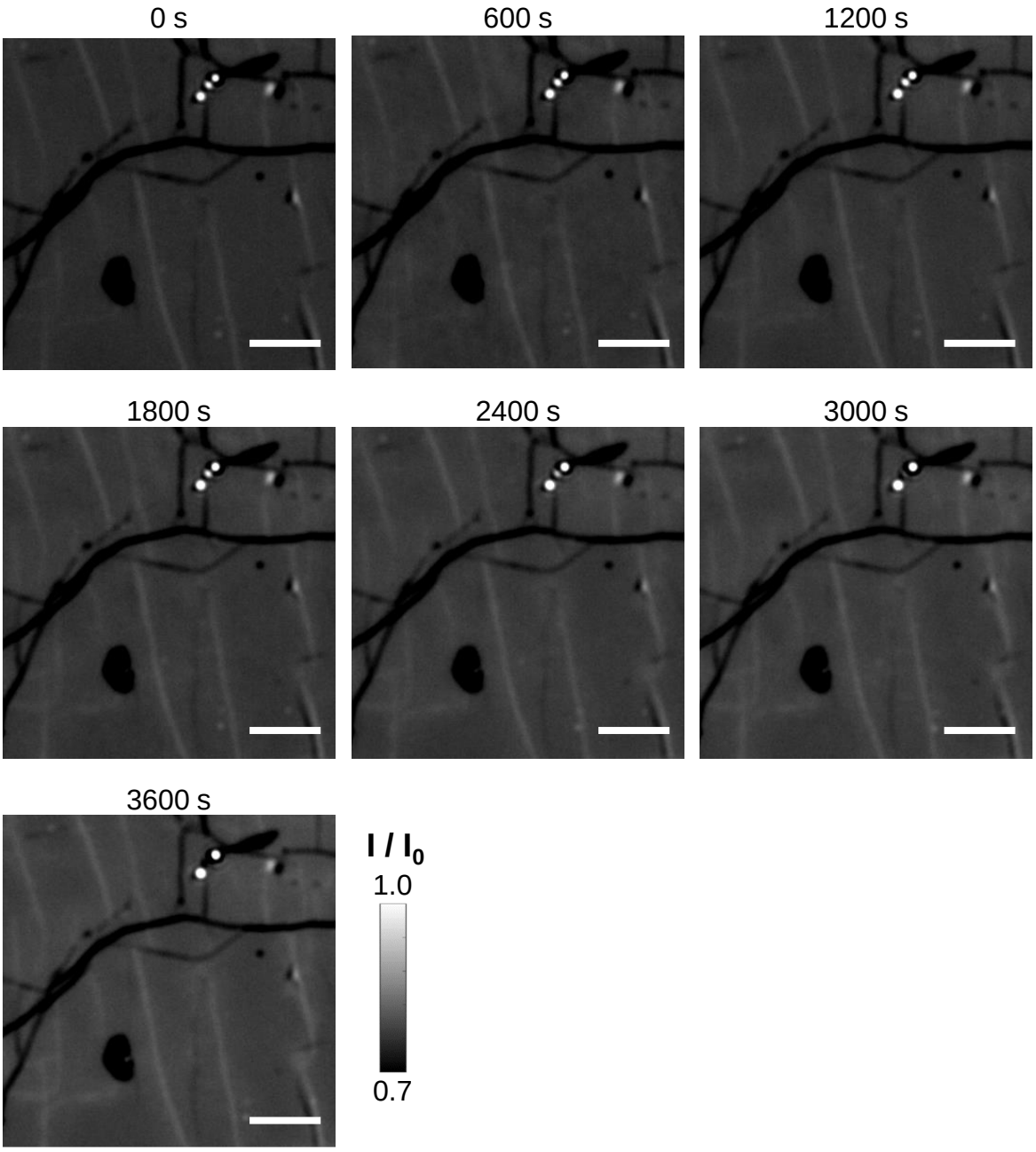

Figure 15. A sequence of IRM images from the *in situ* data, for the diazonium functionalization of graphene under 0.6 W/cm^2 of 610 nm illumination, shown in 600 s increments. Scale bars: 5 μm.

The observed strong dependence on illumination wavelength is consistent with the above hot electron transfer mechanism (Figure 10g): whereas graphene uniformly absorb ~2.3% of incident light over the visible spectrum,[44] shorter wavelengths generate photoexcited electrons of higher energy, which better overcome the reaction barrier. Indeed, previous work on the photochemical reaction of graphene with BPO has found that when compared to the 514 nm illumination, reactions under 458 nm and 633 nm illuminations are ~5 times faster and ~10 times slower, respectively.[58] Our results followed a similar trend, albeit that the light intensity involved was ~10^5

lower, and that the long-wavelength reaction was competed by dark reactions, both effects possibly related to the higher reactivity of 4-NBD.

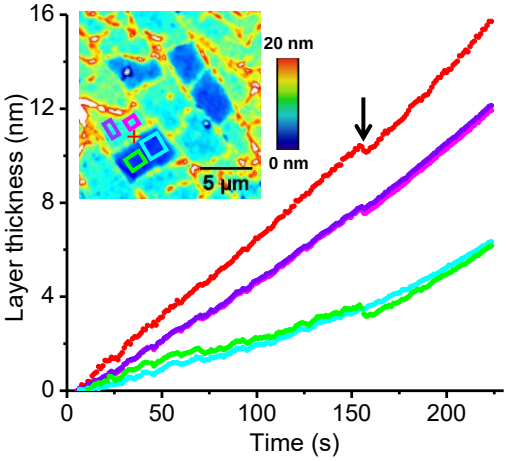

Figure 16. *In situ* IRM results of the layer thickness as a function of reaction time under 450 nm illumination, for different locations of the same sample. Inset: a color map of layer thickness, for a region shown in Figure 10b. The red curve in the main figure corresponds to a spot at the graphene edge marked by the red cross in the inset, whereas the violet, magenta, green, and cyan curves correspond to four different areas marked by the boxes of corresponding colors in the color map inset. Arrow: artifact due to the adjustment of microscope focus.

We next turn to the rich spatial heterogeneity visualized by IRM. One marked feature we found was the bright-up of IRM signals at graphene edges during the reactions (Figure 10b and Figure 13), indicating a higher local reactivity. Correlated AFM images verified that these higher local IRM signals indeed corresponded to taller local layers (Figure 10d). Examining the *in situ* IRM data over time (Figure 16 and Figure 11) showed that the reaction rate at the graphene edges to be consistently faster than the basal plane throughout the reaction. This result may be interpreted as that the graphene edges contained a higher level of structural defects, and so are chemically more reactive.[9,55] Interestingly, our previous IRM work found no reaction enhancement for graphene edges during chemical and electrochemical oxidation processes,[14,15] thus indicating that this difference in edge reactivity is reaction-type dependent.

Another remarkable IRM observation, corroborated by both AFM and infrared *s*-SNOM results, is an unexpected variation of reactivity between different graphene flakes, even though the reactivity within each continuous flake appeared relatively uniform (Figure 16 and inset). Close examination of the IRM images before reaction (Figure 10a) indicated that these flakes were electrically isolated by nanoscale cracks. Thus, even though they were fragmented from the same initial graphene sheet, they were possibly inadvertently doped to different levels on the glass surface,[10] and so shifted to different electrochemical potentials that affected reactivity. For comparison, graphene that contained cracks yet still stayed electrically connected did not exhibit such local variations in reactivity (Figure 17).

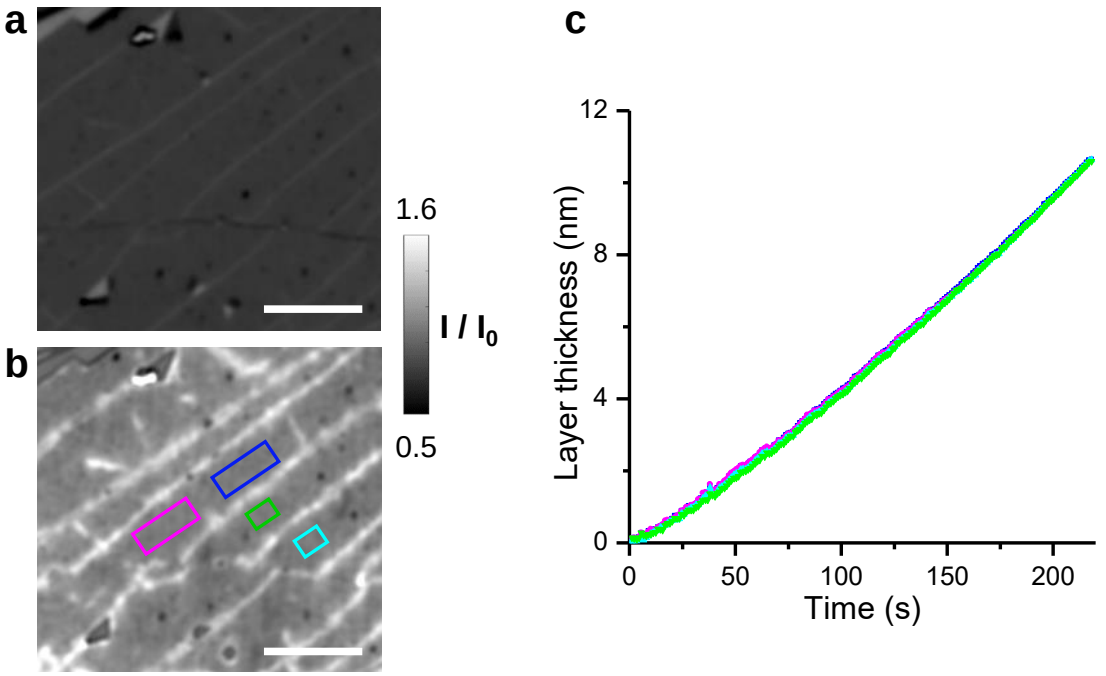

Figure 17. Graphene that contained cracks yet still stayed electrically connected did not exhibit strong local variations in reactivity. (a-b) IRM images of monolayer graphene with cracks that did not separate the graphene sheet into electrically isolated flakes, before (a) and after (b) 220 s of reaction in the 4-NBD solution under continuous illumination of 0.5 W/cm^2 at 450 nm. Scale bars: 5 µm. (c) *In situ* IRM results of the layer thickness as a function of reaction time for the different regions marked in (b), showing near-identical results.

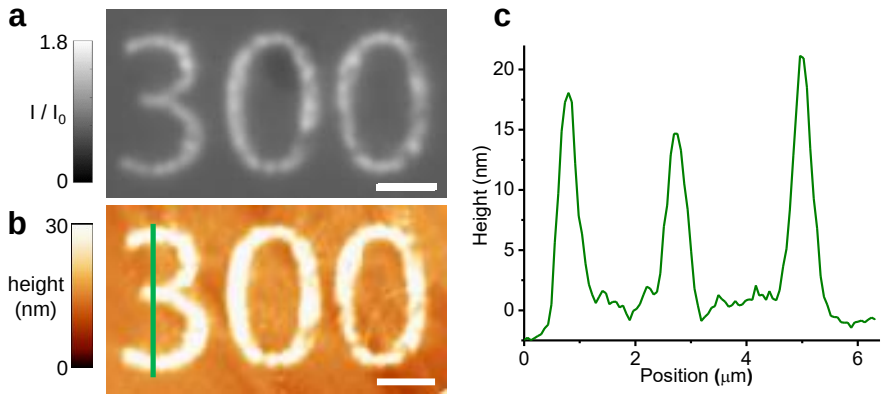

Figure 18. Photo-patterning of the graphene surface through light-assisted diazonium reaction. (a) IRM image of a monolayer graphene sample that was exposed with a photomask under 488 nm illumination in a 4-NBD solution, yielding the pattern "300". (b) AFM image of the same region. Scale bars: 2 µm. (c) Height profile along the green line in (b). Full width at half maximum (FWHM) of the three peaks were 371, 419, and 408 nm, respectively.

Finally, as a possible application for the light-assisted diazonium functionalization discussed above, we examined whether it would be possible to achieve direct photo-patterning using this process. To this end, we inserted a photomask into the collimated 488 nm beam path in a home-built wide-field laser microscope,[63] which effectively functioned as a 200x photolithography

stepper for samples at the microscope image plane. Thus exposing a monolayer graphene sample for 120 s under the immersion of a 4-NBD solution led to good photo-patterning results, with well-defined fine features down to ~400 nm in size readily obtained (Figure 18 and Figure 19).

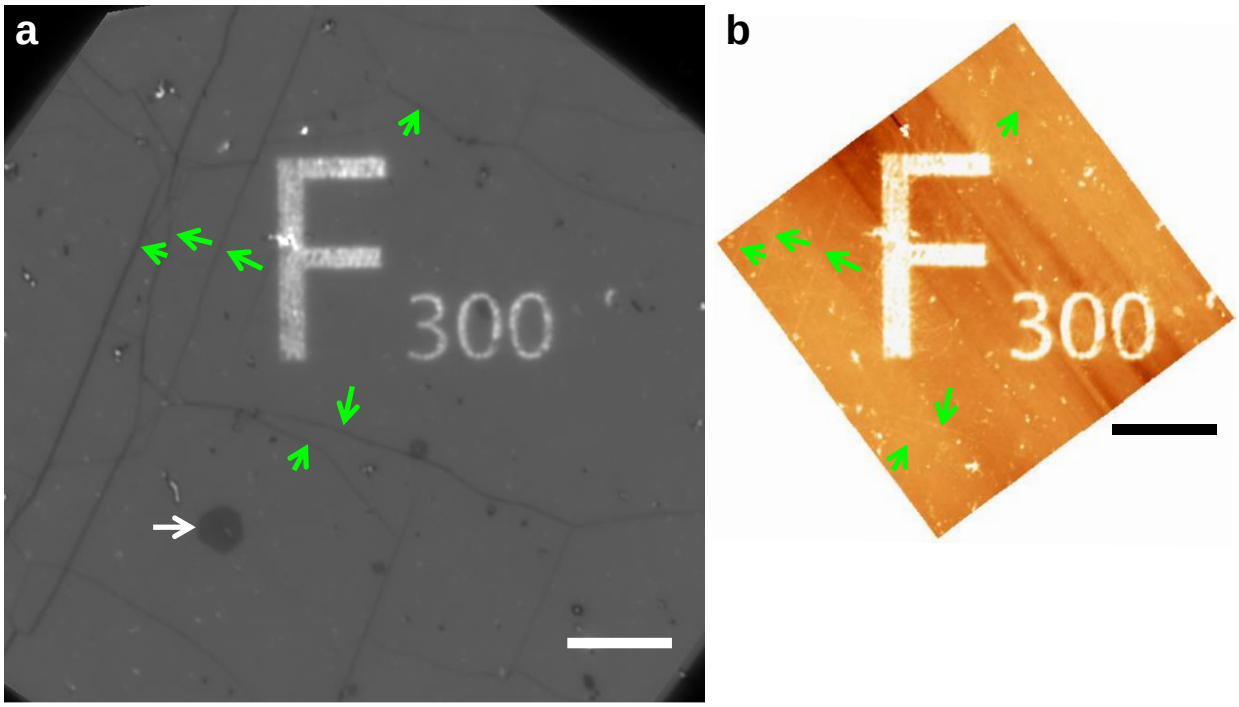

Figure 19. Zoom-out views for the photo-patterning of the graphene surface through light-assisted diazonium reaction. (a) Zoom-out view of the IRM image shown in Figure 5a. (b) Zoom-out view of the AFM image shown in Figure 5b. The "300" patterns correspond to those shown in Figure 5ab. Scale bars: 5 μm. Green arrows point to wrinkles in the monolayer graphene, which are visualized in both IRM and AFM images. The white arrow points to a bilayer island in the otherwise dominantly monolayer graphene.

2.3 Conclusion

In conclusion, through IRM and correlated AFM, Raman, and infrared *s*-SNOM experiments, we have shown that the diazonium functionalization of graphene to be significantly promoted by blue light at low levels. Green light was much less effective in promoting the reaction, whereas red light exhibited negligible effects when compared to the dark reaction. While these results are consistent with the hot electron transfer mechanism previously proposed for the reaction of BPO, the light intensity here for 4-NBD was orders of magnitude lower. We thus demonstrated facile photo-patterning in the wide-field at similarly low light intensities, achieving ~400 nm patterning resolution. Together with the rich spatial heterogeneities we further visualized for the reaction, including enhanced reaction at edges and the unique flake-to-flake variations in reaction rate, we thus shed new light on one of the most popular approaches for the functionalization of graphene under ambient conditions.

2.4 Materials and methods

Graphene sample preparation. CVD graphene on copper foils (ACS Material) was spin-coated with poly (methyl methacrylate) (PMMA) and wet-transferred[42] onto #1.5 glass coverslips (VWR, 16004-322). The coverslip-graphene-PMMA stack was dried in air overnight, and PMMA was removed by immersion in acetone and isopropanol. The sample was then dried in air.

IRM monitoring of diazonium functionalization. 4 mg of 4-nitrobenzenediazonium tetrafluoroborate (Sigma-Aldrich, 294438) was dissolved in 1 mL Milli-Q water to form a 4 mg/mL (16.9 mM) solution. ~300 µL of the solution was dropped on top of the above graphene sample. IRM was performed on an Olympus IX73 inverted epifluorescence microscope with an Olympus UplanFl 100× oil-immersion objective with an adjustable iris (numerical aperture adjusted to ~0.9) and a standard lamp for fluorescence microscopy (U-HGLGPS). The filter cube contained a 50/50 beam splitter (Chroma 21000), no emission filter, and a narrow bandwidth (~10 nm) band-pass filter at 450 nm (Thorlabs FB450-10), 532 nm (Chroma D532/10x), or 610 nm (Semrock FF01-610/5) at the position of excitation filter. By adjusting the lamp intensity level and the numerical aperture of the objective lens, the light intensity at the sample was 0.5, 0.6, and 0.6 W/cm^2 for the 450, 532, and 610 nm illuminations, respectively. Wide-field IRM images were recorded using an Andor Zyla 4.2 sCMOS camera at ~50 ms frame time. Consecutive frames were averaged to reduce the file size and further enhance signal-to-noise, so that the effective time resolution of the processed data was ~1 s, sufficient for the reaction time scales in this work. Light intensity (I) of each pixel was normalized to that of the blank areas of the coverslip (I_0) for each frame.

Photopatterning through the light-assisted diazonium reaction. The graphene sample on the glass coverslip was mounted onto a homebuilt microscope previously constructed for the purpose of super-resolution microscopy in the wide field.[63] A photomask was placed at the expanded, collimated light beam path before the microscope. As the light beam was focused to the back focal plane of the objective lens (Nikon CFI Plan Apochromat λ 100×), the emitted light was parallel at the image plane, and carried the patterns defined by the photomask. The system thus effectively functioned as a 200x stepper for photolithography. 500 µL of 4 mg/mL aqueous 4-NBD solution was dropped on top of the sample, and illumination at 488 nm was immediately applied at ~6 W/cm^2 for 120 s. The sample was then rinsed with water and analyzed by IRM and AFM.

Raman spectroscopy, AFM, and infrared *s*-SNOM characterizations. Raman spectroscopy, AFM, and infrared *s*-SNOM characterizations were carried out after rinsing the sample with water and air-drying. Raman spectra were taken using a Witec Alpha300 (RAS model) Raman spectrometer. Measurements were taken with 532 nm laser excitation with P = 10 mW and acquisition time = 10 s. AFM images were taken on an Asylum MFP-3D system in tapping mode using aluminum-coated probes (Tap300Al-G; BudgetSensors). Nominal values of the force constant, resonance frequency, and tip radius were 40 N/m, 300 kHz, and <10 nm, respectively. AFM data were processed using WsXM.[64] For infrared *s*-SNOM, tunable mid-infrared light was generated by difference frequency generation of signal and idler beams (Harmonixx DFG, APE) from a femtosecond optical parametric oscillator (Levante OPO, APE) with a bandwidth of 150 cm^{-1} centered at 1350 cm^{-1} and with ≤4 mW focused via a parabolic mirror (NA = 0.45, f = 25.4 mm) onto the metallized tip (160AC-GG OPUS, MikroMasch) of an AFM (modified Anasys Nano-IR2S prototype) operating in tapping mode. The near-field tip-scattered signal was detected interferometrically in backscattering by an HgCdTe detector (MCT KLD-0.5-J1/DC/11,

Kolmar Technologies) using lock-in demodulation at the second harmonic of the cantilever motion. Near-field phase response was extracted through complex-valued Fourier transform, which contained absorptive information of the IR response. IR *s*-SNOM spectra were collected with 2–4 cm^{-1} spectral resolution using rapid-scan detection and averaging times of 1–4 min.

Chapter 3: Dynamic, spontaneous blistering of substrate-supported graphene in acidic solutions

The work in this chapter was conducted in collaboration with Bowen Wang, Wan Li, and Ke Xu. It is reproduced in part here from ref[65] with permission from all co-authors.

3.1 Introduction

The outstanding electrical and optical properties of graphene are intricately linked to its extraordinary mechanical behaviors.[66-68] In particular, for substrate-supported graphene, a common device geometry, the formation of gas- or liquid-enclosing bubbles/blisters[69] have in recent years attracted substantial research interest[70-78] for understanding the properties of graphene itself and graphene-substrate interactions, the confinement of molecules,[79-83] as well as for potential applications. Whereas the controlled formation and modulation of bubbles are attainable with carefully engineered substrate geometries,[70,72-74] less control has been achieved for the generation of bubbles/blisters for graphene deposited on common, unpatterned substrates,[69,71,75-78] and when formed, the structures are often static at the hour timescales. Separately, the notion that graphene, after proper processing, may behave as a semipermeable membrane for the selective passing of molecules has garnered focused attention over the past decade.[73,84-90]

In this chapter, we report the unexpected discovery that for graphene deposited on common silicon and glass substrates, the application of acidic solutions of pH<~2 leads to the fast, spontaneous generation of solution-enclosing blisters with high surface coverages. Initially appearing as nanoscale bubbles across the substrate at high densities, within minutes the blisters dynamically coalesce to several micrometers in size and ~100 nm in height. Intriguingly, we further show that in this dynamic system, graphene behaves as a semipermeable membrane, so that the blister volumes can be fast modulated by the solution osmotic pressure in a reversible fashion.

3.2 Results and discussion

3.2.1 IRM unveils dynamic, spontaneous blistering of graphene on the glass surface

Figure 20a presents the typical sample geometry for our *in situ* monitoring of graphene morphology. Monolayer graphene was deposited on a transparent substrate, and then submerged in an aqueous top medium that was readily exchanged during the experiment. An index-matched oil-immersion objective lens imaged through the substrate in the mode of interference reflection microscopy (IRM). While originally developed for cell imaging,[1,2] we recently established IRM as a powerful tool for the quantitative, *in situ* imaging of graphene structures, defects, and reactions.[4,14,15,53,91]

Unexpectedly, for graphene deposited on common glass coverslips, as we replaced the top medium from water to 0.1 M HCl, within minutes, we observed the generation of numerous nanoscale features of varying IRM contrasts that distributed across the sample at high densities (Figure 20d). While generally growing bigger with increased IRM contrasts at the ~10 min time scale, these nanoscale structures also showed dynamic merging and reconfigurations, so that they gradually coalesced into micrometer-sized islands (Figure 20d, and Figure 21). As we examined similarly treated samples on different days, we consistently observed the high coverage of comparable islands (Figure 21).

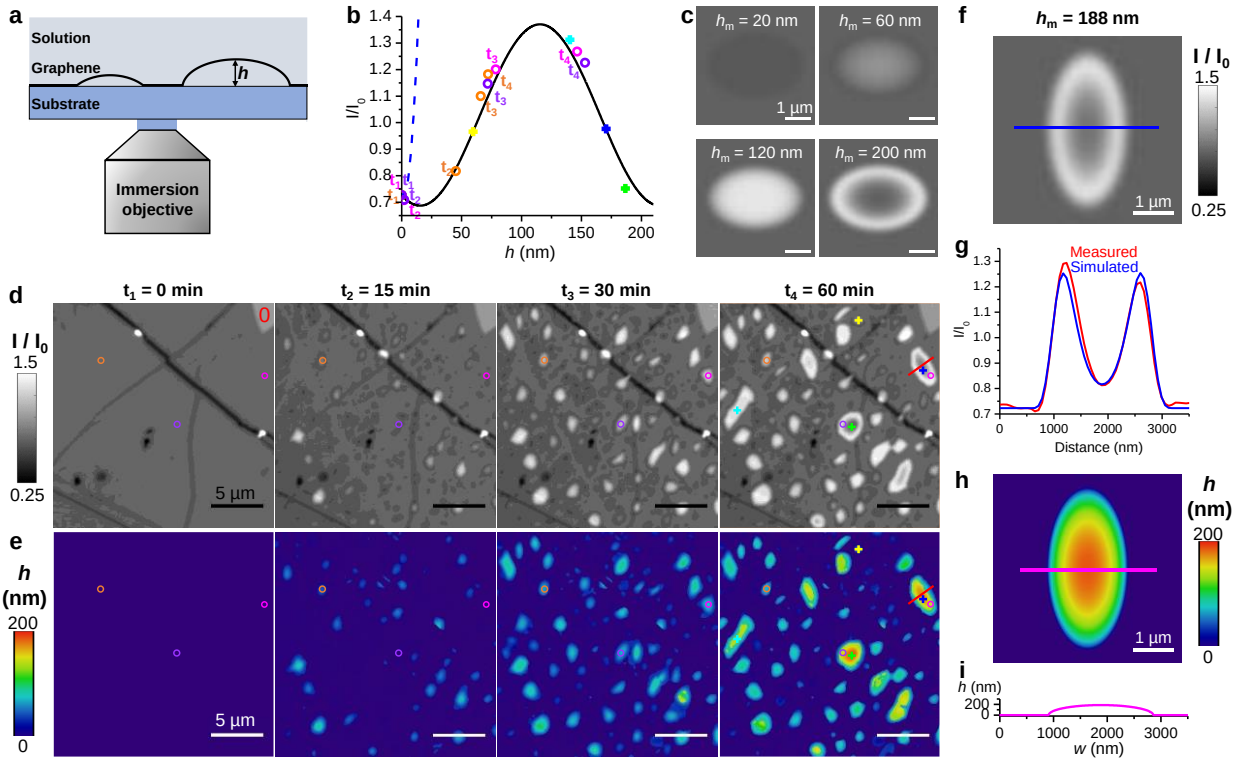

Figure 20. IRM unveils dynamic, spontaneous blistering of graphene on the glass surface. (a) Schematic of the system. (b) Predicted IRM signal (light intensity I normalized by the intensity at the bare substrate I_0) for monolayer graphene on glass, as a function of the local blister height h, for blisters enclosing an aqueous solution (back line) vs. gas (blue dashed line). (c) Simulated IRM images of solution-enclosed graphene blisters of varying maximal heights h_m. (d) Experimental *in situ* IRM images for monolayer graphene on a glass surface, in 0.1 M HCl for different amounts of time. "0" marks locally exposed glass surface. (e) Converted blister height maps. Colored crosses (for final time point) and circles (for different time points): locations for which the IRM signal in (d) is plotted in (b) against the inferred height in (e). Slight value shifts are due to smoothing of the spatiotemporal signals in data processing. (f) Simulated IRM image for a blister of h_m = 188 nm, which matched well to the experimental data for the blister crossed by the red line in the last time point in (d). (g) Overlay of the simulated and measured IRM signals along the blue and red lines in (f) and (d), respectively. (h) Heightmap of the simulated data in (f). (i) Height profile along the magenta line in (h), shown at a 1:1 scale for width w and height h.

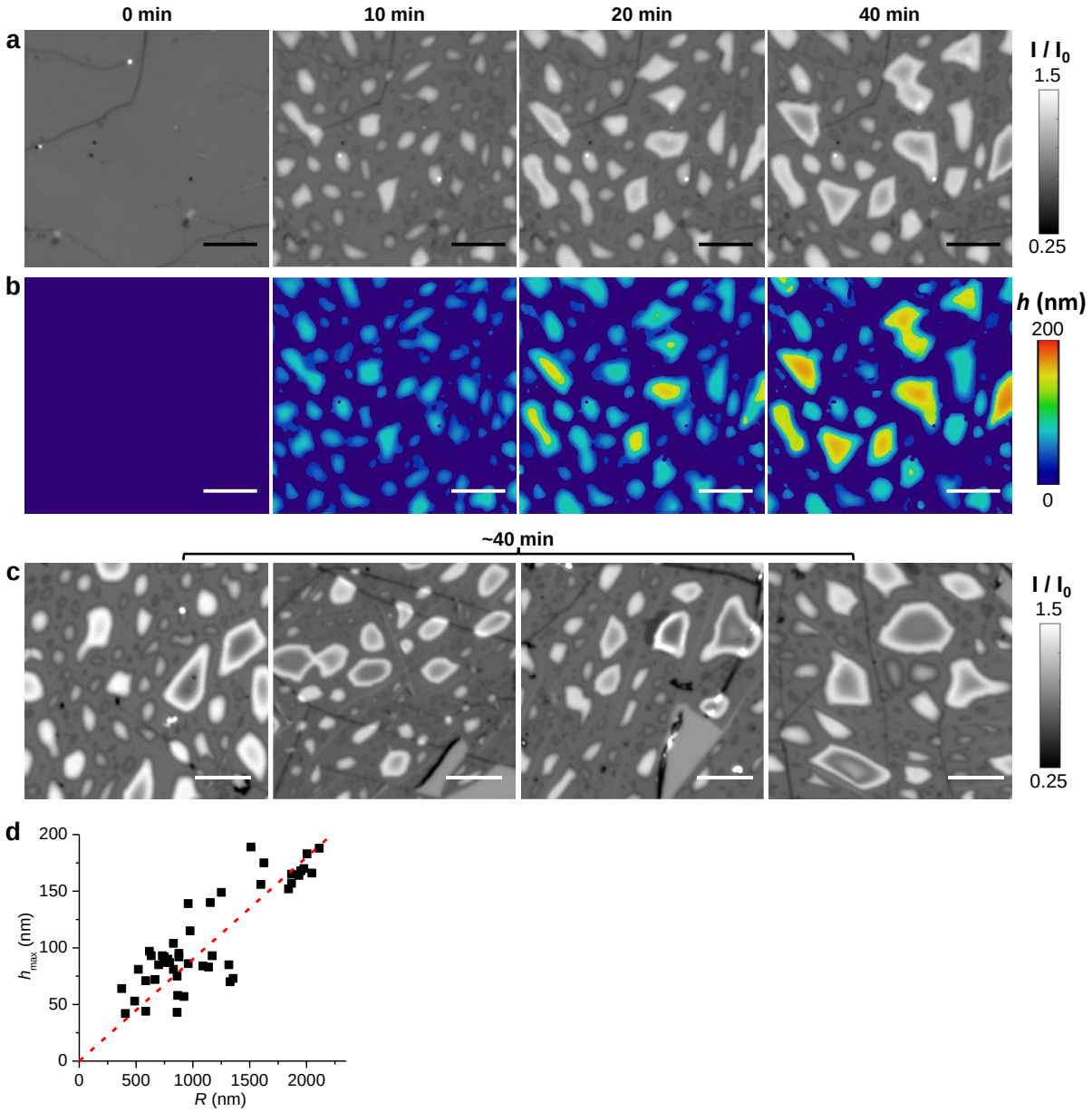

Figure 21. Additional examples for monolayer graphene sample on glass in 0.1 M HCl. (a) Experimental *in situ* IRM image series for the blistering process of another sample. (b) Converted blister height map. (c) Representative IRM images for samples after the same ~40 min 0.1 M HCl treatment on different days. (d) Summary of height-radius relationship for different blisters across three samples. Radii were calculated from the mean dimensions at the blister bases. Red dash line: slope of 0.09. Scale bars (a-c): 5 µm.

As the system involved only an HCl solution and that the island edges exhibited gradual changes in IRM signal, we reasoned that the islands were graphene blisters/bubbles[69] that locally delaminated from the glass surface (schematic in Figure 20a) and hence altered the IRM signal, rather than surface depositions as we previously examined for other systems.[53] Yet, the spontaneous formation of these blisters on the flat glass surface differs from previous experiments in which engineered substrate geometries are employed to induce bubbles.[70,72-74] Meanwhile, the

dynamic nature of these blisters further contrasts with the relatively static bubbles and surface adlayers trapped between graphene and substrates reported in previous studies.[69,71,75-83,92-94] Instead, here graphene started as a regular, flat layer stable on the glass surface, yet the introduction of 0.1 M HCl induced the fast, spontaneous generation of blisters, and such blisters rearranged dynamically over time.

Theoretical modeling (Materials and methods) showed that if we assumed that the blisters enclosed aqueous solutions, the IRM readout, as presented as local light intensity I divided by the intensity at a direct substrate-solution interface I_0 (I/I_0), would initially drop from ~0.75 to 0.69 as the blister height increases to ~15 nm (Figure 20b). Subsequently, the signal would rapidly rise to ~1.37 as the blister height increases to ~115 nm, when the signal would drop again with further blister growth (Figure 20b). As we examined the IRM signal time traces of different growing blisters, we observed trends consistent with the above-predicted bounds (Figure 22). In contrast, if the blisters enclosed gas, theory predicts that the IRM signal I/I_0 would rise dramatically, reaching ~28 at a blister height of ~130 nm before the signal bounces back (Figure 22), drastically different from our experimental observations. Simulated IRM images of solution-enclosed graphene blisters of varying maximal heights, accounting for the diffraction-limited optical resolution, further showed good agreement with the experimental data (Figure 20c,f-h, and Figure 23).

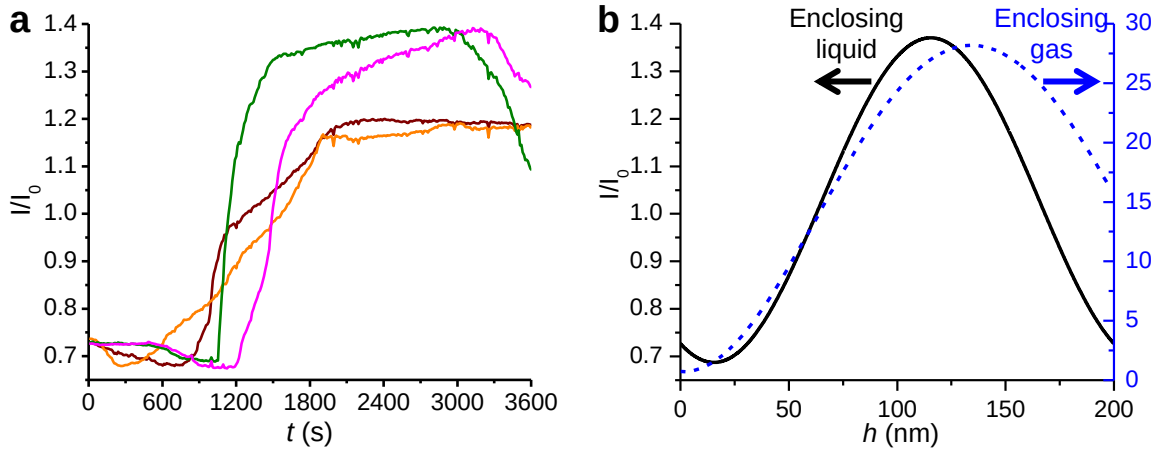

Figure 22. (a) IRM signal time traces for 4 representative blisters in Figure 20. (b) Comparison of the theoretical predicted IRM signals for blisters enclosing solution (black; y-scale on the left) or gas (blue dashed line; y-scale on the right for the much larger values).

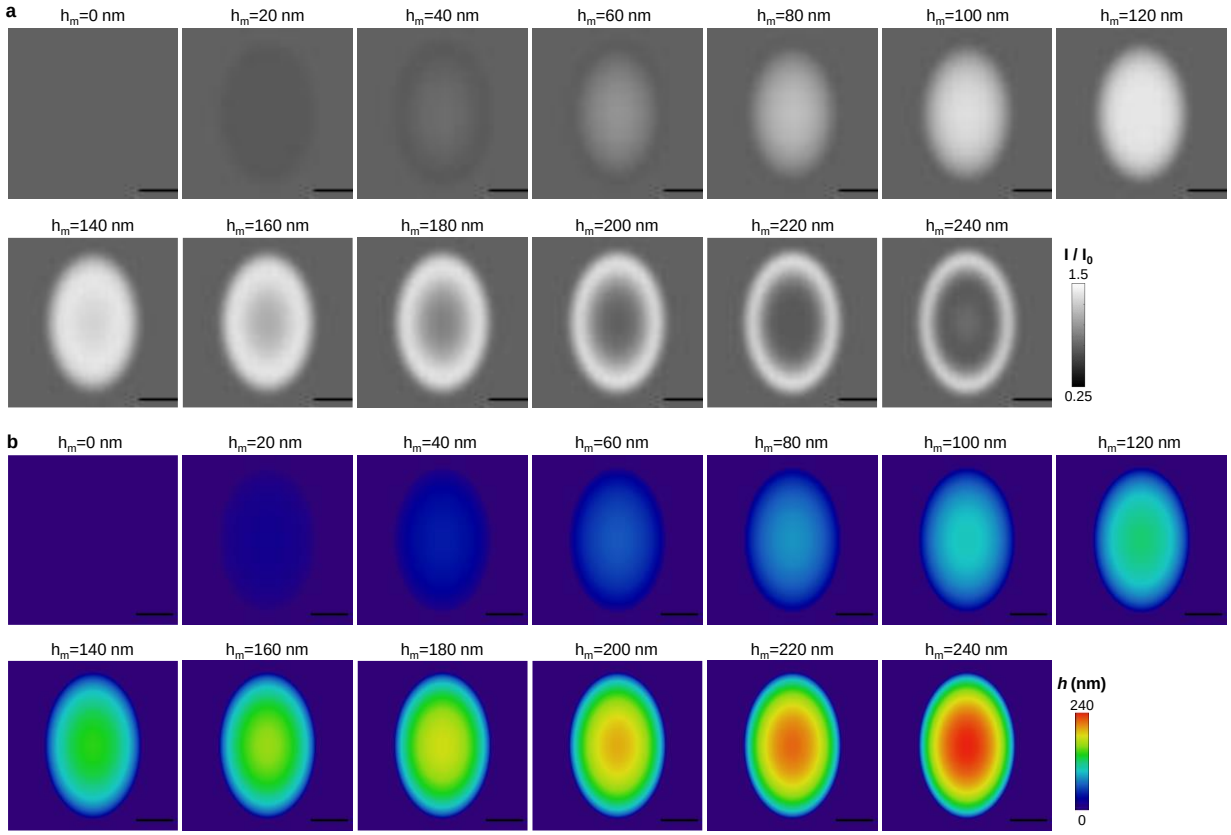

Figure 23. Simulated IRM images. (a) Simulated IRM images of solution-enclosed monolayer graphene blisters with maximal heights h_m of 0-240 nm, presented on the same contrast scale as the experimental data in Figure 1d. (b) The simulated height maps. Scale bars: 1 μm.

Thus, our IRM data indicate the spontaneous generation of blisters enclosing aqueous solutions between the graphene monolayer and the substrate. To further examine this possibility, we removed the top solution as we continued recording IRM images (Figure 24). The originally bright blister features turned dark with low I/I_0 values, as expected for solution-enclosed graphene exposed to air (Figure 24). The blisters quickly shrank and disappeared within seconds, indicating fast evaporation of the nanoscopic water. This dynamic behavior again contrasts with the relative static graphene-trapped bubbles and surface adlayers noted in previous studies.[69,71,75-83,92-94] We further found that after the blisters were equilibrated with a NaCl solution, they shrank much slower in the air and maintained finite volumes over 30 min (Figure 24). This observation suggests that when the solute cannot evaporate, the blisters retain a concentrated solution in equilibrium with the ambient water vapor. Together, our results indicated that the blisters enclosed the applied solutions in the experiment.

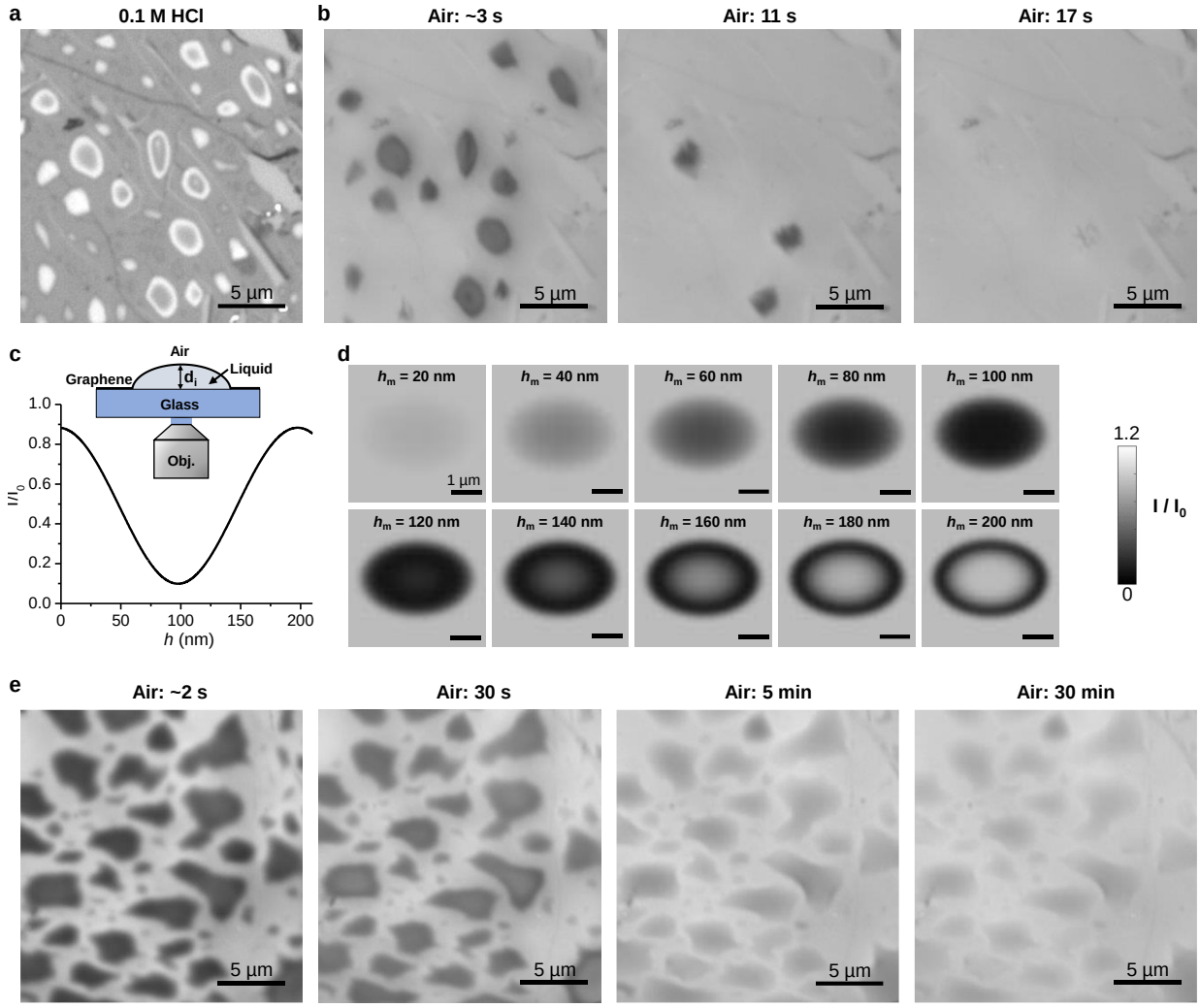

Figure 24. IRM monitoring of the evaporation of blister-enclosed liquids in the air. (a) IRM image of a monolayer graphene sample on glass in 0.1 M HCl, showing the generation of blisters after ~30 min. (b) IRM images of the same sample, after removing the top solution to expose the graphene surface to the air, at 3, 11, and 17 s. The blisters quickly shrank and disappeared. (c) Theoretically predicted IRM contrast (λ = 532 nm) versus local blister heights for solution-containing monolayer graphene blisters exposed to the air. Inset: schematic of the imaging geometry. (d) Simulated IRM images based on (c) for air-exposed graphene blisters of different heights, presented on the same contrast scales as the experimental data in (b,e). (e) IRM image sequence for a sample in which blisters were generated with a solution containing 0.8 M HCl and 0.2 M NaCl. The sample was equilibrated with a 1 M NaCl solution for ~1 h, and then exposed to the air. The blisters only shrank moderately after 30 s, and retained finite volumes after 30 min. Comparing (e) with the simulated images in (d) suggests that blisters of ~150 nm initial height shrank to ~40 nm height over the 30 min period.

By following the time traces and comparing them with our prediction in Figure 20b, we converted the IRM data into local height maps of the blisters (Figure 20e and Figure 21). This showed that the blisters grew to heights of ~50 nm in 15 min, ~100 nm at 30 min, and up to ~200 nm at 60 min. The bases of the blisters also grew wider over time to up to a few micrometers. Thus, the blisters

were still quite flat, as illustrated by the cross section in Figure 20i. Plotting the height versus radius of different blisters showed a positive correlation with a slope of ~0.09 (Figure 21). This aspect ratio is comparable to previous liquid-trapped graphene bubbles/blisters on substrates.[75,77]

We further examined the behavior of few-layer graphene, utilizing the occasionally found multilayer islands in our dominantly monolayer samples (Figure 25). Interestingly, upon acid treatments, blisters were also generated between the multilayers and the substrate, and they were often larger than those at monolayers. This result may be linked to previous findings that the substrate adhesion energy of graphene is ~50% stronger for the monolayer than multilayers.[72]

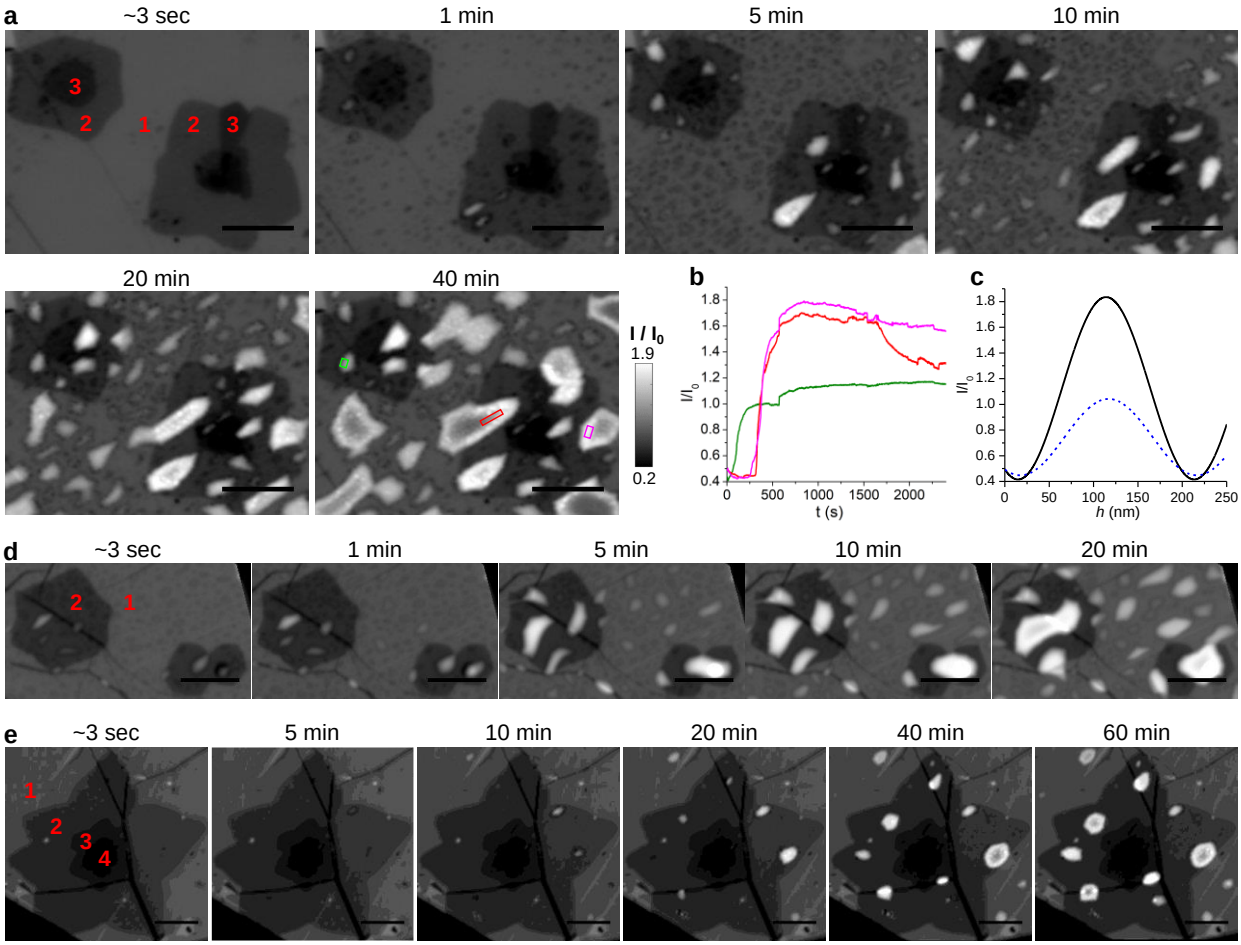

Figure 25. IRM monitoring of acid-induced blisters for multilayer graphene on glass. (a) Representative IRM image sequence for a sample immersed in 1 M HCl. Red "1", "2", and "3" mark the local number of graphene layers. (b) IRM signal time traces for three bilayer regions marked by the color boxes in the last panel of (a). (c) Theoretically predicted IRM signal for bilayer graphene on glass as a function of the local blister height *h*, for solutions being trapped between the glass substrate and the bilayer (black line) vs. between the two graphene layers (blue dashed line). The experimental IRM signals are consistent with blisters >100 nm in height that trapped the solution between the bilayer and the glass substrate. (d) Results from another sample under identical conditions. (e) Results from another sample immersed in a 0.01 M HCl solution. Scale bars (a,d,e) : 5 μm.

3.2.2 Spontaneous graphene blistering occurs under acidic conditions

To understand what factors led to the above fast spontaneous generation of blisters, we examined graphene samples in HCl solutions of different concentrations (Figure 26, and Figure 27). We thus found that when compared to the above-discussed blister dynamics in the 0.1 M HCl (pH = 1) solution at the ~10 min time scales, 1 M HCl (pH = 0) led to the instantaneous generation of nanoscale blisters at high densities in seconds, which grew rapidly and coalesced with each other in ~1 min, so that at 5 min, the system stabilized toward big blisters a few micrometers in lateral size and ~200 nm in height (Figure 26a). In contrast, in the 0.01 M HCl (pH = 2) solution, the generation of blisters was substantially slower and less abundant (Figure 26a). The pH = 3 and 5 solutions generated no blisters over 40 min (Figure 26b). We also compared results with pH<1 H_2SO_4 and *p*-toluenesulfonic acid solutions, and similarly observed blister generation (Figure 28). Meanwhile, a pH~5 solution of Na_2SO_4 and basic conditions with 0.1 M (pH = 13) and 1 M (pH = 14) NaOH solutions did not produce graphene blisters (Figure 26b and Figure 28). Thus, graphene blisters are induced under acidic conditions of pH<~2.

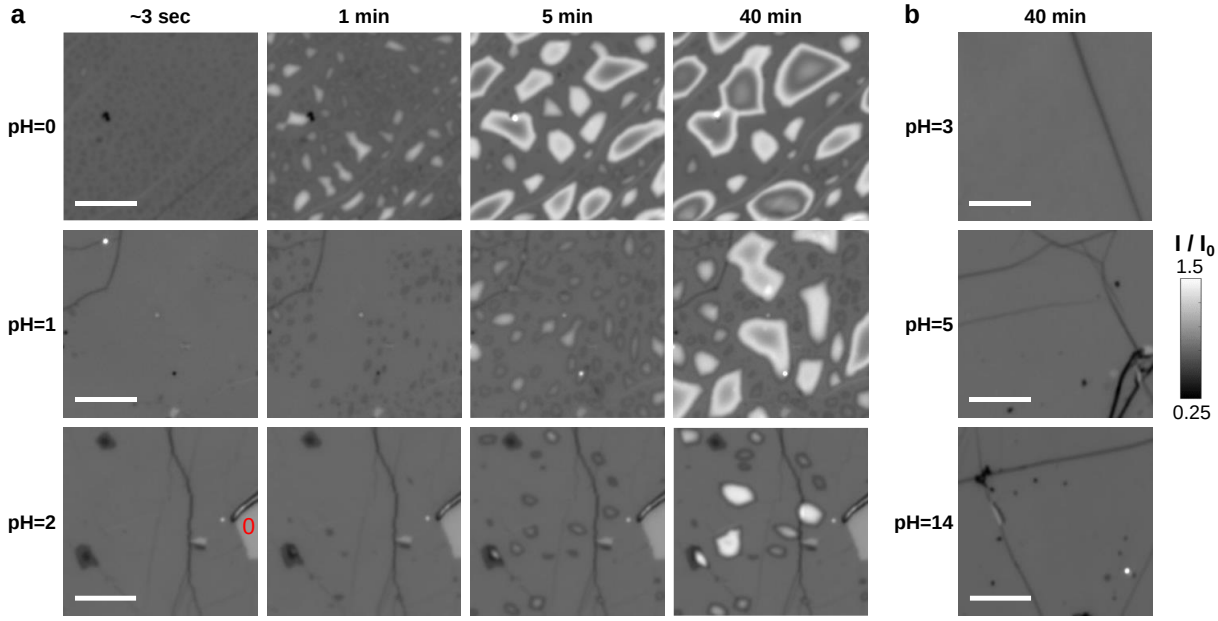

Figure 26. pH dependence of blister generation for graphene on the glass surface. (a) *In situ* IRM images of monolayer graphene on glass submerged in pH = 0, pH = 1, and pH = 2 HCl solutions, at different time points. (b) IRM images for similar samples after 40 min immersion in a pH = 3 HCl solution, pH ~5 MilliQ water, and a pH=14 NaOH solution. Scale bars: 5 μm.

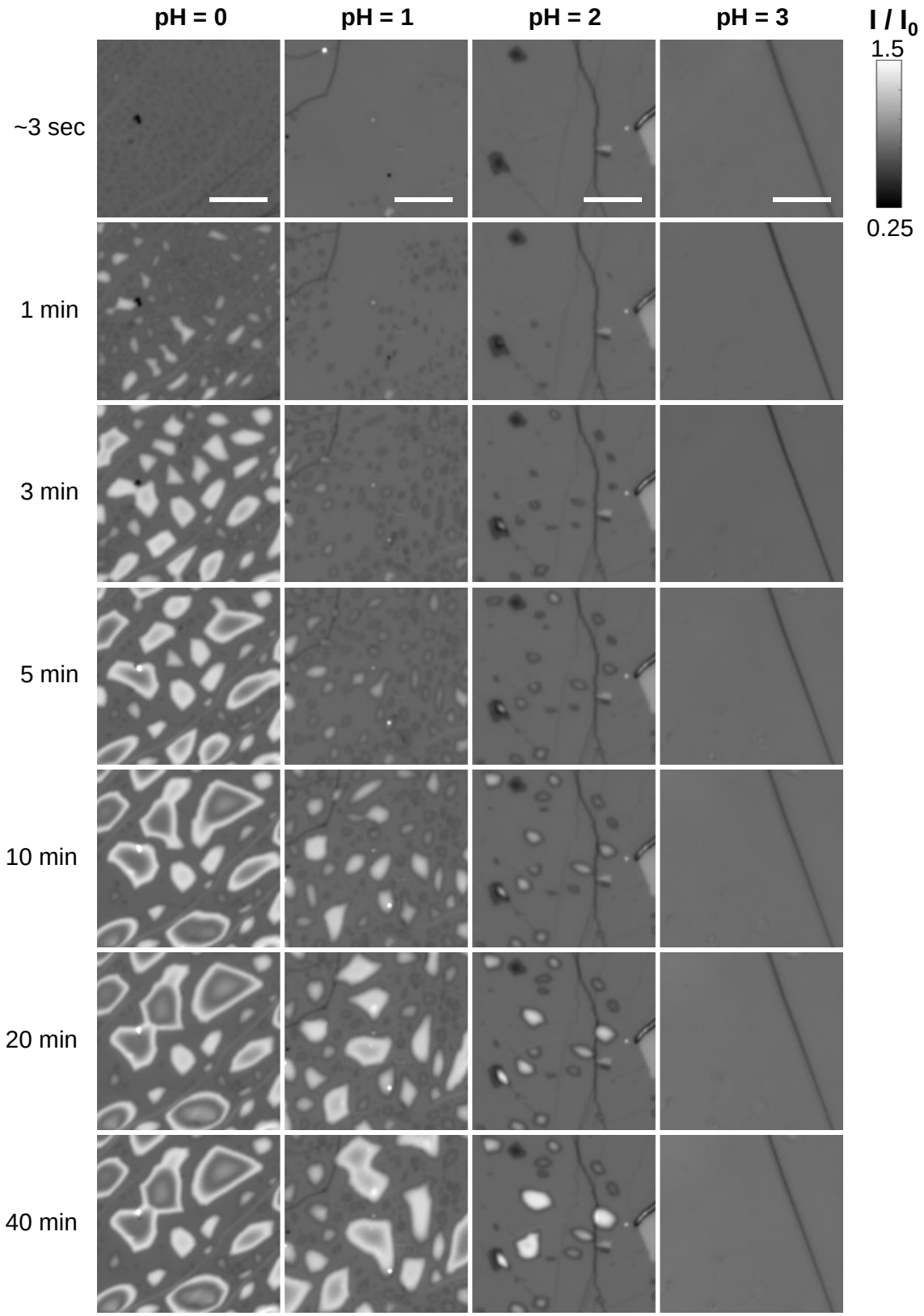

Figure 27. Additional *in situ* IRM image sequences of monolayer graphene on glass in pH = 0, pH = 1, pH = 2, and pH = 3 HCl solutions for different amounts of time. Scale bars: 5 μm.

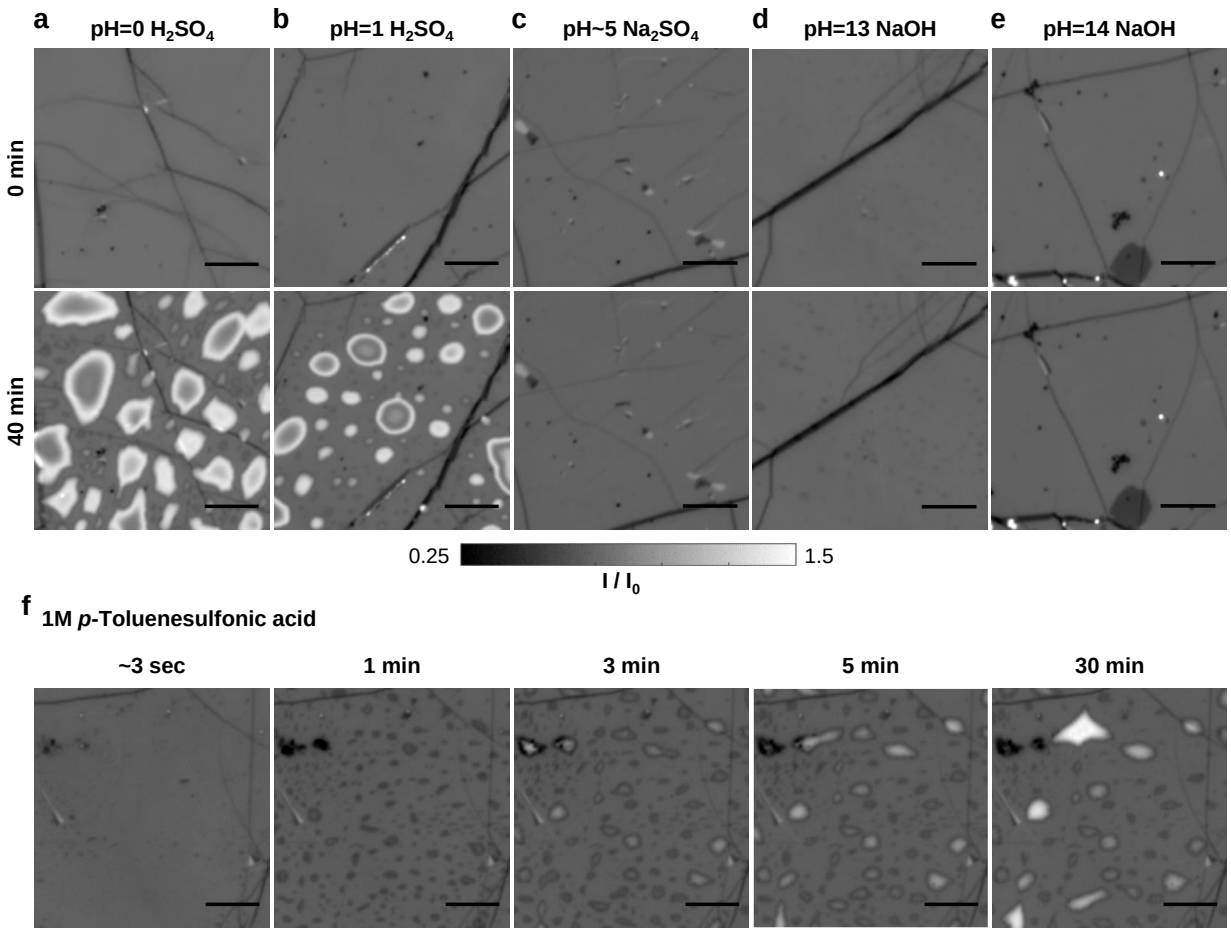

Figure 28. IRM images of monolayer graphene on glass after different chemical treatments besides HCl. (a-e) Before (top row) and after (bottom row) 40 min immersion in pH=0 H_2SO_4 (a), pH=1 H_2SO_4 (b), pH~5 Na_2SO_4 (c), pH=13 NaOH (d), and pH=14 NaOH (e) solutions. (f) Time sequence after immersion in a 1 M solution of *p*-toluenesulfonic acid: blister growth appeared slower than with HCl and H_2SO_4, possibly due to the larger size of the *p*-toluenesulfonic acid molecule. Scale bars: 5 μm.

3.2.3 Spontaneous graphene blistering occurs on hydrophilic, but not hydrophobic, substrates

We next investigated the effects of the substrate. The as-received glass coverslips, which we used above after sonication in isopropanol and water, were hydrophilic. After treating the coverslips with a piranha solution (1:3 H_2O_2:H_2SO_4), the surface became highly hydrophilic, and we observed a similar fast generation of graphene blisters on this substrate in 0.1 M HCl (Figure 29a). Functionalizing the glass surface with (3-aminopropyl)triethoxysilane (APTES), which altered the hydrophilic glass surface from negatively charged to positively charged, did not affect the blister-generating capability (Figure 29a). In contrast, functionalizing the glass surface with chlorotrimethylsilane (TMCS), which yielded a hydrophobic surface, led to the full suppression of blisters in 0.1 M HCl (Figure 29a). Similarly, we found that for graphene deposited on the hydrophobic surface of polychlorotrifluoroethylene (PCTFE; Aclar) films, no blisters were generated (Figure 29a). Thus, blisters are generated for graphene deposited on hydrophilic but not hydrophobic surfaces. We also examined glass coverslips functionalized with

trichloro(1H,1H,2H,2H-perfluorooctyl)silane: the surface was both hydrophobic and oleophobic, onto which graphene did not adhere adequately but crumbled into sub-micrometer pieces (Figure 30).

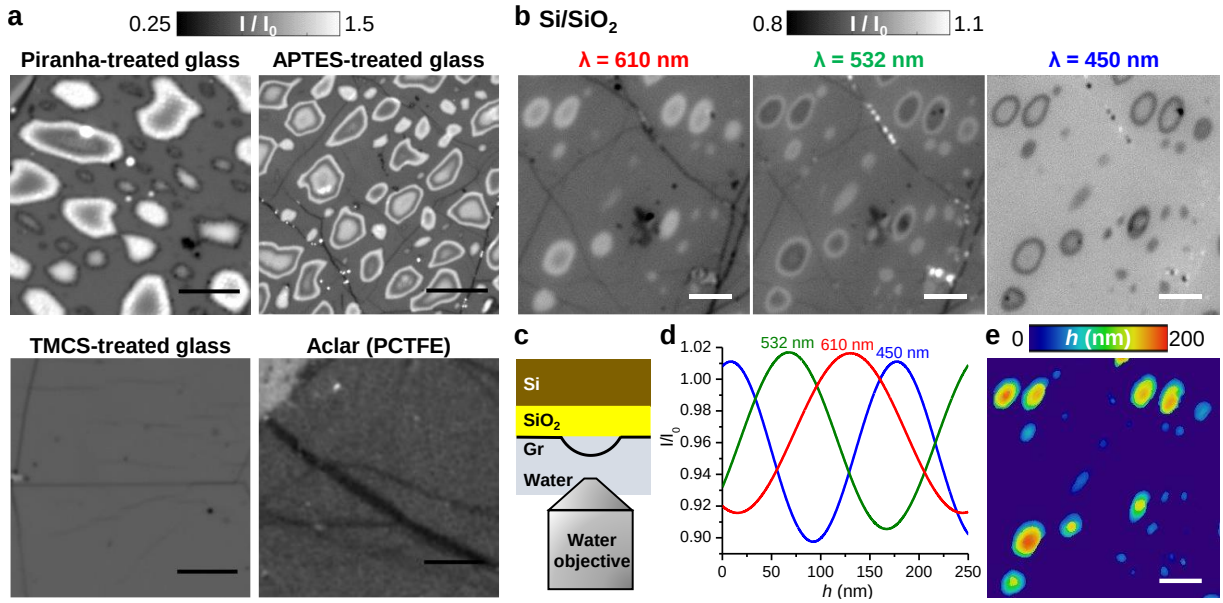

Figure 29. Spontaneous graphene blistering on different substrates. Monolayer graphene was deposited on different substrates and then immersed in 0.1 M HCl for ~1 h. (a) IRM images for graphene on piranha-treated glass, APTES-treated glass, TMCS-treated glass, and Aclar (PCTFE) film. (b) Reflected light microscopy images of graphene on a Si wafer coated with a ~290 nm layer of thermally grown oxide, under 610, 532, and 450 nm illuminations. For both imaging modes, signals are presented as the local light intensity I divided by the intensity at the direct substrate-solution interfaces I_0. (c) Sample geometry for the reflected light microscopy of graphene on Si/SiO_2. (d) Predicted image signals at the three wavelengths as a function of the water-enclosed blister height h. (e) Blister height map converted from the images in (b). Scale bars: 5 μm.

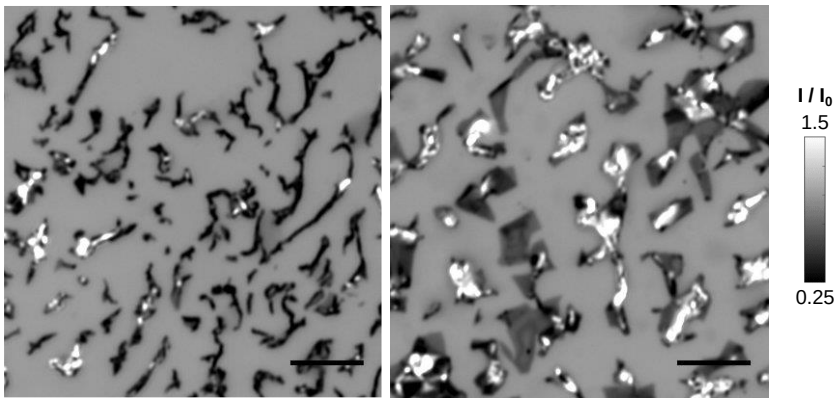

Figure 30. Typical IRM images for graphene deposited on glass surfaces functionalized with trichloro(1H,1H,2H,2H-perfluorooctyl)silane, which were both hydrophobic and oleophobic due to the low surface energy of the fluorocarbon. Graphene did not adhere adequately but crumbled into sub-micrometer fragments. Scale bars: 5 μm.

We next examined the hydrophilic substrate of thermal oxide-coated silicon (Si/SiO_2) wafers, an often-used device substrate. As the substrate is opaque, we changed our imaging strategy, so that the sample was immersed in a 0.1 M HCl solution for ~1 h, rinsed with water, and then mounted upside-down for imagining with a water-immersion objective lens (Figure 29c). The resultant reflected light microscopy images visualized numerous blisters. Here, as the ~290 nm SiO_2 layer differently interfered with light of different wavelengths, we illuminated the sample at 610, 532, and 450 nm, respectively, and obtained images of varying contrasts (Figure 29b). Theory predicted different blister height-dependent signal evolution trends under the three wavelengths (Figure 29d). These predictions, as well as simulated blister images (Figure 31), matched well with our experimental observations (Figure 29b and Figure 31). We hence converted the triplex reflected-light micrograph into a heightmap, showing blisters up to ~200 nm in height (Figure 29e). Thus, comparable blisters were generated for graphene on the commonly used Si/SiO_2 substrate, albeit the dynamics are difficult to monitor *in situ* on this opaque substrate.

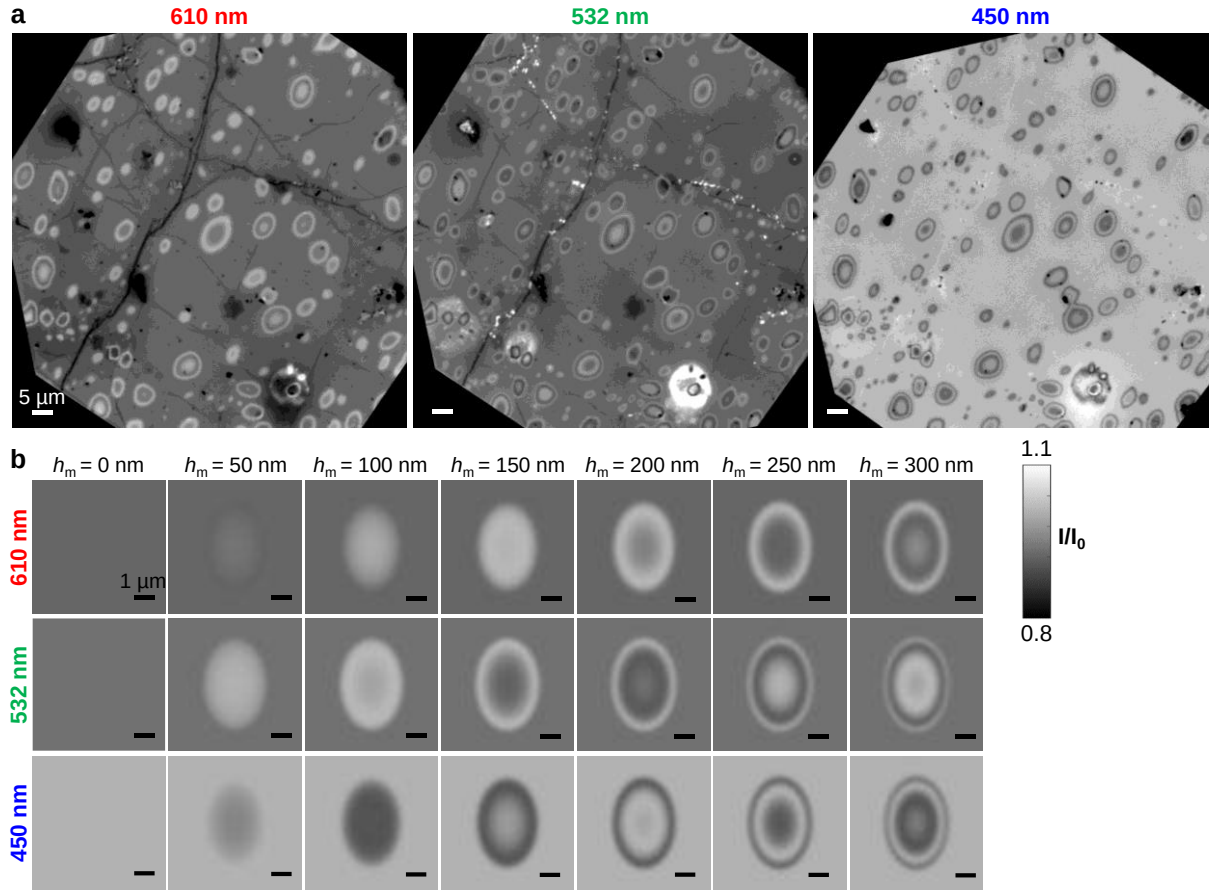

Figure 31. Reflected light microscopy of graphene blisters on Si/SiO_2. (a) A larger view of the sample shown in Figure 3b, under 610, 532, and 450 nm illuminations. (b) Simulated images at the three wavelengths for blisters of different maximal heights.

3.2.4 Graphene blisters are fast modulated by the solution osmotic pressure as graphene acts as a semipermeable membrane

As we next examined the stability of the graphene blisters in different solutions, we found that the blisters expanded and shrank reversibly under different solute concentrations, and the behavior followed the osmotic pressure of the solution. Starting with blisters generated with 1 M HCl (Figure 32ab), we found that as we replaced the sample solution with water, the blisters quickly expanded in volume at ~10 s time scales, so that the expanded blisters gradually merged with each other (arrowheads in Figure 32cd).

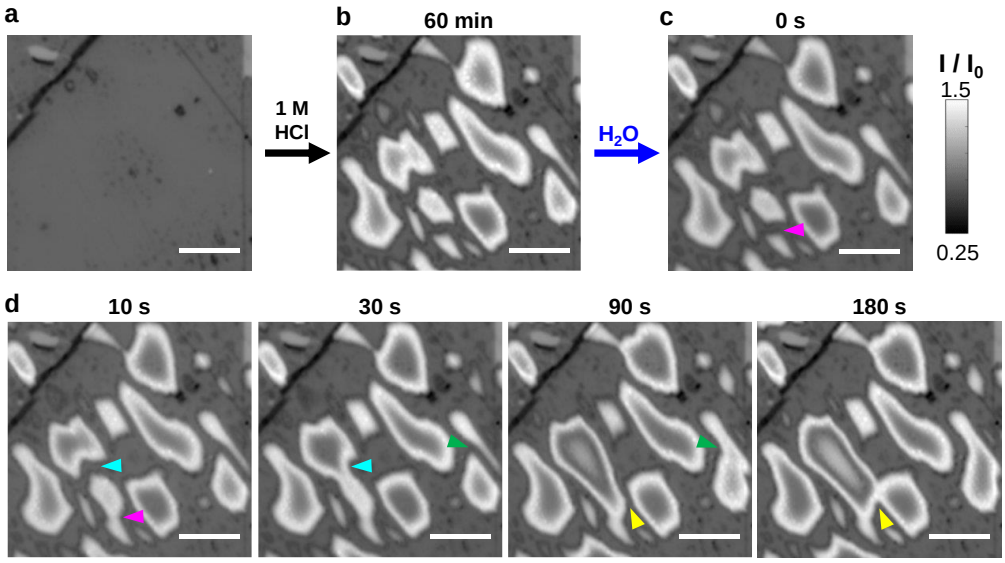

Figure 32. Fast expansion of blister volumes after changing the acid solution to water. (a,b) IRM images of monolayer graphene on glass, before (a) and after (b) immersed in 1M HCl for 1 h. (c) The top solution was changed to MilliQ water. (d) *In situ* IRM image sequences after different amounts of time, showing notable swelling of blisters. Color arrowheads point to blister-merging events between the shown image sequences. Scale bars: 5 μm.

To examine whether this dynamic behavior could be driven by changes in solute concentration and thus osmotic pressure, we examined a sample in which blisters were generated with a solution containing 0.8 M HCl and 0.2 M NaCl (Figure 33a). Replacing the top medium with an isotonic solution of 1 M NaCl did not notably alter the blisters over 17 min (Figure 33b). Next changing the medium to 6 M NaCl led to an initial flash of high IRM signal due to the high refractive index of the 6 M NaCl solution, yet the IRM signal then plummeted as the blister volumes shrank drastically in ~30 s (Figure 33c). Reverting the medium to 1 M NaCl led to rapid regrowth of the blisters, so that the system largely recovered the original blister volumes in ~3 min (Figure 33d).

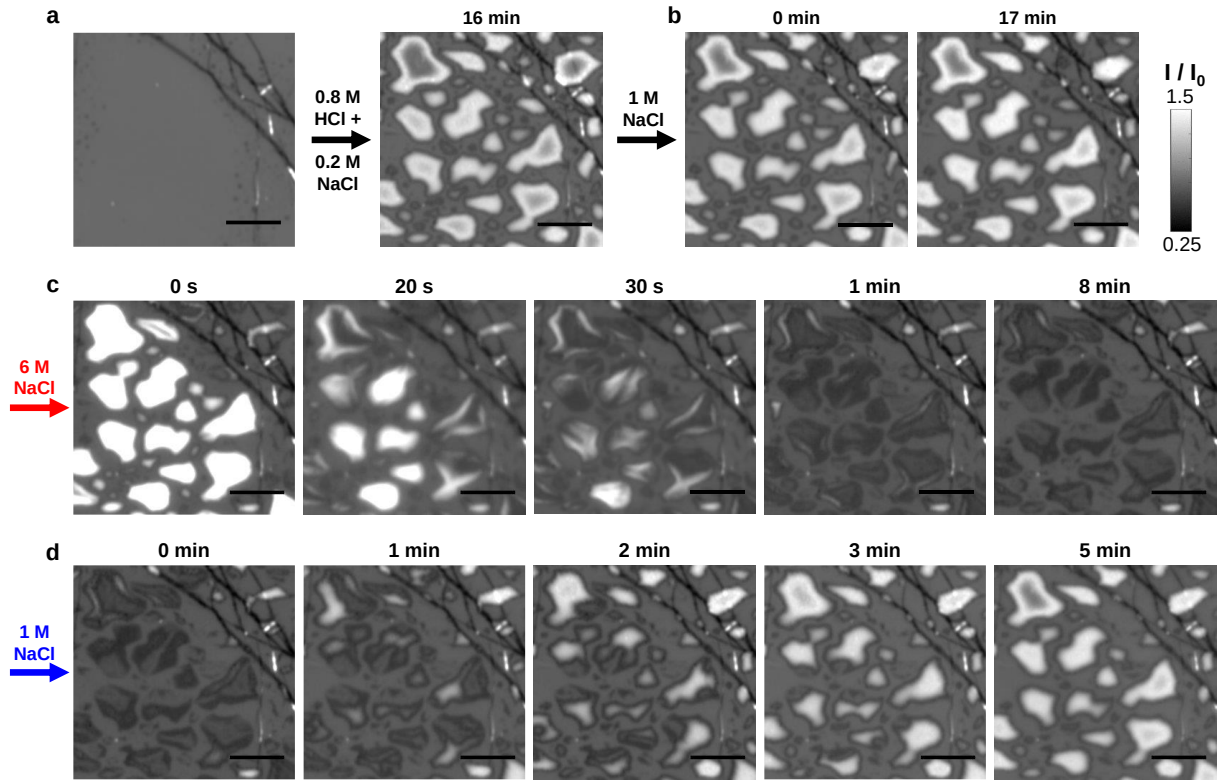

Figure 33. Reversible fast modulation of graphene blisters *via* solution osmotic pressure. (a) IRM images of monolayer graphene on glass, before (a) and after (b) immersed in a solution of 0.8 M HCl + 0.2 M NaCl for 16 min. (b) The top medium was changed to 1 M NaCl, with little changes in blister shapes observed over 17 min. (c) The top medium was next changed to 6 M NaCl, and IRM recorded a fast shrinkage of blister volumes. (d) The top medium was next reverted to 1 M NaCl, and IRM recorded a fast recovery of blister volumes. Scale bars: 5 μm.

The above results suggest that in our system, the acid-treated graphene behaved as a semipermeable membrane[73,84-90] that more readily passed water molecules than the solute ions. Consequently, increased solute concentration and hence osmotic pressure of the solution withdrew water from the blisters to shrink their volumes, whereas decreased osmotic pressure of the solution drove more water into the blisters and induced blister expansion.

To further probe the semipermeable properties of the blisters, we next examined osmotic effects over longer timescales. Interestingly, as we applied 1 M NaCl to graphene blisters generated with 0.1 M HCl, whereas rapid shrinkage occurred at the second-to-minute timescale as water flew out under the higher osmotic pressure, the blisters gradually grew back after ~30 min (Figure 34). This result suggests the gradual diffusion of the NaCl solute into the blisters over the longer timescale. In contrast, as we added into the top medium the fluorescent dye Sulforhodamine 101, fluorescence microscopy showed reduced Sulforhodamine 101 signal at the graphene blisters, and this dye-exclusion effect was well maintained over 2 h (Figure 35). Together, our results indicated that the blisters allowed relatively free passing of water (~10 s timescales) and impeded passing of the NaCl solute (~10 min timescales), but effectively blocked the passing of the larger Sulforhodamine 101 molecule.

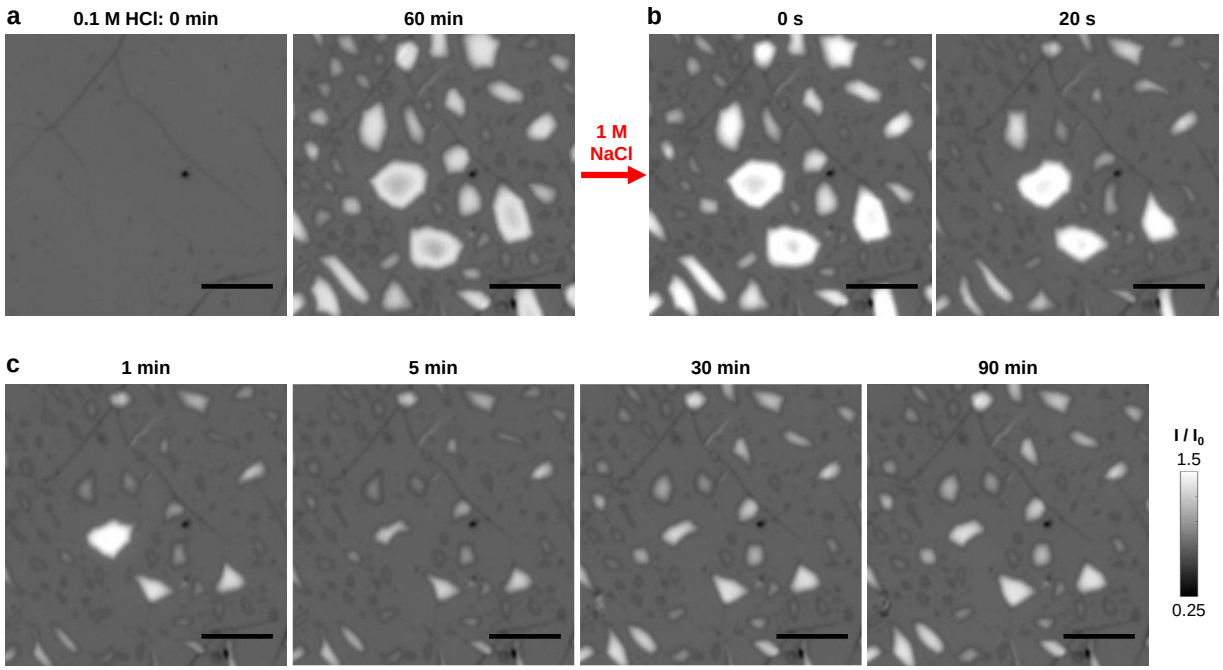

Figure 34. IRM images suggest the slow passing of NaCl through the graphene blisters. (a) Blisters were induced with 0.1 M HCl over 60 min. (b) Changing the top medium to 1 M NaCl led to fast shrinkage of blisters in seconds as water flew out under the higher osmotic pressure. (c) After reaching the lowest volumes at ~5 min, the blisters gradually grew back after ~30 min, suggesting gradual diffusion of the NaCl solute into the blisters over the long timescale. Scale bars: 5 µm.

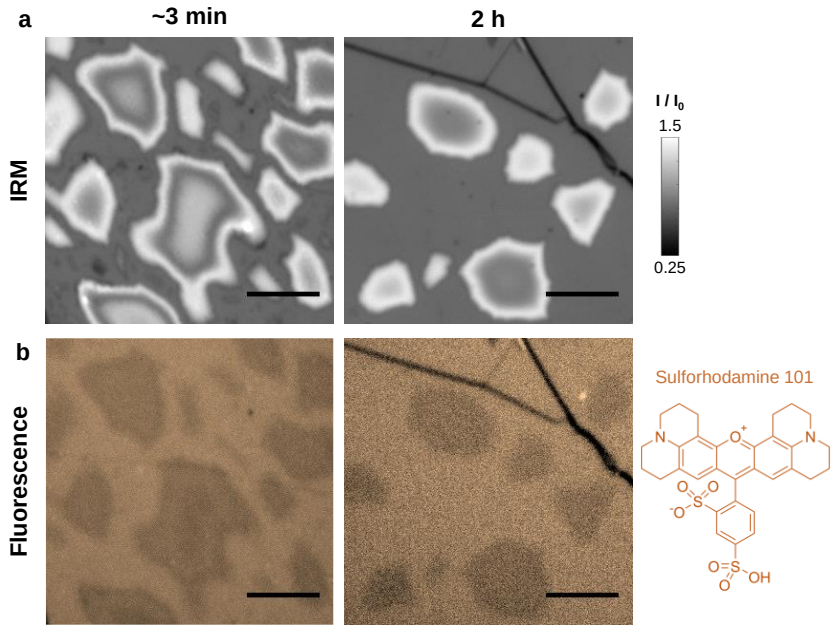

Figure 35. IRM (a) and fluorescence microscopy (b) images for graphene blisters (generated through 1 M HCl treatment for 1 h, and then rinsed with water) in a 10 µM solution of the fluorescent dye Sulforhodamine 101, ~3 min and 2 h after adding the dye. Scale bars: 5 µm.

3.3 Conclusion

In summary, with the exceptional contrast and *in situ* imaging capabilities offered by IRM, we discovered the fast, spontaneous generation of solution-enclosed blisters for graphene on common substrates. We thus showed that at pH<~2, nanoscale to micrometer-sized graphene blisters, up to ~100 nm in height, were universally generated on hydrophilic surfaces, including the popular Si/SiO_2 substrates, but not on hydrophobic substrates. The blister-generation process was highly dynamic, with IRM-visualized growth, merging, and reconfiguration occurring at second-to-minute time scales, and we further showed that in such processes, graphene behaved as a semipermeable membrane so that the blister volumes were readily modulated by the osmotic pressure of the solution.

Our intriguing observations may be explained below. Acidic conditions create atomic defects in graphene.[95,96] Raman spectroscopy (Figure 36) showed no noticeable generation of *D* peaks but enhanced hole doping after acid treatments, consistent with that expected from acid-induced defects and trapped water.[97-99] Thus, a moderate level of atomic defects creates a semipermeable membrane. Subsequently, if the substrate is hydrophilic, capillary action draws the aqueous solution into the narrow space between the graphene and substrate surfaces, hence initiating local delamination and dynamic reconfiguration of the inserted liquid to form blisters. The resultant blisters followed a height-to-radius aspect ratio of ~0.09, comparable to previous liquid-trapped graphene bubbles/blisters.[75,77] We further found the blisters to be larger at multilayers, a result attributable to the lower substrate adhesion of graphene multilayers than monolayers,[72] which likely facilitates local delamination. In contrast, a hydrophobic substrate disfavors water insertion and may more strongly bond the (relatively hydrophobic) graphene surface to prevent delamination, so blisters are not formed. Interestingly, we found that on the hydrophilic glass surface, chemical oxidated graphene no longer formed blisters (Figure 37), possibly because the oxidized graphene was more hydrophilic and thus adhered more strongly to the hydrophilic substrate.

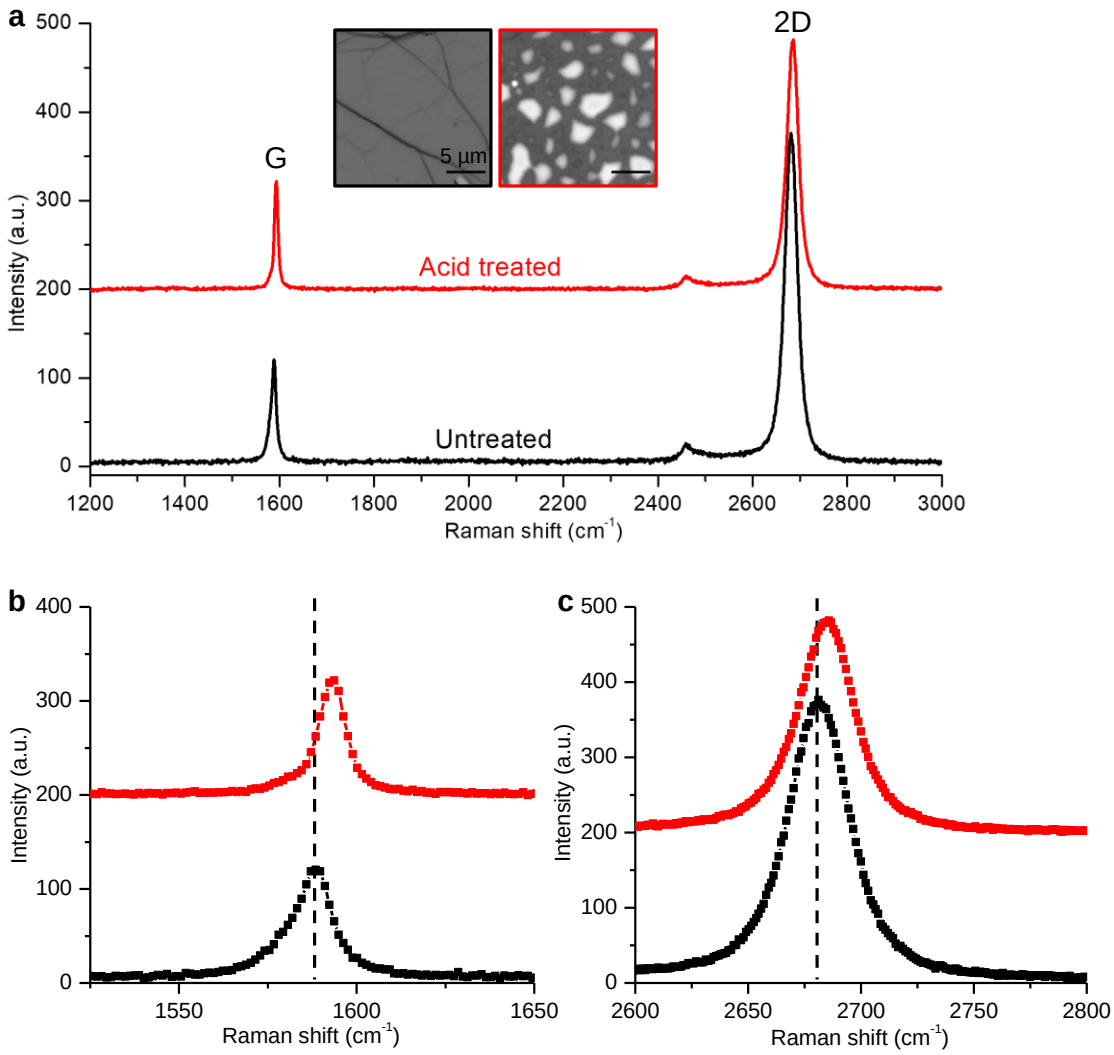

Figure 36. Raman spectra of typical graphene samples in this work before (black) and after (red) treatment with 1 M HCl for 1 h. (a) Full spectra, showing no noticeable generation of the D peak but a reduced 2D/G peak-height ratio after the acid treatment. (b,c) Zoom-ins of the G and 2D bands, showing substantial blueshifts after the acid treatment. Together, these results are consistent with enhanced hole doping owing to the formation of a low level of acid-induced atomic defects.

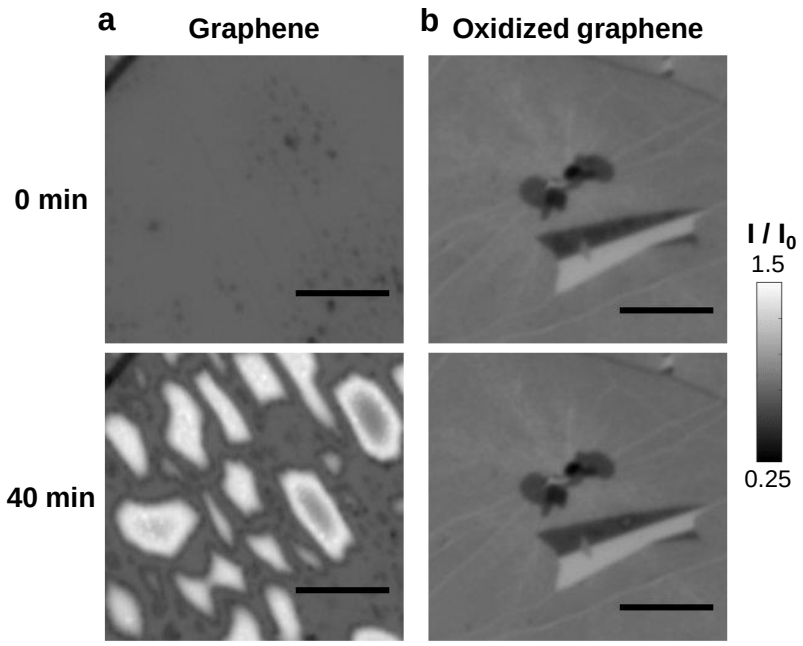

Figure 37. IRM images of regular graphene (a) and oxidized graphene (b; produced by 1-h Clorox treatment[14]) on glass surfaces before (top panel) and after (bottom panel) 40 min immersion in 1 M HCl. Scale bars: 5 μm.

As yet another demonstration of the power of IRM for *in situ* graphene characterization, our work thus sheds new light on graphene properties, both in terms of its blister-forming capabilities and its semipermeable behavior. The observed spontaneous formation of blisters in acidic solutions further carries practical implications for understanding the stability of graphene devices under different operational conditions.

3.4 Materials and methods

Graphene sample preparation. For most samples, glass coverslips (#1.5, 50×24 mm, VWR, 16004-322) were cleaned by sonication in isopropanol for 10 min, followed by sonication in MilliQ water for 10 min. For evaluating the behavior of different substrates (Figure 29): For piranha treatment, coverslips were heated in a 1:3 H_2O_2:H_2SO_4 solution for 20 min, and thoroughly rinsed with MilliQ water. For APTES functionalization, the piranha-treated coverslips were immersed in a 10% (v/v) (3-aminopropyl)triethoxysilane (Sigma 440140) ethanol solution for 1 h. After that, the coverslips were rinsed with ethanol and MilliQ water. For TMCS functionalization, the piranha-treated coverslips were placed in a chamber with chlorotrimethylsilane (Sigma 92361) vapor for 5 min. For trichloro(1H,1H,2H,2H-perfluorooctyl)silane functionalization, the piranha-treated coverslips were incubated in a chamber with trichloro(1H,1H,2H,2H-perfluorooctyl)silane (Fisher Scientific AAL1660609) vapor at 55 ˚C for 10 min. Aclar 33C (polychlorotrifluoroethylene) film of 0.2 mm thickness (Ted Pella) was cleaned by sonication in isopropanol for 10 min, followed by sonication in MilliQ water for 10 min. Single-side-polished silicon wafers with a ~290 nm thermal oxide layer (Si/SiO_2; University Wafer) was piranha-treated and water-rinsed as above. CVD-grown graphene on copper foils (ACS Material or Graphene Supermarket) was spin-coated with a ~150 nm layer of poly (methyl methacrylate) (PMMA), and wet-transferred with a modified RCA cleaning process[100] onto the above substrates. PMMA was removed by immersion in acetone

and isopropanol. Raman spectroscopy was performed with a Horiba LabRAM HR Evolution Spectrometer with a 100x objective lens using 532-nm laser excitation and an 1800 lines/mm grating.

Optical microscopy characterizations. IRM, reflected light microscopy, and fluorescence microscopy were performed on an Olympus IX73 inverted epifluorescence microscope with a white light source (Olympus U-HGLGPS), as described previously.[4,101] IRM and fluorescence microscopy were performed using an UplanFl 100× oil-immersion objective (numerical aperture ~0.9 with iris diaphragm). Reflected light microscopy was performed using a UplanSapo 60× water-immersion objective (numerical aperture 1.2). For IRM and reflected light microscopy, the dichroic mirror position was mounted with a 50/50 beam splitter (Chroma 21000), and the emission filter position was left empty. For IRM, the excitation filter was D532/10x (Chroma). For reflected light microscopy, the excitation filter was FF01-610/5-25 (Semrock), D532/10x (Chroma), or FB450-10 (Thorlabs). For fluorescence microscopy, the excitation filter, dichroic mirror, and emission filter were ET545/25x (Chroma), zt561rdc-UF1 (Chroma), and ET605/70m (Chroma), respectively. For all microscopy modes, wide-field images were recorded using an Andor Zyla 4.2 sCMOS camera at ~10 frames per second with effective pixel sizes of 65 and 108 nm for the 100× and 60× objective lenses, respectively.

Theoretical modeling of IRM and reflected light microscopy signals. Theoretical modeling of IRM signal on transparent substrates, as well as reflected light microscopy signal on Si/SiO_2 substrates, were performed using the transfer-matrix method for thin films.[4,102]

For IRM signal on transparent substrates, layer configuration is shown in Figure 1a. Incident light of wavelength λ and intensity I_I enters the sample from the substrate side, successively encounters the blister, graphene, and top solution, and leaves as reflected (R) and transmitted (T) light. The refractive indices of the substrate, blister-enclosed content, graphene, and top solution are respectively denoted as n_1, n_i, n_2, and n_3. Here, the complex refractive index of graphene is taken as $n_2 = 2.65-1.27i$.[39,40] The local height of the blister is d_i. Graphene thickness is $d_2 = 0.335m$ nm for m-layers.

The Fresnel coefficients at the substrate-blister, blister-graphene, and graphene-top solution interfaces are respectively: $r_{1i} = \frac{n_1-n_i}{n_1+n_i}$, $t_{1i} = \frac{2n_1}{n_1+n_i}$, $r_{i2} = \frac{n_i-n_2}{n_i+n_2}$, $t_{i2} = \frac{2n_i}{n_i+n_2}$, $r_{23} = \frac{n_2-n_3}{n_2+n_3}$, $t_{23} = \frac{2n_2}{n_2+n_3}$.

The transfer matrices at the three interfaces are $T^{1i} = \frac{1}{t_{1i}}\begin{bmatrix} 1 & r_{1i} \\ r_{1i} & 1 \end{bmatrix}$, $T^{i2} = \frac{1}{t_{i2}}\begin{bmatrix} 1 & r_{i2} \\ r_{i2} & 1 \end{bmatrix}$, and $T^{23} = \frac{1}{t_{23}}\begin{bmatrix} 1 & r_{23} \\ r_{23} & 1 \end{bmatrix}$.

The transfer matrix in the blister is $T^i = \begin{bmatrix} e^{i\alpha} & 0 \\ 0 & e^{-i\alpha} \end{bmatrix}$, where $\alpha = \frac{2\pi}{\lambda} n_i d_i$.

The transfer matrix in graphene is $T^2 = \begin{bmatrix} e^{i\beta} & 0 \\ 0 & e^{-i\beta} \end{bmatrix}$, where $\beta = \frac{2\pi}{\lambda} n_2 d_2$.

The transfer matrix for the system is:

$$T^{13} = T^{1i}T^{i}T^{i2}T^{2}T^{23} = \frac{1}{t_{1i}}\begin{bmatrix}1 & r_{1i}\\ r_{1i} & 1\end{bmatrix}\begin{bmatrix}e^{i\alpha} & 0\\ 0 & e^{-i\alpha}\end{bmatrix}\frac{1}{t_{i2}}\begin{bmatrix}1 & r_{i2}\\ r_{i2} & 1\end{bmatrix}\begin{bmatrix}e^{i\beta} & 0\\ 0 & e^{-i\beta}\end{bmatrix}\frac{1}{t_{23}}\begin{bmatrix}1 & r_{23}\\ r_{23} & 1\end{bmatrix} = \frac{1}{t_{1i}t_{i2}t_{23}}$$
$$\begin{bmatrix}e^{i(\alpha+\beta)} + r_{1i}r_{i2}e^{i(\beta-\alpha)} + r_{i2}r_{23}e^{i(\alpha-\beta)} + r_{1i}r_{23}e^{-i(\beta+\alpha)} & r_{23}e^{i(\alpha+\beta)} + r_{i2}e^{i(\alpha-\beta)} + r_{1i}e^{-i(\beta+\alpha)} + r_{1i}r_{i2}r_{23}e^{i(\beta-\alpha)}\\ r_{1i}e^{i(\alpha+\beta)} + r_{i2}e^{i(\beta-\alpha)} + r_{23}e^{-i(\beta+\alpha)} + r_{1i}r_{i2}r_{23}e^{i(\alpha-\beta)} & e^{-i(\alpha+\beta)} + r_{1i}r_{i2}e^{i(\alpha-\beta)} + r_{i2}r_{23}e^{i(\beta-\alpha)} + r_{1i}r_{23}e^{i(\beta+\alpha)}\end{bmatrix}$$

The reflection coefficient is

$$\mathrm{r} = \frac{T_{21}^{13}}{T_{11}^{13}} = \frac{r_{1i}e^{i(\alpha+\beta)} + r_{i2}e^{i(\beta-\alpha)} + r_{23}e^{-i(\beta+\alpha)} + r_{1i}r_{i2}r_{23}e^{i(\alpha-\beta)}}{e^{i(\alpha+\beta)} + r_{1i}r_{i2}e^{i(\beta-\alpha)} + r_{i2}r_{23}e^{i(\alpha-\beta)} + r_{1i}r_{23}e^{-i(\beta+\alpha)}}$$

Intensity of the reflected light, which is recorded experimentally in IRM images, is thus:

$$I = |r|^2 I_I = \left|\frac{r_{1i}e^{i(\alpha+\beta)} + r_{i2}e^{i(\beta-\alpha)} + r_{23}e^{-i(\beta+\alpha)} + r_{1i}r_{i2}r_{23}e^{i(\alpha-\beta)}}{e^{i(\alpha+\beta)} + r_{1i}r_{i2}e^{i(\beta-\alpha)} + r_{i2}r_{23}e^{i(\alpha-\beta)} + r_{1i}r_{23}e^{-i(\beta+\alpha)}}\right|^2 I_I$$

Intensity without blister ($d_i = 0$; substrate-graphene-solution geometry) is:[4]

$I = \left|\frac{r_{12}e^{i\beta} + r_{23}e^{-i\beta}}{e^{i\beta} + r_{12}r_{23}e^{-i\beta}}\right|^2 I_I$, where $r_{12} = \frac{n_1 - n_2}{n_1 + n_2}$

Intensity without blister and graphene ($d_i = 0$, $d_2 = 0$; a direct substrate-solution interface) is:[4] $I_0 = \left|\frac{n_1 - n_3}{n_1 + n_3}\right|^2 I_I$

For reflected light microscopy signal on Si/SiO_2 substrates, layer configuration of the system is given in Figure 3c. Incident light of wavelength λ and intensity I_I enters the sample from the water side, successively encounters graphene, blister, SiO_2 and Si, and leaves as reflected (R) and transmitted (T) light. The refractive indices of water, graphene, blister, SiO_2 and Si are respectively denoted as n_1, n_2, n_i, n_3, and n_4. The local height of the blister is d_i. Graphene thickness is d_2.
The Fresnel coefficients at the water-graphene, graphene-blister, blister-SiO_2, and SiO_2-Si interfaces are respectively:
$r_{12} = \frac{n_1 - n_2}{n_1 + n_2}$, $t_{12} = \frac{2n_1}{n_1 + n_2}$, $r_{2i} = \frac{n_2 - n_i}{n_2 + n_i}$, $t_{2i} = \frac{2n_2}{n_2 + n_i}$, $r_{i3} = \frac{n_i - n_3}{n_i + n_3}$, $t_{i3} = \frac{2n_i}{n_i + n_3}$, $r_{34} = \frac{n_3 - n_4}{n_3 + n_4}$, $t_{34} = \frac{2n_3}{n_3 + n_4}$.

The transfer matrices at the three interfaces are: $T^{12} = \frac{1}{t_{12}}\begin{bmatrix}1 & r_{12}\\ r_{12} & 1\end{bmatrix}$, $T^{2i} = \frac{1}{t_{2i}}\begin{bmatrix}1 & r_{2i}\\ r_{2i} & 1\end{bmatrix}$, $T^{i3} = \frac{1}{t_{i3}}\begin{bmatrix}1 & r_{i3}\\ r_{i3} & 1\end{bmatrix}$, and $T^{34} = \frac{1}{t_{34}}\begin{bmatrix}1 & r_{34}\\ r_{34} & 1\end{bmatrix}$.

The transfer matrix in the blister is $T^i = \begin{bmatrix}e^{i\alpha} & 0\\ 0 & e^{-i\alpha}\end{bmatrix}$, where $\alpha = \frac{2\pi}{\lambda} n_i d_i$.

The transfer matrix in graphene is $T^2 = \begin{bmatrix}e^{i\beta} & 0\\ 0 & e^{-i\beta}\end{bmatrix}$, where $\beta = \frac{2\pi}{\lambda} n_2 d_2$.

The transfer matrix in SiO_2 is $T^3 = \begin{bmatrix}e^{i\gamma} & 0\\ 0 & e^{-i\gamma}\end{bmatrix}$, where $\gamma = \frac{2\pi}{\lambda} n_3 d_3$.

The transfer matrix for the system is:

$$T^{14} = T^{12}T^{2}T^{2i}T^{i}T^{i3}T^{3}T^{34}$$

$$= \frac{1}{t_{12}}\begin{bmatrix} 1 & r_{12} \\ r_{12} & 1 \end{bmatrix}\begin{bmatrix} e^{i\beta} & 0 \\ 0 & e^{-i\beta} \end{bmatrix}\frac{1}{t_{2i}}\begin{bmatrix} 1 & r_{2i} \\ r_{2i} & 1 \end{bmatrix}\begin{bmatrix} e^{i\alpha} & 0 \\ 0 & e^{-i\alpha} \end{bmatrix}\frac{1}{t_{i3}}\begin{bmatrix} 1 & r_{i3} \\ r_{i3} & 1 \end{bmatrix}\begin{bmatrix} e^{i\gamma} & 0 \\ 0 & e^{-i\gamma} \end{bmatrix}\frac{1}{t_{34}}\begin{bmatrix} 1 & r_{34} \\ r_{34} & 1 \end{bmatrix}$$

$$T_{11}^{14} = \frac{1}{t_{12}t_{2i}t_{i3}t_{34}}(e^{i(\alpha+\beta+\gamma)} + r_{12}r_{2i}e^{i(\alpha-\beta+\gamma)} + r_{2i}r_{i3}e^{i(-\alpha+\beta+\gamma)} + r_{12}r_{i3}e^{i(-\alpha-\beta+\gamma)} + r_{i3}r_{34}e^{i(\alpha+\beta-\gamma)} + r_{2i}r_{34}e^{i(-\alpha+\beta-\gamma)} + r_{12}r_{34}e^{i(-\alpha-\beta-\gamma)} + r_{12}r_{2i}r_{i3}r_{34}e^{i(\alpha-\beta-\gamma)})$$

$$T_{21}^{14} = \frac{1}{t_{12}t_{2i}t_{i3}t_{34}}(r_{12}e^{i(\alpha+\beta+\gamma)} + r_{2i}e^{i(\alpha-\beta+\gamma)} + r_{i3}e^{i(-\alpha-\beta+\gamma)} + r_{34}e^{i(-\alpha-\beta-\gamma)} + r_{12}r_{2i}r_{i3}e^{i(-\alpha+\beta+\gamma)} + r_{12}r_{2i}r_{34}e^{i(-\alpha+\beta-\gamma)} + r_{12}r_{i3}r_{34}e^{i(\alpha+\beta-\gamma)} + r_{2i}r_{i3}r_{34}e^{i(\alpha-\beta-\gamma)})$$

The reflection coefficient is:

$$r = \frac{T_{21}^{14}}{T_{11}^{14}} = \frac{r_{12}e^{i(\alpha+\beta+\gamma)} + r_{2i}e^{i(\alpha-\beta+\gamma)} + r_{i3}e^{i(-\alpha-\beta+\gamma)} + r_{34}e^{i(-\alpha-\beta-\gamma)} + r_{12}r_{2i}r_{i3}e^{i(-\alpha+\beta+\gamma)} + r_{12}r_{2i}r_{34}e^{i(-\alpha+\beta-\gamma)} + r_{12}r_{i3}r_{34}e^{i(\alpha+\beta-\gamma)} + r_{2i}r_{i3}r_{34}e^{i(\alpha-\beta-\gamma)}}{e^{i(\alpha+\beta+\gamma)} + r_{12}r_{2i}e^{i(\alpha-\beta+\gamma)} + r_{2i}r_{i3}e^{i(-\alpha+\beta+\gamma)} + r_{12}r_{i3}e^{i(-\alpha-\beta+\gamma)} + r_{i3}r_{34}e^{i(\alpha+\beta-\gamma)} + r_{2i}r_{34}e^{i(-\alpha+\beta-\gamma)} + r_{12}r_{34}e^{i(-\alpha-\beta-\gamma)} + r_{12}r_{2i}r_{i3}r_{34}e^{i(\alpha-\beta-\gamma)}}$$

Intensity of reflected light, which is recorded experimentally in reflected light microscopy images, is thus:

$$I = |r|^2 I_I$$

$$= \left|\frac{r_{12}e^{i(\alpha+\beta+\gamma)} + r_{2i}e^{i(\alpha-\beta+\gamma)} + r_{i3}e^{i(-\alpha-\beta+\gamma)} + r_{34}e^{i(-\alpha-\beta-\gamma)} + r_{12}r_{2i}r_{i3}e^{i(-\alpha+\beta+\gamma)} + r_{12}r_{2i}r_{34}e^{i(-\alpha+\beta-\gamma)} + r_{12}r_{i3}r_{34}e^{i(\alpha+\beta-\gamma)} + r_{2i}r_{i3}r_{34}e^{i(\alpha-\beta-\gamma)}}{e^{i(\alpha+\beta+\gamma)} + r_{12}r_{2i}e^{i(\alpha-\beta+\gamma)} + r_{2i}r_{i3}e^{i(-\alpha+\beta+\gamma)} + r_{12}r_{i3}e^{i(-\alpha-\beta+\gamma)} + r_{i3}r_{34}e^{i(\alpha+\beta-\gamma)} + r_{2i}r_{34}e^{i(-\alpha+\beta-\gamma)} + r_{12}r_{34}e^{i(-\alpha-\beta-\gamma)} + r_{12}r_{2i}r_{i3}r_{34}e^{i(\alpha-\beta-\gamma)}}\right|^2 I_I$$

It can be shown that intensity without the blister ($d_i = 0$; water-graphene-substrate geometry) is:

$$I = \left|\frac{r_{12}e^{i(\beta+\gamma)} + r_{23}e^{i(\gamma-\beta)} + r_{34}e^{-i(\beta+\gamma)} + r_{12}r_{23}r_{34}e^{i(\beta-\gamma)}}{e^{i(\beta+\gamma)} + r_{12}r_{23}e^{i(\gamma-\beta)} + r_{23}r_{34}e^{i(\beta-\gamma)} + r_{12}r_{34}e^{-i(\beta+\gamma)}}\right|^2 I_I$$

It can be further shown that intensity without the blister and graphene ($d_i = 0$, $d_2 = 0$; water-substrate interface) is:

$$I_0 = \left|\frac{r_{13}e^{i\gamma} + r_{34}e^{-i\gamma}}{e^{i\gamma} + r_{13}r_{34}e^{-i\gamma}}\right|^2 I_I$$

For comparison with experiments, for IRM, the experimental signal I was first normalized by the signal measured at a direct substrate-solution interface (*e.g.*, locally exposed glass surface in the sample, as marked by "0" in Figure 20d), I_0. The resultant I/I_0 values were presented as images and compared with the theoretically predicted values (Figure 20b) to obtain the local blister height d_i and generate height maps. For reflected light microscopy, the experimental signal I, obtained at three fixed wavelengths of 610, 532, and 450 nm, was each separately normalized by the signal measured at a direct water-substrate interface, I_0. The resultant I/I_0 values were presented as images. For each pixel, the I/I_0 values were compared with the theoretical values at the same three

wavelengths for different local blister heights d_i (Figure 29d). Local d_i values were then assigned by minimizing the sum of the differences between the experimental and theoretical values at the three wavelengths.

Simulation of blister IRM and reflected light microscopy images. Half-ellipsoids of varying heights were first simulated on grids 10 times finer than the actual pixel size. For simulating IRM images, the half-ellipsoids were converted from heights to IRM contrasts using the theoretically predicted IRM signal discussed above. The resultant simulated images were then spatially convolved with a 2D Gaussian function with an FWHM (full width at half maximum) of 300 nm to simulate the diffraction-limited optical resolution. The images were then down-sampled to the actual pixel size to generate the final simulated IRM images. For graphene on Si/SiO_2, reflected light microscopy images were similarly simulated at the three experimental wavelengths.

Part II: Facile chemical modifications of graphene under ambient conditions supported by optical characterization

In this section, we move to discuss facile chemical modifications of graphene under ambient conditions. Besides IRM, other optical characterizations techniques including transmission microscopy, fluorescence microscopy, and Raman spectroscopy are utilized here to help establish the successful modifications of graphene through our facile approaches. In chapter 4, we report direct azidation and subsequent click chemistry of the graphene basal plane through the electrochemical oxidation of an aqueous sodium azide solution at the graphene surface. As azide is chemically analogous to halogens, we next apply a comparable strategy in chapter 5 to directly chlorinate graphene from an aqueous sodium chloride solution through electrochemistry. Beyond that, we have also explored the possibility to remove the need to wire up graphene for electrochemistry while still enabling facile chemical modifications of graphene under ambient conditions. In chapter 6, we report a photocatalytic approach for the facile azidation and chemical patterning of graphene.

Chapter 4: Azidated graphene: direct azidation from monolayer, click chemistry, and bulk production from graphite

The work in this chapter was conducted in collaboration with Wan Li and Ke Xu. It is reproduced in part here from ref[101] with permission from all co-authors.

4.1 Introduction

Chemical modification and functionalization greatly expand the application of graphene[20,22,24,54,103-105]. However, the graphene basal plane is notoriously inert; limited approaches exist for its covalent chemistry, and it is challenging to achieve controllable reactions. Radical addition is a major route to graphene basal-plane functionalization.[20,22,24,54] The high reactivity of free radicals is key to initiating reactions with the basal plane under relatively mild conditions, but often gives rise to extensive side reactions and thus not-well-defined chemical structures.[24] For instance, the popular reaction of graphene and graphite with aryl radicals generated from diazonium salts[11,56] can be achieved under ambient conditions, but often results in heterogeneous aryl oligomers.[7,53,56,106] Moreover, for each desired surface function, the

corresponding radical-generating reagent often needs to be designed anew, thus limiting application.

In this chapter, we report facile, direct azidation of the graphene basal plane, click chemistry of the product for different surface functions, as well as bulk production of azidated graphene flakes from graphite. Although previous work has examined the azidation of the chemically much more active[18,25] graphitic oxide to a few percent of total weight,[107-109] limited success has been achieved in converting such heterogeneous systems to graphitic azide.[109] It is thus of both fundamental and application interests to examine if stable, well-defined azidated graphene could be obtained, as well as if such a system would be electrically conductive and/or suitable for click chemistry.

4.2 Results and discussion

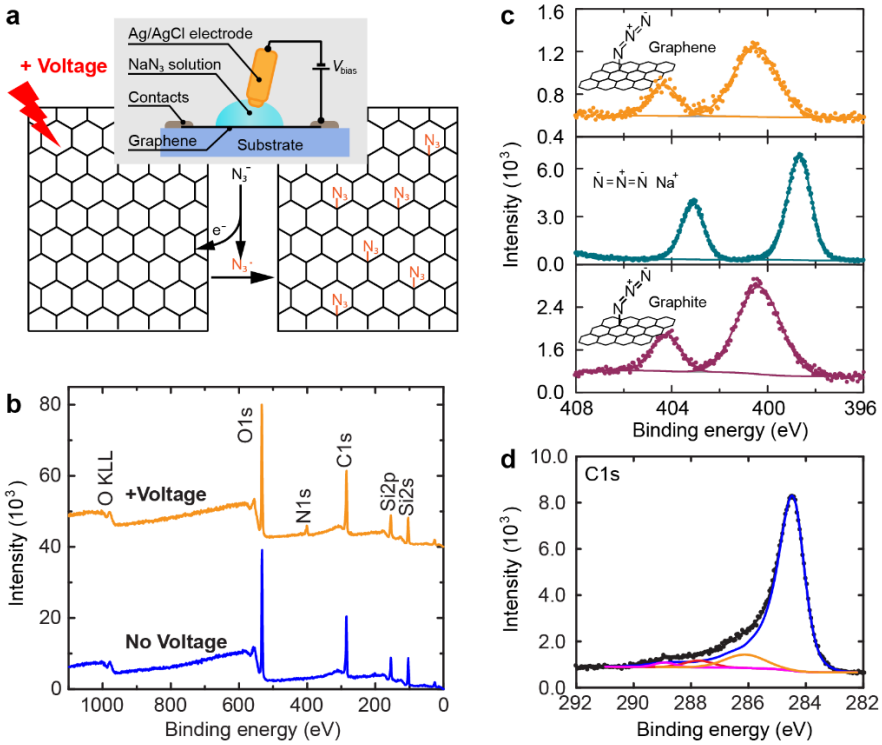

Figure 38. Direct azidation of monolayer graphene. (a) Schematic of the azidation process. In a pH-neutral aqueous solution, the electrochemical oxidation of N_3^- at the graphene surface generates azidyl radicals ($N_3\cdot$), which react *in situ* with the basal plane. (b) Survey-mode XPS of monolayer graphene on a SiO_2/Si substrate after electrochemical reaction in a 200 mM NaN_3 solution at 1.3 V (vs. Ag/AgCl) for 15 min (top), vs. a control sample that was immersed in a 400 mM NaN_3 solution for 20 min but without the application of voltages (bottom). (c) High-resolution XPS for the nitrogen 1s region of the azidated graphene (top) vs. that of the solid surface of NaN_3 salt (middle), and a freshly cleaved graphite surface after electrochemical reaction in a 400 mM NaN_3 solution at 1.3 V (vs. Ag/AgCl) for 10 min (bottom). (d) High-resolution XPS for the carbon 1s region of the azidated graphene (black dots and curve), in comparison to that of the starting monolayer graphene (blue curve). Orange, red, and magenta curves fit to the difference between the two curves, which are attributable to C-N/C-O, C=O, and O=C-OH bonds, respectively.

We start by developing a strategy to electrochemically generate azidyl radicals[110,111] at the graphene surface *in situ* through the oxidation of the simple salt sodium azide (NaN_3) in an aqueous solution (Figure 38a). This approach leads to efficient, tunable azidation of the graphene surface, which then allows for the expansion of surface functionality to broad possibilities through click chemistry[112-114] and bioconjugation. Remarkably, we find that graphene maintains high electrical conductivity and carrier mobility after azidation, cycloaddition, and bioconjugation, thus pointing to the potential of all these new graphene derivatives for electronics and biosensing applications. To conclude, we demonstrate the possibility to combine electrochemical azidation with electrochemical exfoliation for the bulk production of azidated graphene flakes from graphite.

CVD-grown monolayer graphene was deposited as ~2×10 mm strips onto thermal oxide-coated silicon chips (SiO_2/Si) or glass substrates, and electrically contacted at both ends. Interference reflection microscopy (IRM)[4] confirmed that the deposited graphene was predominately monolayer with sporadic nanoscale bilayer islands (Figure 39). A ~150 µL drop of 200 mM NaN_3 in a 0.1 M pH=7 phosphate buffer (PB7) was placed at the center of the graphene strip, thus creating both immersed and non-immersed areas in the same sample as defined by the drop boundary. An Ag/AgCl electrode served as the counter/reference electrode by contacting the top of the electrolyte drop (Figure 38a inset).

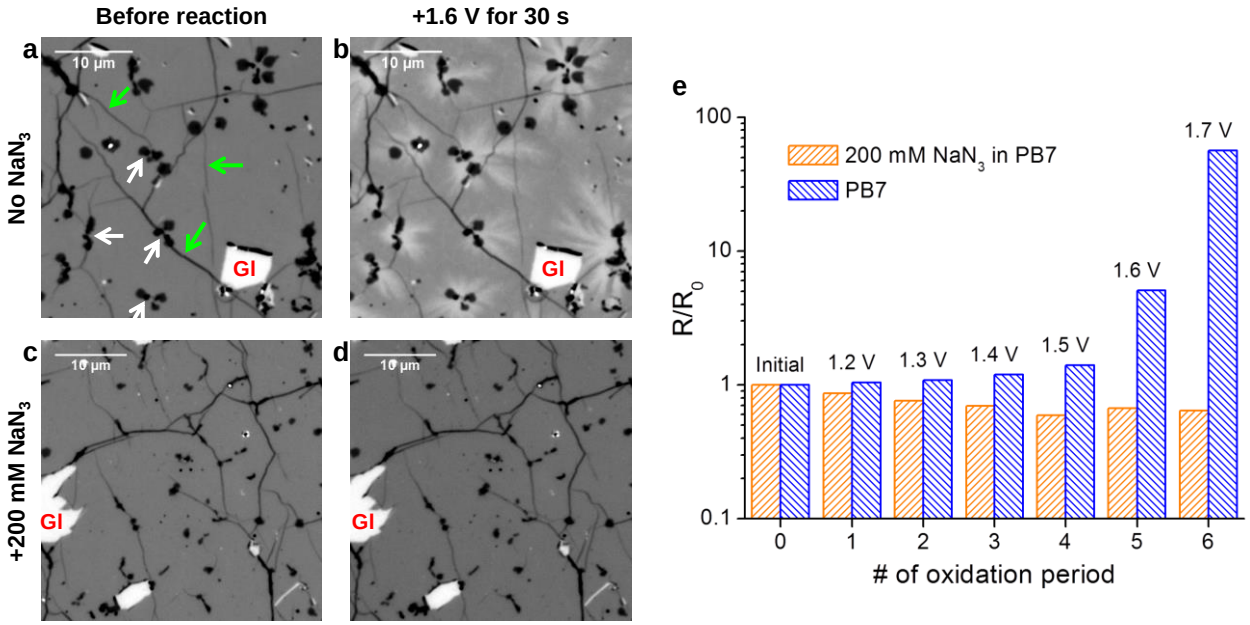

Figure 39. *In situ* IRM and electrical measurements indicate that adding NaN_3 into the electrolyte suppresses the electrochemical oxidation of graphene while enabling azidation. (a) IRM image of a CVD graphene sample on a glass substrate in blank PB7, showing that the starting graphene was predominately monolayer with sporadic nanoscale bilayer islands (white arrows) and wrinkles (green arrows) [4]. "Gl" marks exposed glass surface due to a tear in graphene. (b) IRM image of the same area after the application of a +1.6 V (vs. Ag/AgCl) oxidative voltage for 30 s. Notable oxidation occurred (brightening up of IRM signal, especially for areas surrounding the bilayer islands), as discussed in detail previously [15]. (c,d) IRM images of another sample before (c) and after (d) the same applied voltage, but in PB7 containing 200 mM NaN_3. Oxidation of graphene appeared to be fully suppressed. We further note that we found that the azidation of graphene gave

no notable changes to the IRM signal, consistent with the limited changes in electrical conductivity in the process. (e) Changes in graphene resistance over initial values after the application of a series of oxidative voltages (vs. Ag/AgCl) of 45 s duration in 0.1 V increasing steps, for CVD graphene in PB7 with (orange) and without (blue) 200 mM of NaN_3. The PB7-only sample showed progressive increases in resistance for voltages >+1.4 V due to oxidation. In contrast, the sample in the NaN_3 solution showed a trend of decreasing resistance right from the first step of +1.2 V due to the azidation of graphene. Scale bars: 10 μm (a-d).

Remarkably, the application of a voltage of +1.3 V across the graphene and the Ag/AgCl electrodes led to effective azidation of graphene (Figure 38a). Survey-mode X-ray photoelectron spectroscopy (XPS) of the sample on the SiO_2/Si substrate, after water-rinsed and air-dried, showed the appearance of a nitrogen 1s peak (Figure 38b, top) when compared to a control sample that was immersed in a NaN_3 solution without applying voltages (Figure 38b, bottom). Analysis of the C, N, O, and Si peak areas gave atomic percentages of 45.9%, 4.7%, 33.0%, and 16.4% for the voltage-applied sample, and 46.2%, 0%, 36.1%, 17.6% for the control sample, respectively. The ~2:1 ratios of O:Si in both samples indicate that the O signal was mostly from the SiO_2 substrate. Indeed, we have recently shown that the electrochemical oxidation of graphene requires >+1.4 V vs. Ag/AgCl,[15] and we also found that NaN_3 actually further suppresses graphene oxidation (below).

Meanwhile, the emerged N peak at ~11% N/C ratio suggests voltage-driven azidation of graphene. High-resolution XPS of the nitrogen 1s region of the azidated sample (Figure 38c, top) showed two peaks at 400.6 and 404.4 eV at a ~2:1 ratio, consistent with those typically found in organic azides[115-117] and markedly different from that measured for the NaN_3 salt surface at 398.7 and 403.1 eV (Figure 38c, middle).[118] Meanwhile, high-resolution XPS of the carbon 1s region showed an increase at ~286.1 eV (orange fitted curve in Figure 38d), consistent with that of C-N bonds[18,119,120] albeit complicated by C-O bonds at similar energies. Together, these results suggest successful covalent azidation of graphene through our electrochemical process.

We further found that the above electrochemical approach also efficiently azidated freshly cleaved graphite surfaces (Figure 38c, bottom). This result provides further evidence that the azidyl radicals electrochemically generated at the electrode surface[110,111] are effective in reacting with the basal plane, in line with previously reported high reactivity of electrochemically generated aryl and arylmethyl radicals and light-generated chlorine radicals towards the basal planes of graphite and multilayer graphene.[56,121-124]

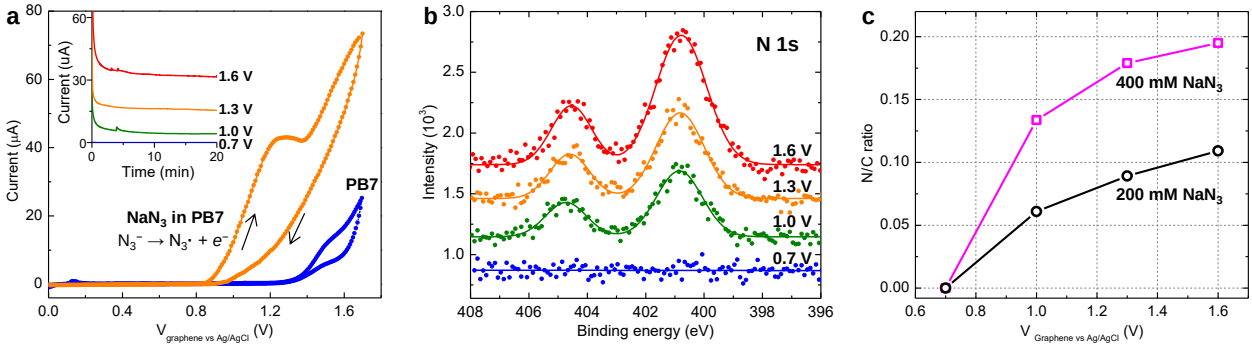

Figure 40. Azidation results under different applied voltages and NaN_3 concentrations. (a) Measured electrochemical current vs. a scanned voltage (40 mV/s) across monolayer graphene and a Ag/AgCl electrode, in 200 mM NaN_3 in PB7 (orange curve) vs. in blank PB7 (blue curve). Inset: time-dependent electrochemical current in 200 mM NaN_3 in PB7, for four different graphene devices at fixed voltages of 0.7, 1.0, 1.3, and 1.6 V (vs. Ag/AgCl), respectively. (b) XPS of the nitrogen 1s region for the above four samples. (c) The measured nitrogen-to-carbon (N/C) ratio as a function of the applied voltage for 20-min reactions in 200 mM (black curve) and 400 mM (magenta curve) NaN_3 solutions.

To gain control of the azidation process, as well as insights into the reaction mechanism, we next varied the applied voltage. Scanning up the voltage at 40 mV/s in 200 mM NaN_3 in PB7, the detected electrochemical current rose rapidly at >0.9 V (vs. Ag/AgCl) and peaked at ~1.25 V (Figure 40a, orange curve), consistent with the electrochemical oxidation of the azidyl/azide couple [$E(N_3\cdot/N_3^-)$ ~1.35 V vs. normal hydrogen electrode[111]]. Mild bubble generation was noted for >~1.0 V, attributable to the self-combination of excessive azidyl radicals ($2\ N_3\cdot \rightarrow 3N_2$). Further increasing the voltage beyond ~1.4 V led to another rise in current; this rise coincided with the onset of current in blank PB7 (Figure 40a, blue curve) and is ascribed to the electrolysis of water.[15] Reversed scan yielded no noticeable reduction peaks, consistent with the high reactivity of the generated azidyl radicals.[111]

Based on these results, we examined graphene azidation efficiency at different fixed voltages. Whereas no appreciable azidation occurred at 0.7 V vs. Ag/AgCl (Figure 40b), under which condition the electrochemical current was negligible (Figure 40a inset), substantial azidation was found at 1.0 V (Figure 40b), for which case the electrochemical current was significant (Figure 40a inset). Stronger azidation was achieved at 1.3 V, and a further slight increase was found for 1.6 V (Figure 40bc). We have recently identified 1.4 V (vs. Ag/AgCl) as the onset voltage for the electrochemical oxidation of graphene.[15] Interestingly, IRM showed that whereas 1.6 V (vs. Ag/AgCl) quickly oxidized graphene in the blank PB7, the oxidation was fully suppressed with 200 mM NaN_3 added (Figure 39). This result can be understood as that the hydroxyl radical ($HO\cdot$), the major oxidative species in water electrolysis that drives graphene oxidation,[15,125] is readily consumed by N_3^- to produce OH^- and $N_3\cdot$.[126]

The azidation degree also depended on the NaN_3 concentration (Figure 40c). For 1.6 V vs. Ag/AgCl, final N/C ratios of 11% and 19.5% were obtained when the electrolyte contained 200 and 400 mM NaN_3, respectively. With three nitrogen atoms in each azido group, the latter result indicates ~6.5% of all carbon atoms were azidated. Varying the reaction time (Figure 41) showed that effective azidation occurred within 5 min, and improved slightly further with 10-20 min of reaction. Together, these results demonstrate that the azidation degree of graphene is tunable through both the applied voltage and the NaN_3 concentration, while further confirming the reaction mechanism of *in situ* generation of azidyl radicals (Figure 38a).

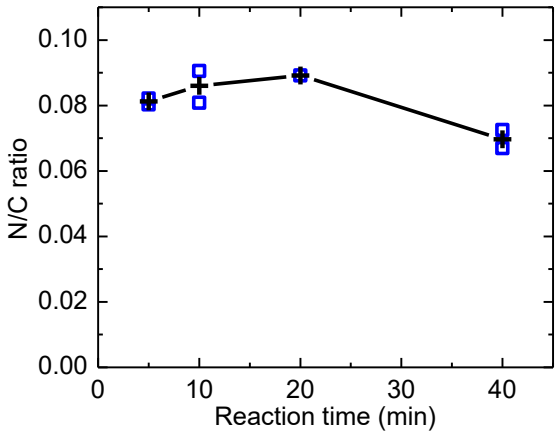

Figure 41. XPS-measured N/C ratio as a function of reaction time for reactions at 1.3 V (vs. Ag/AgCl) in a 200 mM NaN_3 solution. Crosses: averages of two runs (blue squares).

The azidated graphene surface readily enabled copper (I)-catalyzed alkyne-azide cycloaddition (CuAAC) click chemistry.[112] For CuAAC of the azidated graphene with alkyne-PEG_5-acid (Figure 42a), XPS of the nitrogen 1s region (Figure 42b) showed a small peak at ~404.2 eV (cyan) attributed to the unreacted azido groups (~404.4 eV above in Figure 38c), as well as a major peak at 400.2 eV (magenta) that is shifted towards a slightly lower binding energy when compared to the azido group (~400.6 eV in Figure 38c), together with the emergence of a shoulder peak at 401.6 eV (blue). These results are in good agreement with the generation of triazole groups through CuAAC.[116,127]

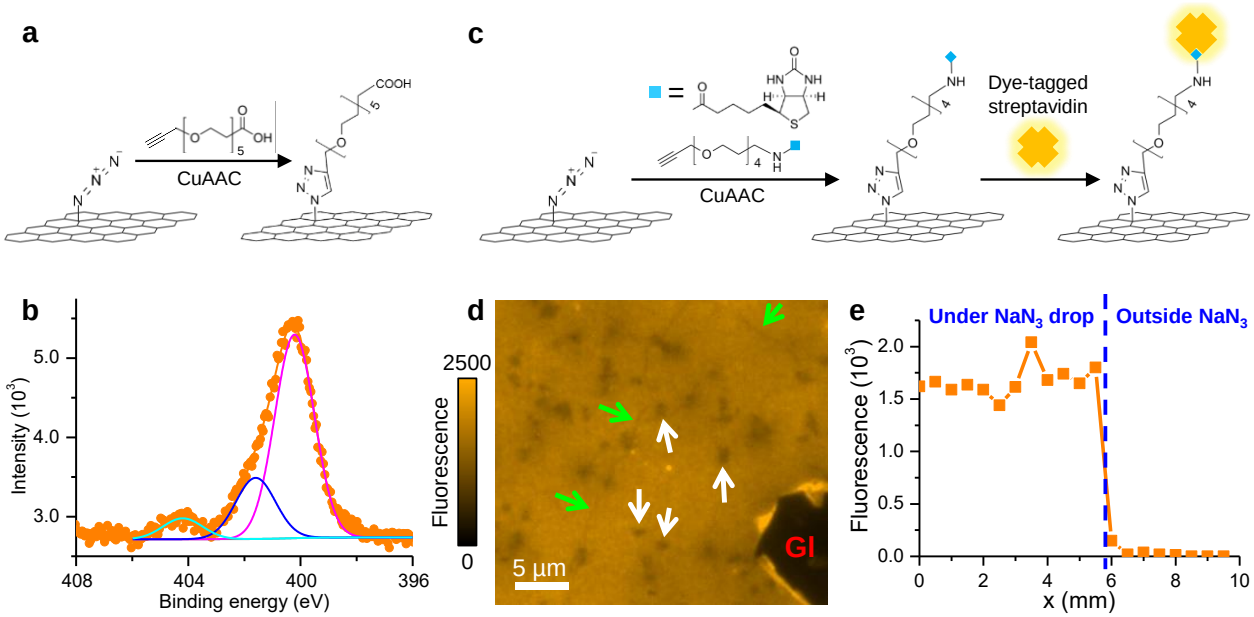

Figure 42. CuAAC click chemistry of azidated graphene and subsequent biotin-streptavidin bioconjugation. (a) Schematic: CuAAC of azidated graphene with alkyne-PEG_5-acid. (b) XPS of the nitrogen 1s region for the resultant product (orange) on a SiO_2/Si substrate, fit to magenta, blue, and cyan peaks at 400.2, 401.6, and 404.2 eV, respectively. (c) Schematic: CuAAC of azidated graphene with alkyne-PEG_4-biotin, and subsequent conjugation with streptavidin tagged by the fluorescent dye Alexa Fluor 555 (AF555). (d) Fluorescence microscopy image of the labeled

AF555 for the resultant functionalized graphene on a glass substrate. White and green arrows point to reduced local fluorescence at bilayer islands and wrinkles in graphene, respectively. "Gl": exposed glass surface with no graphene coverage. (e) Fluorescence intensity for different regions of another sample (Figure 44), in 0.5 mm translational steps along the *x*-direction. Blue dashed line marks the boundary position of the initial NaN_3 drop.

To evaluate the spatial homogeneity of the functionalization result, we performed CuAAC of the azidated graphene with a fluorescent dye-tagged alkyne (Figure 43), as well as with alkyne-PEG_4-biotin for subsequent bioconjugation of dye-tagged streptavidin (Figure 42c). Fluorescence microscopy showed spatially uniform dye labeling for both samples (Figure 42de and Figure 43), with reduced local intensities noted at bilayer islands (white arrows in Figure 42d) and wrinkles (green arrows), consistent with fluorescence quenching by graphene.[128] Meanwhile, as the NaN_3 solution droplet in the initial azidation process only partially covered the graphene strip, the non-azidated parts of the same graphene sample showed minimal fluorescence (Figures 42e, 43 and 44) even though the CuAAC and streptavidin reactants covered the entire sample, thus signifying specific labeling through click chemistry.

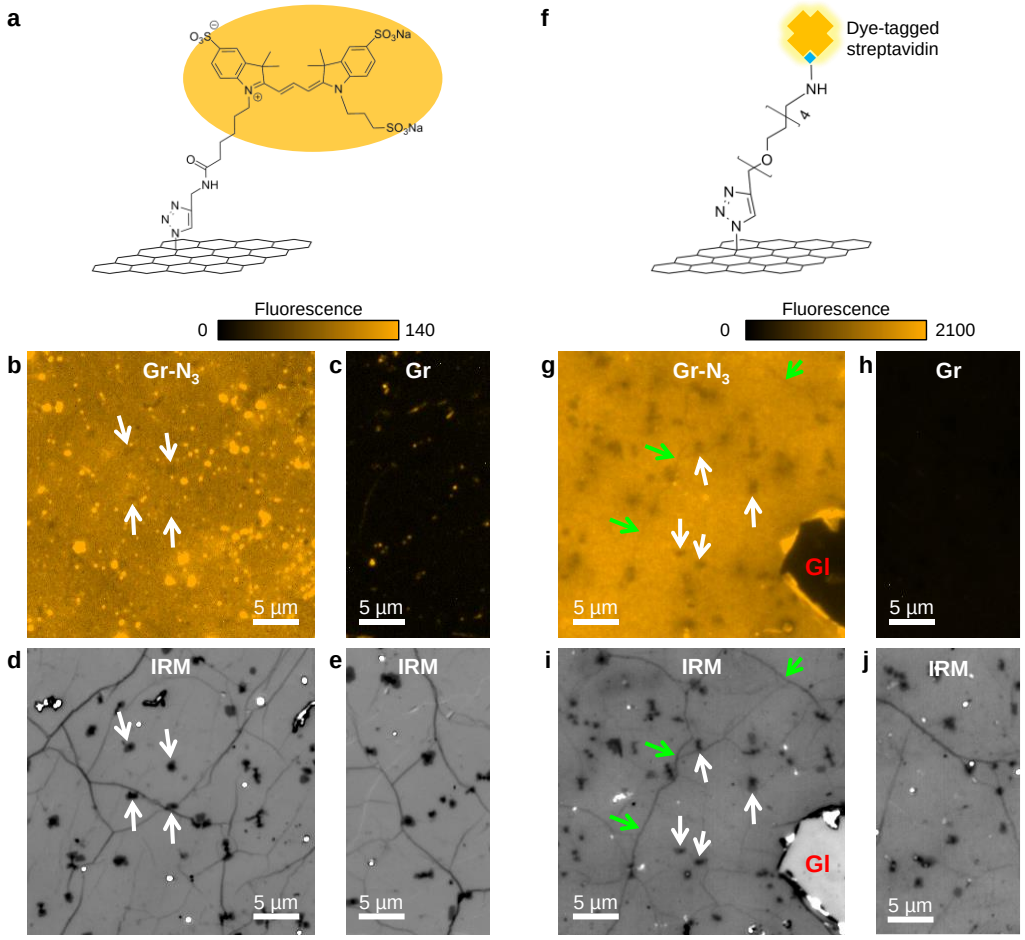

Figure 43. Fluorescence microscopy and IRM characterizations of the azidated graphene on glass substrates, after CuAAC with alkyne-Cy3 and after CuAAC with alkyne-PEG$_4$-biotin and subsequent conjugation with streptavidin-Alexa Fluor 555 (AF555). (a) Schematic of the alkyne-Cy3-clicked azidated graphene. (b-c) Fluorescence microscopy images of the labeled Cy3 of the final product, for areas inside (b) and outside (c) the initial NaN_3 drop during electrochemical azidation. The CuAAC reactant covered both areas. (d-e) Corresponding IRM images, showing that graphene is predominately monolayer for both areas [4]. White arrows in (b,d) point to nanoscale bilayer islands. (f) Schematic of the final product of the CuAAC of azidated graphene with alkyne-PEG$_4$-biotin and subsequent conjugation with streptavidin-AF555. (g-h) Fluorescence microscopy images of the labeled AF555 for the resultant functionalized graphene, for areas inside (g) and outside (h) the initial NaN_3 drop. (g) corresponds to the same image as Figure 3d. (i-j) IRM images of the same areas as (g,h), indicating monolayer graphene. White and green arrows in (g,i) point to bilayer islands and wrinkles in graphene, respectively. "Gl" in (g,i): exposed glass surface with no graphene coverage. Note the different intensity scales for (g,h) versus (b,c): dye molecules on streptavidin (~5 nm in size) are farther away from the graphene surface and so are less quenched in fluorescence emission [45,128].

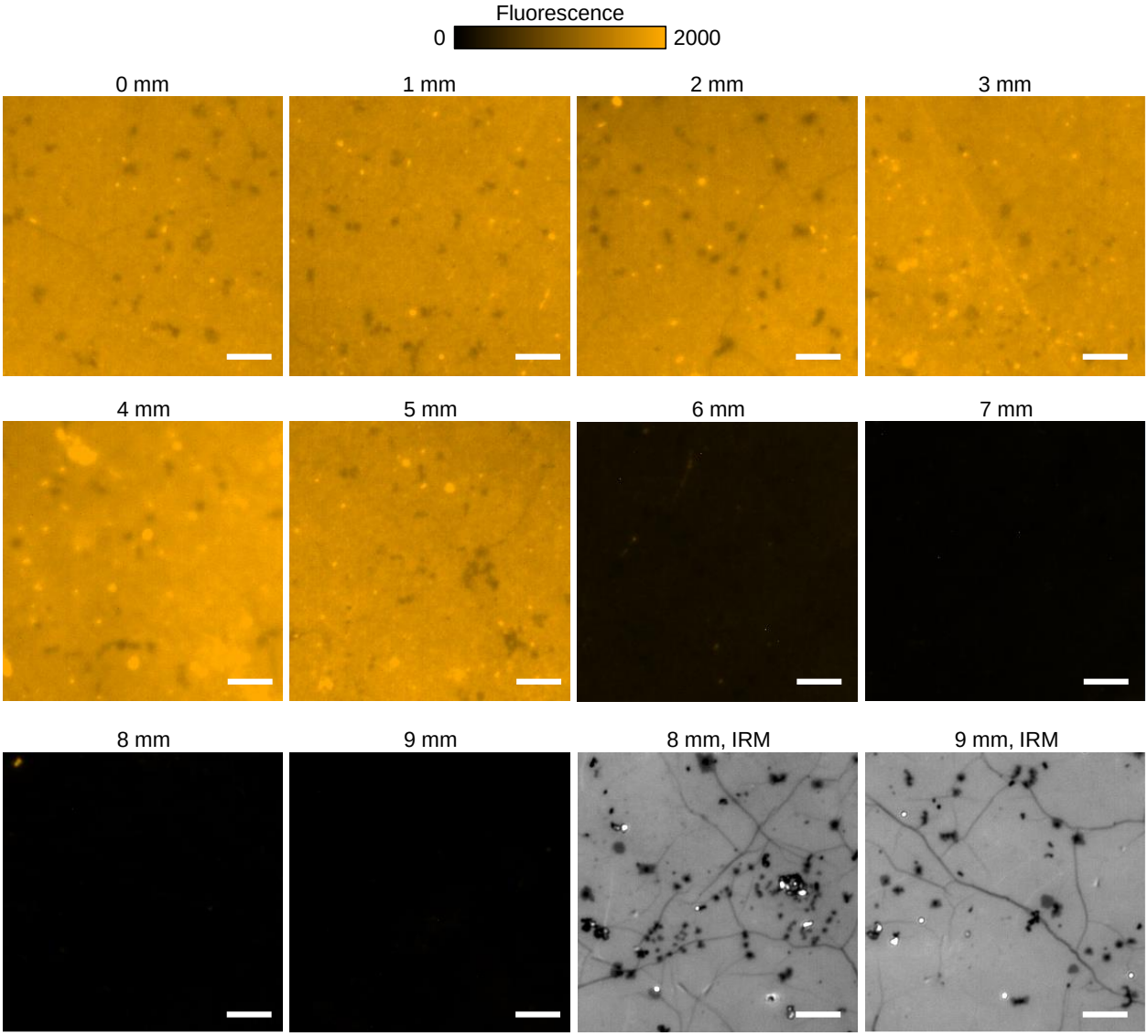

Figure 44. Fluorescence microscopy images of the labeled AF555, for an azidated graphene sample on a glass substrate after CuAAC with alkyne-PEG4-biotin and subsequent conjugation with streptavidin-AF555, corresponding to the x = 0,1,2,3,4,5,6,7,8,9 mm positions shown in Figure 42e, respectively. The last two panels show the IRM images at x = 8 and 9 mm, to confirm that monolayer graphene is present, with typical features as nanoscale bilayer islands and wrinkles [4], but not functionalized. Scale bars: 5 μm.

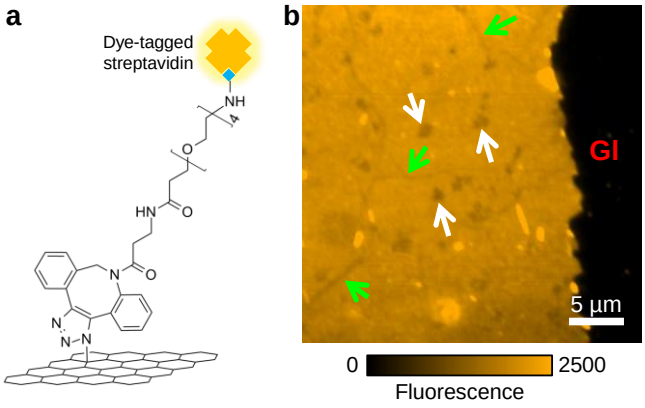

Figure 45. Copper-free cycloaddition of azidated graphene and subsequent biotin-streptavidin conjugation. (a) Schematic of the final product. (b) Fluorescence microscopy of the labeled AF555 for the resultant functionalized graphene on a glass substrate. "Gl" marks the glass substrate, where the functionalized graphene was locally peeled away.

We next examined if the azidated graphene could permit copper-free cycloaddition,[113,114] which by eliminating the need for potentially toxic Cu ions, is advantageous for biological applications. We thus showed the successful copper-free cycloaddition of azadibenzocyclooctyne (ADIBO)-PEG_4-biotin with the azidated graphene, as well as subsequent streptavidin conjugation (Figure 45 and Figure 46).

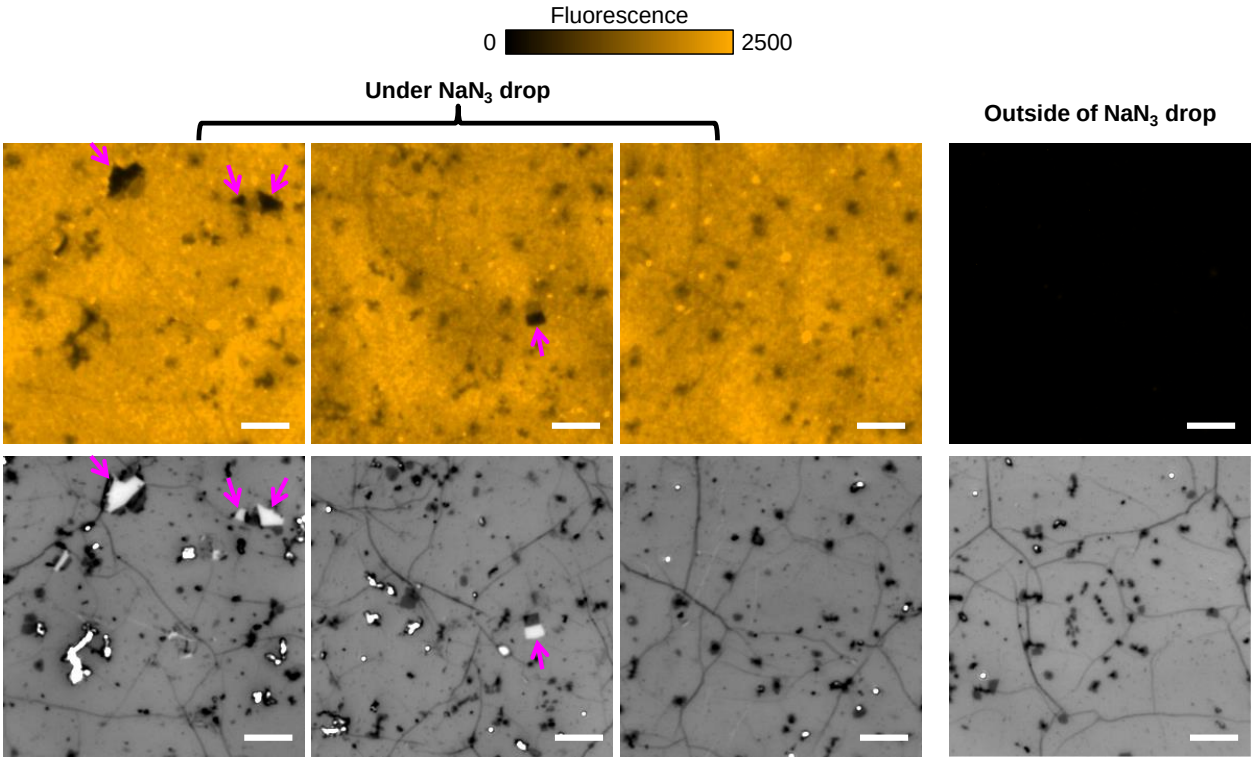

Figure 46. Additional fluorescence microscopy and IRM images for azidated graphene on a glass substrate after copper-free cycloaddition of azadibenzocyclooctyne (ADIBO)-PEG_4-biotin and subsequent conjugation with streptavidin-AF555. **Top row**: Fluorescence microscopy images of the labeled AF555, for areas inside (first three columns) and outside (last column) the initial NaN_3

drop during the electrochemical reaction. **Bottom row**: corresponding IRM images of the same areas as the top row, showing that graphene is predominately monolayer for all areas [4]. Magenta arrows point to tears/fold-overs in graphene. Scale bars: 5 µm.

We further followed the evolution of graphene electrical properties through the functionalization processes under a field-effect transistor scheme. Scanning the source-drain voltage (V_{sd}) between −20 to +20 mV yielded linear *I-V* curves (Figure 47a and Figure 48), from which we calculated sample conductance as varied electrochemical gating voltages (V_g) were applied across the Ag/AgCl electrode and graphene (Figure 47b; electrolyte: 70 mM pH = 7 phosphate buffer). Conductance of the starting sample was ~0.11 mS (Figure 47ab), consistent with the ~2×10 mm strip geometry, with electrochemical-gating results (Figure 47b) typical of monolayer graphene.[129]

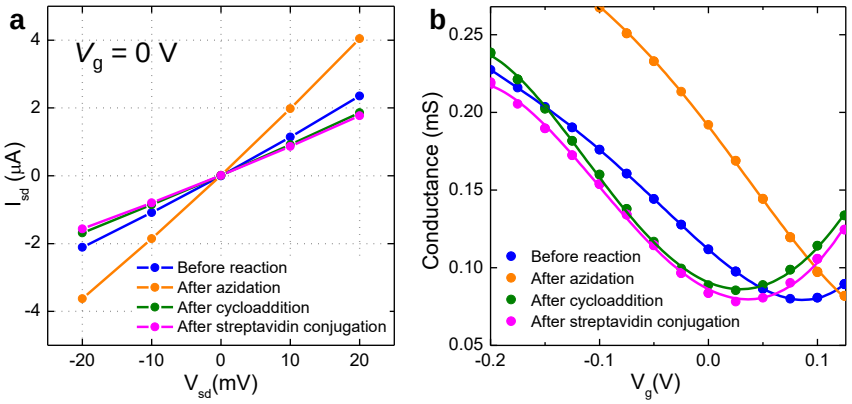

Figure 47. Electrical characterizations of azidated and clicked graphene. (a) *I-V* curves for monolayer graphene on a glass substrate at 0 V gate voltage, before reaction (blue), after azidation (orange), after copper-free cycloaddition of ADIBO-PEG$_4$-biotin (green), and after streptavidin conjugation (magenta). (b) Conductance obtained from linear fits to *I-V* curves, as a function of the electrochemical gating voltage applied to the Ag/AgCl electrode vs. graphene, for the four functionalization states. Electrolyte was a 70 mM pH = 7 phosphate buffer.

Remarkably, the graphene conductance increased notably after azidation (Figure 47a). Gate-dependent measurement showed a substantial positive voltage shift for the conductance-V_g transfer curve (Figure 47b), indicating enhanced *p*-doping, consistent with azido groups being electron-withdrawing.[130,131] A high conductance-V_g slope was also noted (Figure 47b), indicative of high carrier mobility. Similar *p*-doping behavior with high conductivity and mobility has been noted before for highly chlorinated monolayer graphene.[132-136] As a pseudohalogen, the azido group is characterized by Hammett substituent constants comparable to that of halogens,[130] and so it could affect graphene properties analogously. To this end, we found Raman spectroscopy of the azidated graphene (Figure 49) also behaved similarly as the highly chlorinated graphene, namely a significant decrease in the intensity ratio of the 2D peak over the G peak but little increase in the D peak signal.[133,135,136] It is thus possible that the azido group similarly *p*-doped graphene without inducing high levels of defects in the graphene lattice,[133-136] hence the measured high electrical conductivity. Cycloaddition of ADIBO-PEG$_4$-biotin led to substantial *n*-doping while keeping the large conductance-V_g slope (Figure 47b). Subsequent streptavidin conjugation did not cause significant further changes (Figure 47b). Together, our observation that graphene maintained high conductance and mobility throughout all the above functionalization states points to the potential of these new graphene derivatives in electronics and biosensing applications.

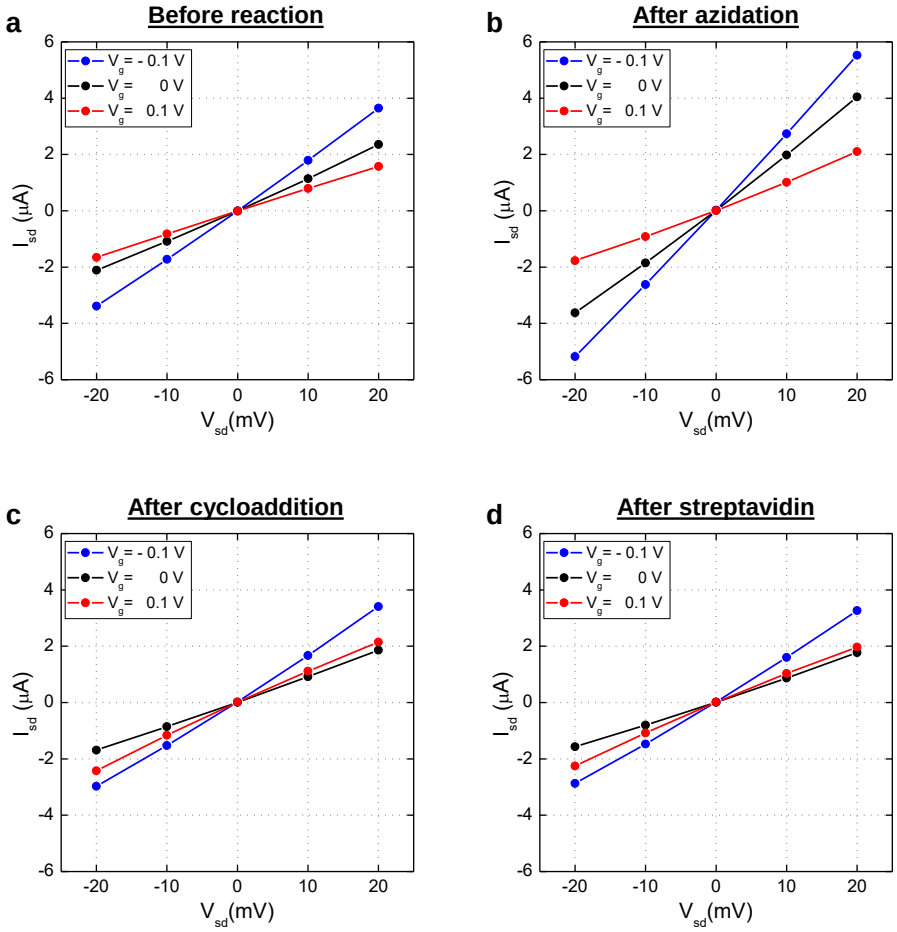

Figure 48. Measured *I-V* curves of the device in Figure 47, at representative electrochemical gating voltages of −0.1 (blue), 0 (black), and 0.1 (red) V, for before reaction (**a**), after azidation (**b**), after cycloaddition of ADIBO-PEG4-biotin (**c**), and after streptavidin conjugation (**d**).

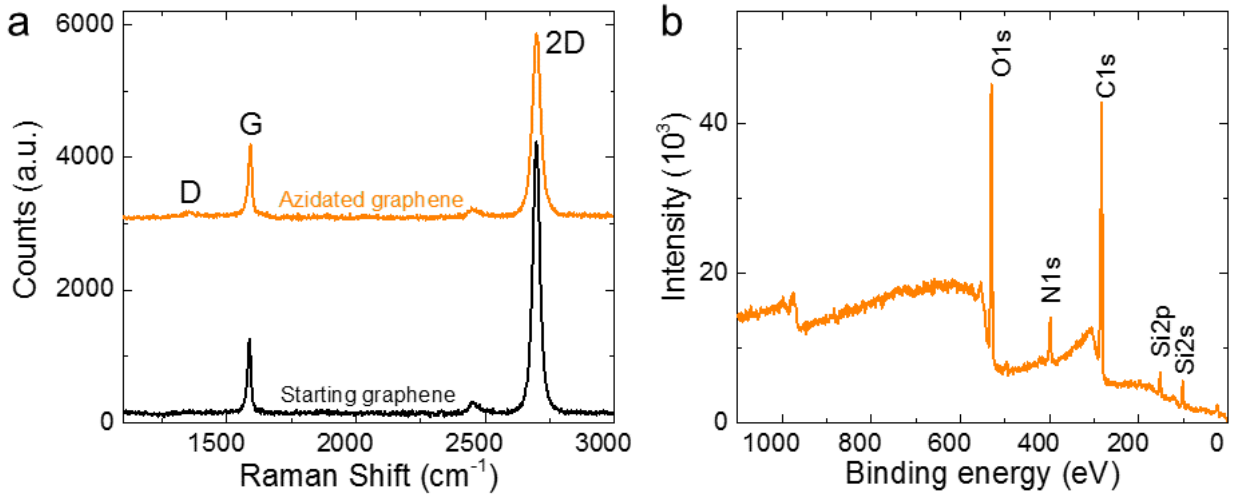

Figure 49. (a) Raman spectroscopy of the azidated graphene on a glass substrate [orange curve, azidated in 400 mM NaN_3 (PB7) at 1.3 V for 15 min] vs. the starting CVD graphene (black curve). The azidated graphene showed a significant decrease in the intensity ratio of the 2D peak over the G peak but little increase in the D peak signal. Both behaviors are highly similar to that previous found for the highly chlorinated graphene [133,135,136], in line with the pseudohalogen properties of the azido group, which is characterized by Hammett substituent constants comparable to that of halogens [130]. (b) XPS spectrum of the same azidated graphene sample in (a), confirming the successful functionalization to an N/C atomic ratio of 17.6%.

By integrating our above electrochemical azidation scheme with electrochemical exfoliation, we next demonstrated one-step bulk production of azidated graphene from graphite. Recent years have witnessed the rise of electrochemical exfoliation as a powerful pathway to graphene bulk production.[103,105,137] In particular, the anodic exfoliation of graphite in aqueous sulfate solutions has achieved high efficiency.[138]

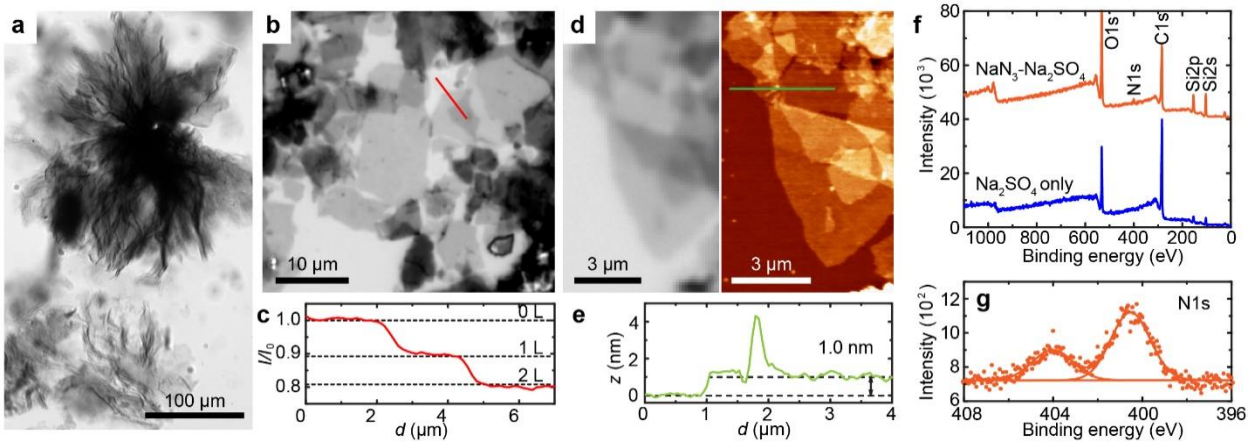

Figure 50. Bulk production of azidated graphene flakes through the electrochemical exfoliation of graphite in a NaN_3-Na_2SO_4 solution. (a) Transmission optical micrograph of flower-like graphitic particles generated through the electrochemical exfoliation of graphite in an aqueous solution of 200 mM NaN_3 and 400 mM Na_2SO_4. (b) Reflected light micrograph for the resultant flakes on a SiO_2/Si substrate. (c) Intensity profile along the red line in (b), normalized to the intensity at the bare substrate. Dot lines: expected intensities of monolayer and bilayer graphene,

as calibrated with CVD graphene samples. (d) Reflected light microscopy (left) and AFM (right) images of another sample. (e) Height profile along the green line in (d). (f) Survey-mode XPS spectrum of the product on a SiO_2/Si substrate (top), vs. that produced through the electrochemical exfoliation of graphite in a Na_2SO_4-only solution (bottom). (g) High-resolution XPS spectrum of the N1s region for the sample exfoliated in the NaN_3-Na_2SO_4 solution.

We found natural graphite to be readily exfoliated in an aqueous solution of 200 mM NaN_3 and 400 mM Na_2SO_4, although the voltage required was notably higher than that in a Na_2SO_4-only solution (+7 vs. +5 V; Methods). Transmission optical microscopy showed the generation of ~200 μm-sized, flower-like particles of loose few-layer sheets (Figure 50a). The product was collected, washed, re-dispersed through a brief sonication, and then drop-casted onto SiO_2/Si substrates (Materials and methods). Reflected light microscopy showed monolayer flakes ~10 μm in size (Figure 50b and Figure 51), with image contrasts matching well to that calibrated with CVD graphene (Figure 50c). Accordingly, AFM showed heights of ~1.0 nm (Figure 50de), typical of monolayer graphene.

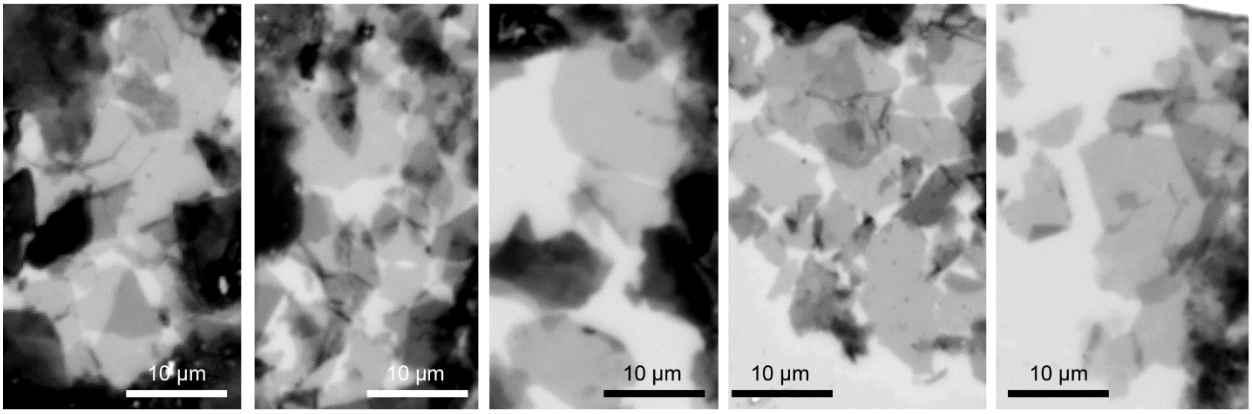

Figure 51. Additional reflective light microscopy images of azidated graphene flakes deposited on a SiO_2/Si substrate, obtained through the electrochemical exfoliation of graphite in the NaN_3-Na_2SO_4 solution, showing the abundant presence of monolayers.

Notably, when compared to samples exfoliated in the Na_2SO_4-only solution, XPS of samples exfoliated in the NaN_3-Na_2SO_4 solution showed the emergence of N1s signal (Figure 50f). High-resolution data showed two N1s peaks at 400.5 and 404.1 eV (Figure 50g), similar to our results above on CVD graphene (Figure 38c), thus indicating azidated graphene flakes. Quantitative analysis showed an N/C atomic ratio of 5%, and an O/C ratio of 20% after subtracting the O signal from the SiO_2 substrate. In comparison, the Na_2SO_4-only sample (Figure 50f, bottom) had no N signal and an O/C ratio of 12%. The higher O/C ratio of the azidated sample may be related to the above-noted higher required voltage for exfoliation, which points to competitions between the SO_4^{2-}-intercalation and N_3^--azidation processes, and hence the necessity to explore multiple parameters for future optimization. Nonetheless, with the achieved ~5% N/C ratio, clicking with a strongly negatively charged molecule already showed improved dispersion of the graphene flakes in water (Figure 52).

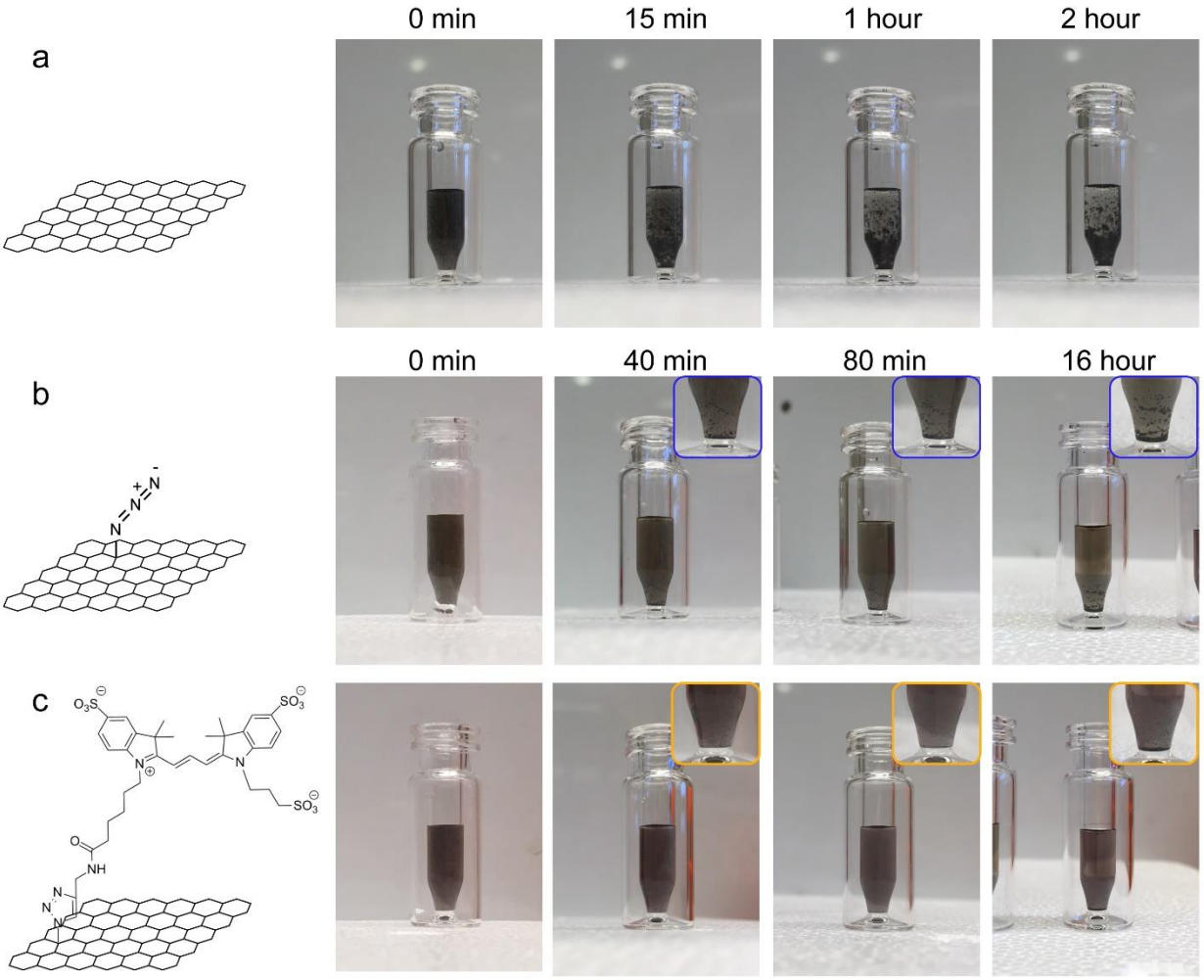

Figure 52. Dispersion of the functionalized graphene flakes in water. (a) Graphene flakes exfoliated in the Na_2SO_4-only solution, showing quick aggregation in ~15 min. (b) Azidated graphene flakes exfoliated in the NaN_3-Na_2SO_4 solution, showing slower aggregation at 40 min, 80 min and 16 hr. (c) Azidated graphene flakes after click chemistry with alkyne-Cy3, showing further improved dispersion at 80 min and 16 hr. Insets: zoom-ins of the bottom of the vial. Whereas the better dispersion of the azidated graphene flakes vs. the non-azidated graphene flakes may be a combined result of the azido groups and the higher oxidation degree of the former (see text), the further improvement in dispersion upon click chemistry with alkyne-Cy3 is attributable to the high negative charges on Cy3.

4.3 Conclusion

Our successful azidation of graphene through electrochemically generated $N_3\cdot$ radicals is consistent with mounting evidence that free radicals are particularly effective in reacting with the graphene basal plane[15,20,22,24,54]. Although reagents as diazonium salts also enable radical reactions under ambient conditions, heavy side reactions often occur between the radicals and the already deposited layer[56]; the resultant surface is thus heterogeneous in chemical composition and height[7,24,53,106]. By starting with the simple N_3^- anion, which was converted into azidyl radicals *in*

situ at the graphene surface, our approach effectively precludes side reactions. Consequently, well-defined, covalently bond azido groups were obtained at high levels in minutes.

The monolayer azido groups bond to the graphene surface next uniquely offered a valuable handle for expanding surface functions. Whereas here we have already demonstrated both CuAAC and copper-free click chemistry, as well as subsequent biotin-streptavidin bioconjugation, azides are notably multifunctional:[139] other rich chemistry remains to be explored. In this work we further found that graphene maintained excellent conductivity and carrier mobility as the different surface functions substantially shifted the doping level. This finding bodes well for the potential application of these and related new materials for electronics and biosensing applications. Finally, by next demonstrating the possibility to bulk-produce azidated graphene flakes directly from natural graphite, we pointed to a new pathway to the high-throughput preparation of diverse graphene derivatives. We thus opened a new door to the facile, versatile covalent functionalization of graphene under ambient conditions.

4.4 Materials and methods

All sample preparation and characterization steps were performed under ambient conditions in the air at room temperature and near-neutral pH. Although sodium azide is a common salt in laboratory settings and is stable under ambient conditions, it is toxic and should be handled with care. In this work, we have used minimal amounts at moderate concentrations.

Preparation of monolayer graphene. Monolayer graphene grown on copper foils [42] (Graphene Supermarket, Calverton, NY or Graphenea, San Sebastián, Spain) was cut into ~2×10 mm strips, and wet transferred onto silicon chips coated with a 300 nm thermal oxide layer (SiO_2/Si) or #1.5 glass coverslips, following standard PMMA-based wet transfer methods [42]. After removal of PMMA using acetone and isopropanol, the graphene strips were contacted at both ends using conductive silver paint or pre-deposited Au electrodes [15].

Azidation of monolayer graphene. Sodium azide (identical results using Sigma-Aldrich 71289 and 769320) was dissolved in a 0.1 M pH = 7 sodium phosphate buffer (PB7) at 200 or 400 mM. A small (~150 µL) drop of the solution was placed at the center of the graphene strip, far away from the contacts on the two ends, thus creating both immersed and non-immersed areas in the same sample, divided by the drop boundary. A Ag/AgCl counter/reference electrode (3 M NaCl) contacted the solution drop from the top (Figure 38a inset). A Keithley 2400 SourceMeter was programmed to apply a voltage between the graphene and the Ag/AgCl electrodes and record the resultant electrochemical current. After the reaction, the sample was rinsed with 18 MΩ Milli-Q water and dried in air.

Azidation of freshly cleaved graphite surface. Freshly cleaved graphite surfaces were prepared by peeling off the upper layers of Natural Kish Graphite (Grade 200, Graphene Supermarket) using Kapton tape. The cleaved graphite surface was immediately immersed in a 400 mM NaN_3 solution in 0.1 M PB7, and a +1.3 V voltage was applied across the graphite piece and a Ag/AgCl electrode for 10 min. The sample was gently rinsed with Milli-Q water and dried in air.

Bulk production of azidated graphene flakes from graphite. A piece of Natural Kish Graphite (Grade 200, Graphene Supermarket) was mounted onto a glass coverslip and electrically contacted. The electrolyte for the preparation of azidated graphene flakes was an aqueous solution containing 200 mM NaN_3 and 400 mM Na_2SO_4. The electrolyte for the control experiment contained 400 mM Na_2SO_4 alone. A 400 µL drop of electrolyte was applied to cover the graphite piece, and a Pt wire was inserted as the counter electrode. A Keithley 2400 SourceMeter applied increasing voltages across graphite and Pt in 1 V steps until exfoliation occurred. For the Na_2SO_4–only electrolyte, rapid exfoliation occurred at +5 V, and was completed in ~3 min. For the NaN_3-Na_2SO_4 electrolyte, exfoliation occurred at +7 V, and was also completed in ~3 min. The suspended graphitic sheets from exfoliation were collected with centrifuge tube filters (Costar Spin-X 8161, Cole-Parmer; 0.22 µm pore size) and washed with Milli-Q water for four times. The final product was dispersed in ~200 µL water through a brief sonication, and drop-casted onto piranha-treated SiO_2/Si chips for XPS, AFM, and reflected light microscopy characterizations.

CuAAC of azidated graphene. An aqueous solution of 7 mM $CuSO_4$ and 33.3 mM THPTA [Tris(3-hydroxypropyltriazolylmethyl)amine; Sigma-Aldrich 762342] and an aqueous solution of 0.1 M sodium L-ascorbate were first prepared. For CuAAC of the azidated CVD graphene samples, 0.05 mg of alkyne-PEG_5-acid (764167; Sigma-Aldrich) or 0.02 mg of alkyne-Cy3 (TA117-1; Click Chemistry Tools, Scottsdale, AZ) or alkyne-PEG_4-biotin (TA105-25; Click Chemistry Tools) was dissolved in 468 µL of 0.1 M potassium phosphate buffer (pH = 7), to which 7.5 µL and 25 µL of the above $CuSO_4$-THPTA and sodium ascorbate solutions were respectively added. This reaction solution was dropped onto the entire sample to cover both the azidated and non-azidated areas for comparison of results. The sample was covered with aluminum foil for reaction in the dark for 1 h. The sample was rinsed with a 0.1 M potassium phosphate buffer for 3 times, and then rinsed with Milli-Q water and dried in air. For CuAAC of the azidated graphene flakes produced from bulk graphite, 0.02 mg of alkyne-Cy3 was dissolved in 268 µL of 0.1 M potassium phosphate buffer (pH = 7), to which 7.5 µL and 25 µL of the above $CuSO_4$-THPTA and sodium ascorbate solutions were respectively added. This reaction solution was added to azidated graphene flakes that were dispersed in 200 µL of 0.1 M potassium phosphate buffer. The sample was covered with aluminum foil for reaction in the dark for 1 h, and washed with Milli-Q water 4 times by centrifuging at 1000 rpm and removing the supernatant.

Copper-free cycloaddition of azidated graphene. 0.02 mg of ADIBO-PEG_4-biotin (Sigma-Aldrich 760749) was dissolved in 500 µL of 0.1 M potassium phosphate buffer (pH = 7). This reaction solution was similarly dropped onto the entire azidated CVD graphene sample, and allowed to react for 1 h in the dark. The sample was rinsed with a 0.1 M potassium phosphate buffer for 3 times, and then rinsed with Milli-Q water and dried in air.

Biotin-streptavidin conjugation. The biotinylated graphene surface, prepared above through either CuAAC or copper-free cycloaddition, was treated with 3% bovine serum albumin (BSA; Sigma-Aldrich A3059) in Dulbecco's phosphate-buffered saline (DPBS; Corning 21-031-cv) for 30 min. Alexa Fluor 555-conjugated streptavidin (Invitrogen S21381) was constituted as a 2 mg/mL stock solution in DPBS. 2 µL of this solution was added to 400 µL of DPBS containing 3% BSA, and the mixed solution was dropped onto the entire graphene sample. After 1 h of incubation in the dark, the sample was rinsed with DPBS 3 times, and then rinsed with Milli-Q water and dried in air.

XPS characterization. XPS spectra were obtained using a Perkin Elmer PHI 5600 XPS that operated at ~10^{-9} torr with a monochromatic Al Kα (1486.8 eV) X-ray source. A neutralizer was used to discharge accumulated charges from the sample surface. The above samples were characterized by both survey (0-1100 eV binding energy range) and high-resolution (15 or 20 eV binding energy window around the peaks of interest) scans. The control NaN_3 solid sample was prepared by letting dry in the air a ~150 μL drop of 200 mM NaN_3 aqueous solution on a clean SiO_2/Si substrate. Element compositions were determined from the peak areas using the factory-calibrated relative sensitivity factors.

Optical microscopy characterizations. Fluorescence microscopy, IRM, and reflected light microscopy were performed on an Olympus IX73 inverted epifluorescence microscope. Fluorescence microscopy and IRM were performed using an Olympus UplanSapo 60× water-immersion objective (numerical aperture 1.2) or UplanFl 100× oil-immersion objective (numerical aperture ~0.9 with iris diaphragm). Reflected light microscopy was performed using an Olympus UPlanFl 50× air objective. A white light source (Olympus U-HGLGPS) was used in combination with optical filters from Chroma (Bellows Falls, VT) and Thorlabs (Newton, NJ). For fluorescence microscopy of the labeled Cy3 and AF555 in the functionalized graphene, the excitation filter, dichroic mirror, and emission filter were ET545/25x (Chroma), zt561rdc-UF1 (Chroma), and ET605/70m (Chroma), respectively. For IRM and reflected light microscopy, the dichroic mirror position was mounted with a 50/50 beam splitter (Chroma 21000), and the emission filter position was left empty. For IRM, the excitation filter was D532/10x (Chroma) or FB450-10 (Thorlabs). For reflected light microscopy, the excitation filter was FF01-610/5-25 (Semrock). For all microscopy modes, wide-field images were recorded using an Andor Zyla 4.2 sCMOS camera.

AFM characterization. AFM was performed on an Asylum MFP-3D system in tapping mode using aluminum-coated probes (Tap300Al-G; BudgetSensors). Nominal values of the force constant, resonance frequency, and tip radius were 40 N/m, 300 kHz, and <10 nm, respectively. AFM data were processed using WsXM [140].

Electrical characterization. Graphene electrical properties were characterized through the contacts at the two ends of the graphene strip. A Keithley 2400 SourceMeter repeatedly scanned source-drain voltages through graphene in the range of −20 to +20 mV, and a second Keithley 2400 SourceMeter applied electrochemical gating voltages across the Ag/AgCl electrode and graphene (electrolyte was a 70 mM phosphate buffer). Linear *I*-*V* curves were obtained (Figure 47a and Figure 46), from the slopes of which conductance was calculated.

Chapter 5: Facile, electrochemical of graphene from an aqueous NaCl solution

The work in this chapter was conducted in collaboration with Wan Li and Ke Xu. It is reproduced in part here from ref[91] with permission from all co-authors.

5.1 Introduction

Chemical modifications provide key routes to expand the functionalities and potential applications of graphene.[22,24,103,104,141-145] Among the limited chemical modifications that have been accomplished for the inert graphene basal plane, chlorination is a notable success. To date, the chlorination of substrate-supported monolayer graphene has been achieved in two major ways, namely, plasma chlorination[132-135] and photochemical chlorination.[146-149] Separately, chlorinated graphitic and graphene-oxide flakes have been prepared from bulk graphite through UV-radiation, microwave-spark, and high-temperature exfoliation.[150-152] Although efficient chlorination has been achieved, these approaches all start with the toxic, corrosive elementary chlorine (Cl_2), and so require advanced reactors and/or high-vacuum systems.

In this chapter, we report a facile approach to chlorinate graphene under ambient conditions in an aqueous sodium chloride (NaCl) solution through electrochemistry. Electrochemistry offers powerful means for the preparation, characterization, functionalization, and application of graphene and related materials.[103,142,144,153-155] In the previous chapter, we reported the facile, electrochemical azidation of the graphene basal plane in an aqueous solution of sodium azide (NaN_3).[101] As azide is chemically analogous to halogens and, in fact, considered a pseudohalogen, we ask if an analogous strategy may enable graphene halogenation. We thus identify a facile, effective pathway for graphene chlorination, while finding the corresponding bromination and iodination reactions to be much less viable.

5.2 Results and discussion

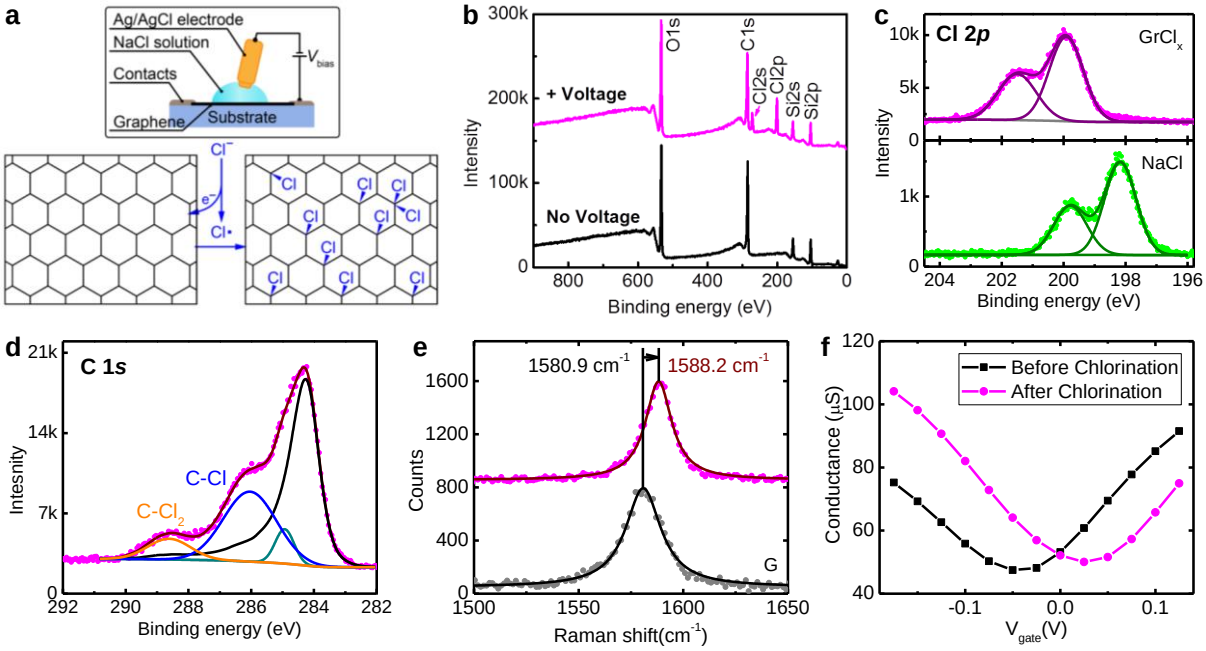

Figure 53. Facile chlorination of graphene through electrochemistry. (a) Schematics of the experimental setup and the chlorination mechanism. Electrochemical oxidation of aqueous chloride (Cl^-) at the monolayer graphene surface generates chlorine radicals ($Cl\cdot$), which react *in situ* with the basal plane to chlorinate graphene. (b) Survey-mode XPS spectra of monolayer graphene on a SiO_2/Si substrate after electrochemical reaction at 1.6 V (vs. Ag/AgCl) for 4 min in a pH = 3 phosphate buffer containing 1.5 M NaCl, versus a control sample that was immersed in the same solution for 10 min without applying voltage. (c) High-resolution XPS for the Cl 2*p* region of the chlorinated graphene (magenta) versus that of the starting NaCl salt (green). (d) High-resolution XPS for the C 1*s* region of the chlorinated graphene (magenta) in comparison to that of the starting monolayer graphene (black curve). The emergent blue and orange peaks are attributed to C−Cl and C−Cl_2 states, respectively. (e) Raman spectroscopy of graphene G band, before (black) and after (magenta) chlorination at 1.6 V for 4 min. (f) Graphene conductance as a function of the electrochemical gating voltage applied to the Ag/AgCl electrode vs. graphene before (black) and after (magenta) chlorination.

Figure 53a illustrates our electrochemical chlorination scheme. CVD-grown monolayer graphene was deposited as ~2×10 mm strips onto thermal oxide-coated silicon (SiO_2/Si) or glass substrates and fabricated into a working electrode for electrochemistry by electrically contacting at both ends. A ~60 μL drop of 1.5 M NaCl aqueous solution (in a pH = 3 phosphate buffer unless otherwise specified) was added to the center of the graphene strip, and the electrochemical cell was completed by inserting an Ag/AgCl (3 M NaCl) counter/reference electrode from the top. A Keithley 2401 SourceMeter provided an anodic voltage across the graphene strip and the Ag/AgCl electrode, which electrochemically oxidized chloride ions (Cl^-) in the solution at the graphene surface to generate chlorine radicals ($Cl\cdot$) for *in situ* reaction with the graphene basal plane. We note that efficient chlorination was also achieved when using a Pt wire as the counter/reference electrode (Figure 54), although we focus on results from the better-referenced Ag/AgCl electrode below.

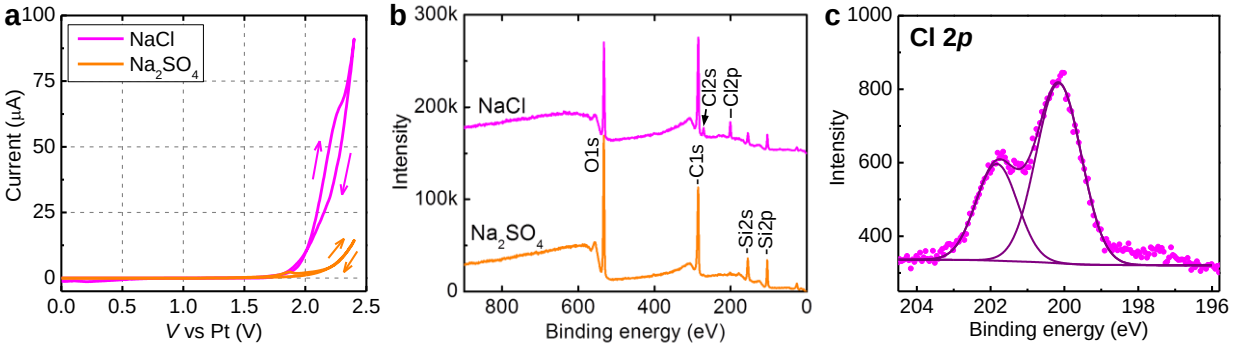

Figure 54. Electrochemical chlorination of graphene using a Pt wire as the counter/reference electrode. (a) Cyclic voltammograms measured vs. the Pt wire for monolayer graphene in 200 mM pH = 3 phosphate buffers with the addition of 1.5 M NaCl (magenta curve) vs. with the addition of 0.5 M Na_2SO_4 (orange curve). Scanning rate: 19 mV/s. (b) Survey-mode XPS spectra of two monolayer graphene devices on SiO_2/Si substrates after electrochemical reactions at 2.1 V (vs. Pt) for 4 min in the above two solutions. (c) High-resolution XPS for the Cl 2*p* region of the chlorinated graphene produced with the NaCl solution in (b).

Figure 53b shows the survey-mode X-ray photoelectron spectrum (XPS) measured for a graphene sample that was chlorinated through the above process by applying an anodic voltage of 1.6 V (vs. Ag/AgCl) for 4 min in two 2-min cycles (Materials and methods), compared to a control sample that was immersed in the same NaCl solution for 10 min but without applying voltage. Pronounced Cl 2*s* and Cl 2*p* peaks emerged after the electrochemical chlorination process. As another control, we also examined graphene subjected to electrochemical oxidation in a $NaSO_4$ solution, and found no Cl peaks appeared (Figure 54).

High-resolution spectrum for the Cl2*p* region (Figure 53c) showed two peaks at 200.0 eV and 201.6 eV at an ~2:1 area ratio, consistent with that expected for Cl $2p_{3/2}$ and Cl $2p_{1/2}$ components in C−Cl bonds in chlorinated graphene.[133,146,151] In comparison, the Cl $2p_{3/2}$ and Cl $2p_{1/2}$ components of chloride (Cl^-) from the starting NaCl salt were found at much lower binding energies of ~198.2 eV and 199.7 eV (Figure 53c), as expected. Meanwhile, high-resolution spectrum for the C 1*s* region (Figure 53d) showed two significant new features at 286.0 eV and 288.6 eV, consistent with that of C−Cl and $C-Cl_2$ states in chlorinated graphene and other chlorinated organic compounds.[149,156] Together, these results suggest the successful formation of C−Cl bonds on graphene through the electrochemical process.

Quantitative analysis based on the areas of Cl 2*p* and C 1*s* peaks and factory-calibrated relative sensitive factors (Materials and methods) showed a Cl:C atomic ratio of 17%, equivalent to one chlorine atom being added to every 5-6 carbon atoms. This result compares well with previous chlorination efforts for substrate-supported monolayer graphene based on plasma[132-135] and photochemical[146-149] approaches, which typically achieve Cl:C atomic ratios of 8-40%. Following the reasoning of these previous studies that graphene should be impervious to the reactant, chlorination likely occurred for the exposed side of the graphene monolayer. Whereas it is difficult to map out the local chlorination degree with existing methods, our recent results on the electrochemical azidation of graphene through analogous radical reaction mechanisms have indicated uniform reaction of the graphene basal plane through the fluorescence microscopy of a clicked dye.[101]

Raman spectroscopy and electrical measurements further showed that chlorination substantially altered the doping level of graphene without introducing significant structural defects to the basal plane. For Raman spectroscopy, both the graphene G and 2D bands blue-shifted notably (Figure 53e and Figure 55), indicating enhanced doping. Meanwhile, a small D peak was detected with $I_D/I_G \sim 0.03$ (Figure 55), suggesting minimal defect generation in the basal plane. The above Raman spectroscopy results are consistent with recent results on monolayer graphene chlorinated by both plasma[133,135] and photochemistry[149] approaches, although earlier photochemical chlorination studies have reported larger Raman D bands.[146]

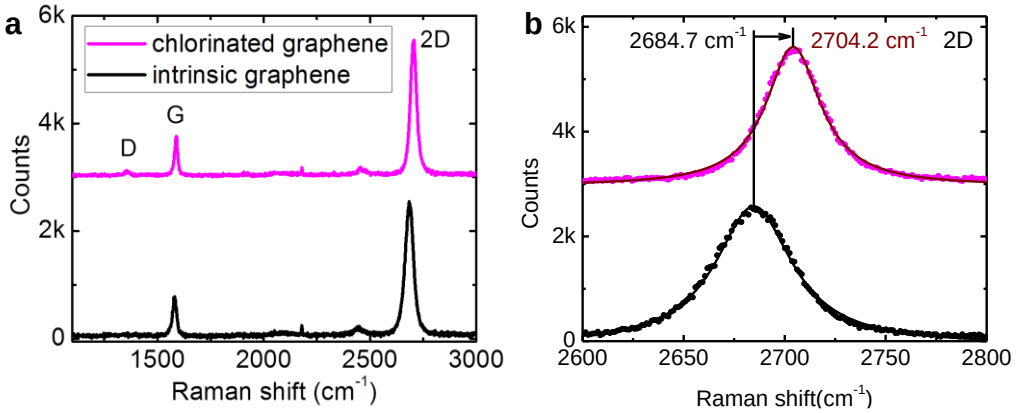

Figure 55. Raman spectra of a monolayer graphene sample on a SiO_2/Si substrate before (black) and after (magenta) chlorination at 1.6 V (vs. Ag/AgCl) for 4 min. (a) Full spectra. (b) Zoom-in of the 2D band, showing a substantial blue shift after chlorination.

Gate-dependent electrical measurements showed a substantial positive voltage shift of the Dirac point after chlorination (Figure 53f), thus *p*-doping due to the high electronegativity of Cl. At the same time, high graphene conductance was preserved, again suggesting good integrity of the graphene basal plane. These electrical characterization results are also in general agreement with previous chlorination results based on plasma[132,133,135] and photochemistry[147,149] approaches.

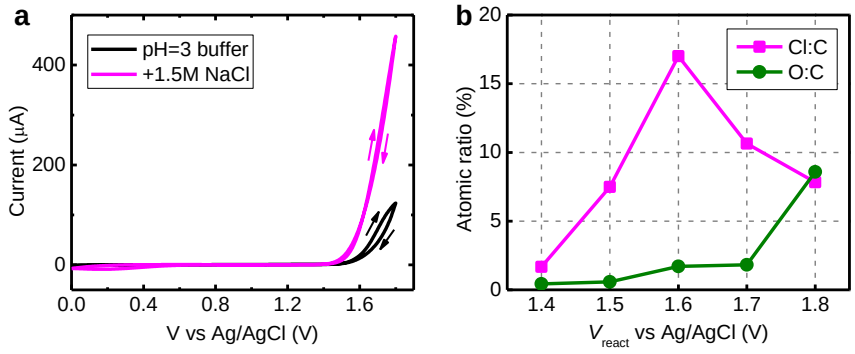

Figure 56. Voltage dependency of the chlorination process. (a) Cyclic voltammograms measured using the same monolayer graphene electrode in a 200 mM pH = 3 phosphate buffer (black) vs. in the same buffer with the addition of 1.5 M NaCl (magenta). Scanning rate: 19 mV/s. (b) XPS-determined Cl:C and O:C atomic ratios for monolayer graphene samples chlorinated in the NaCl solution for 4 min at different constant voltages. The O:C atomic ratios were calculated after subtracting the calibrated oxygen amounts from the SiO_2 substrate.

To better understand the reaction mechanism, we examined the voltage dependency of the chlorination process. Cyclic voltammetry of the graphene electrode in a blank pH = 3 phosphate buffer showed a rise in current as the voltage increased beyond ~1.5 V (vs. Ag/AgCl) (black curve in Figure 56a), attributable to the electrolysis of water.[15,101] Adding 1.5 M NaCl to the buffer shifted the current onset voltage to ~1.4 V and led to a substantial increase in the current level (magenta curve in Figure 56a), attributable to the oxidation of chloride (Cl^-). As a control, adding Na_2SO_4 to the same ionic strength did not noticeably shift the onset voltage or raise the current level (Figure 57). Based on the above results, we examined through XPS the graphene chlorination efficiency achieved in the NaCl solution at different fixed voltages (Figure 56b). Whereas minor chlorination was observed for 4 min reaction at 1.4 V, substantial (~8% Cl:C atomic ratio) chlorination was achieved at 1.5 V, and an even higher Cl:C atomic ratio of 17% was achieved at 1.6 V, in line with the increased electrochemical current and hence Cl· generation at the graphene surface. Further increasing the applied voltages to 1.7 and 1.8 V, however, led to reduced chlorination, possibly owing to the self-combination of chlorine radicals ($2\ Cl\cdot \rightarrow Cl_2$) at high concentrations before reaction with graphene could take place. Subtracting the oxygen contributions from the SiO_2 substrate further showed that minimal graphene oxidation (<2% O:C atomic ratio) occurred for voltages ≤ 1.7 V (vs. Ag/AgCl), whereas an ~8% O:C atomic ratio was found for the high voltage of 1.8 V (Figure 56b).

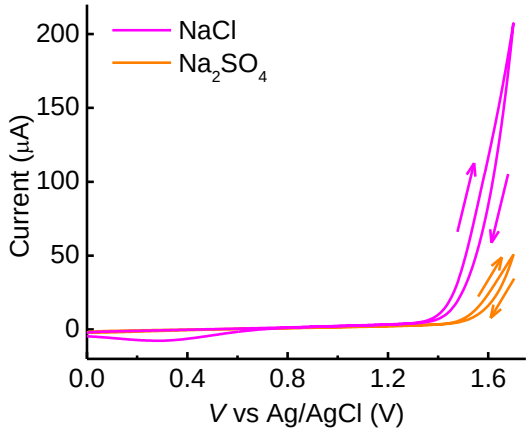

Figure 57. Cyclic voltammograms of a graphene electrode in a pH = 3 buffer with the addition of NaCl or Na_2SO_4 to the same ionic strength. A three-electrode configuration was used with graphene as the working electrode, a Pt wire as the counter electrode, and an Ag/AgCl electrode as the reference electrode. The same monolayer graphene electrode was measured in 200 mM pH = 3 phosphate buffers with the addition of 1.5 M NaCl (magenta curve) vs. with the addition of 0.5 M Na_2SO_4 (orange curve). Scanning rate: 19 mV/s.

To elucidate how the electrochemical chlorination and oxidation processes compete with each other, we deposited graphene onto glass coverslips to enable interference reflection microscopy (IRM), a method we recently developed to enable the *in situ* detection of graphene morphology changes and chemical reactions with excellent contrast and spatial resolution.[4,14,15] For a graphene electrode in a blank, pH = 3 phosphate buffer, IRM thus showed that the application of a 1.6 V voltage (vs. Ag/AgCl) for 40 s led to quick electrochemical oxidation with varying local oxidation degrees of ~30-70% (Figure 58ad), in agreement with our recent results.[15] Notably, adding 1.5 M

NaCl to the buffer efficiently suppressed graphene oxidation under the same conditions (Figure 58b), so that the average oxidation degrees were ~5% (Figure 58d). This small amount of oxidation was further readily reversed by the brief application of a reductive voltage at 0 V vs. Ag/AgCl (Figure 58c), in agreement with our recent demonstration of the reversible electrochemical oxidation and reduction of graphene.[15]

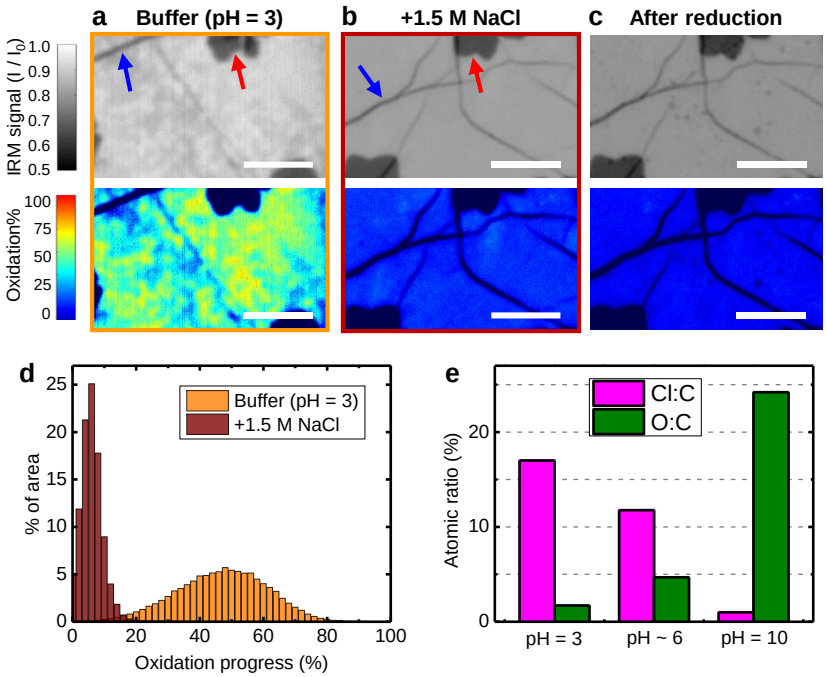

Figure 58. Suppression of electrochemical oxidation facilitates graphene chlorination in the acidic NaCl solution. (a) *In situ* IRM image (top) and the converted map of local oxidation degree (bottom) of a monolayer graphene sample on a glass substrate in a pH = 3 phosphate buffer, after applying 1.6 V vs. Ag/AgCl for 40 s. Blue and red arrows point to wrinkles and sporadic bilayer islands in the monolayer graphene; see interpretation of IRM images in Refs. [15] and [4]. (b) *In situ* IRM image (top) and converted map of local oxidation degree (bottom) for another sample with 1.5 M NaCl added to the buffer, after the same voltage applied. (c) The same sample after ensuing electrochemical reduction at 0 V vs. Ag/AgCl for 60 s. (d) Distributions of local oxidation degree obtained from the spatial maps in (a) and (b). (e) XPS-determined Cl:C and O:C atomic ratios for graphene samples on SiO_2/Si substrates after electrochemical chlorination at 1.6 V (vs. Ag/AgCl) in 1.5 M NaCl dissolved in a phosphate buffer (pH = 3), MilliQ water (pH ~ 6), and a carbonate buffer (pH = 10). Scale bars: 5 μm (a-c).

The observed efficient suppression of graphene oxidation may be understood as that the hydroxyl radical (HO·), the major intermediate species that drives the electrochemical oxidation of graphene,[15,125] reacted off with the abundant chloride in the solution to produce chlorine radicals. In acidic solutions, a two-step mechanism is well-established for this process:[157]

$$OH\cdot + Cl^- \rightleftharpoons ClOH\cdot^- \qquad (1)$$

$$ClOH\cdot^- + H^+ \rightarrow Cl\cdot + H_2O \qquad (2)$$

Thus, graphene oxidation due to the hydroxyl radical was suppressed and additional chlorine radical was generated to further facilitate chlorination. The end product is thus highly chlorinated graphene (Cl:C ratio ~17%) with little oxidation (O:C ratio ~1.7%) (Figure 58e).

The above mechanism implies that the conversion of the hydroxyl radical into the chlorine radical would be more efficient in acidic solutions, as Step (2) requires proton. Indeed, previous experiments on the OH· scavenging capability of chloride in the H_2O_2/UV process have shown ~100-fold difference in the equilibrated OH· concentration at pH = 3 vs. pH = 6.[158] Consistent with this pH-dependent equilibrium between the OH· and Cl· radicals, we found substantially higher oxidation and lower chlorination levels of graphene for electrochemical chlorination carried out at increased pHs, namely, 1.5 M NaCl in the near-neutral MilliQ water (pH ~ 6) and a basic buffer (pH = 10) (Figure 58e).

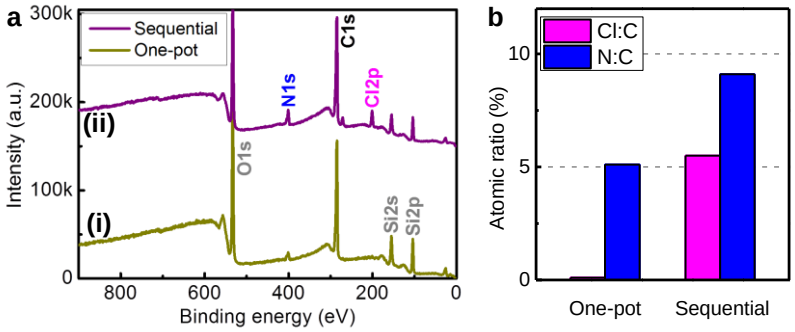

Figure 59. Electrochemical bi-functional chlorination-azidation of graphene. (a) Comparison of XPS results for two monolayer graphene samples respectively processed by (i) One-pot electrochemical reaction at 1.6 V (vs. Ag/AgCl) for 4 min in a pH = 7 phosphate buffer containing both 1.5 M NaCl and 200 mM NaN_3; (ii) Sequential electrochemical reactions, with the first step being chlorination at 1.6 V (vs. Ag/AgCl) for 4 min in 1.5 M NaCl in a pH = 3 phosphate buffer, and the second step being azidation at 1.3 V (vs. Ag/AgCl) for 5 min in 200 mM NaN_3 in a pH = 7 phosphate buffer. (b) Cl:C and N:C atomic ratios of the two samples.

In an attempt to achieve graphene bi-functionalization[159,160] and also to compare the relative efficacies of electrochemical chlorination and azidation, we next applied a 1.6 V (vs. Ag/AgCl) voltage for a graphene sample in a solution containing both 1.5 M NaCl and 200 mM NaN_3. To avoid formation of the volatile and highly toxic hydrazoic acid (HN_3), a neutral (pH = 7) phosphate buffer was employed. Remarkably, even though the concentration of chloride was 7.5 times of azide in the reactant solution, XPS showed that the graphene was only azidated but not chlorinated (Figure 59ab). This result is explainable, as the azide ion (N_3^-) is more readily oxidized to form the azide radical (N_3·) when compared to the oxidation of Cl^- to form Cl·: we have previously shown that for graphene electrodes in NaN_3 solutions, the electrochemical current rises quickly for >0.9 V (vs. Ag/AgCl) due to the oxidation of N_3^-, and efficient graphene azidation occurred at >1.0 V,[101] much lower than the >~1.5 V required for chlorination (Figure 56). The NaN_3 solution also fully suppresses the electrochemical oxidation of graphene at 1.6 V (vs. Ag/AgCl) due to the consumption of the hydroxyl radical by N_3^- to produce OH^- and N_3·.[101,126] It is thus likely that in a similar fashion, N_3^- suppressed graphene chlorination in the NaCl-NaN_3 solution: any chlorine radical formed through electrochemical oxidation would react off with N_3^- to produce Cl^- and N_3·, before graphene chlorination could ever take place. Quantification of the XPS data showed an N:C

atomic ratio of 5% for the azidated product (Figure 59b), lower than that found when 200 mM NaN_3 is used alone without NaCl (~10%).[101] This result may be attributed to side reactions of azide radicals with chlorine, which could lead to undesired species as chlorine azide.[161]

Consequently, we took a different strategy to chlorinate-azidate graphene in two steps, with the first step being chlorination at 1.6 V (vs. Ag/AgCl) in 1.5 M NaCl in a pH = 3 phosphate buffer, and the second step being azidation at 1.3 V (vs. Ag/AgCl) in 200 mM NaN_3 in a pH = 7 phosphate buffer. This sequential approach enabled successful bi-functionalization of graphene (Figure 59a), with Cl:C and N:C atomic ratios of 6% and 9% being achieved, respectively (Figure 59b).

We conclude by examining whether the above facile electrochemical chlorination scheme for graphene may be extended to bromination and iodination by applying an anodic voltage to graphene in NaBr and KI solutions. As expected, we found the electrochemical oxidation of Br^- and I^- ions occurred at the graphene surface at lower voltages (Figure 60 and Figure 61), and such processes effectively suppressed the electrochemical oxidation of graphene (Figure 60) as the hydroxyl radical readily reacts with Br^- and I^- ions to form Br· and I· radicals.[162,163] For the case of I^-, we further observed the deposition of solid I_2 at the graphene surface (Figure 61). XPS data, however, showed limited bromination (Br:C atomic ratio ~0.8%, with bonded and adsorbed Br each at ~0.4%) and iodination (I:C atomic ratio ~0.1%) levels (Figure 60 and Figure 61). These results may be related to the lower chemical reactivity of Br· and I· radicals when compared to the Cl· and N_3· radicals: before reaction with the graphene basal plane could occur, the Br· and I· radicals may combine to generate elementary Br_2 and I_2 (Figure 61), as well as to further incorporate Br^- and I^- in the solution to form tri-halide anions. Previous theoretical and experimental studies both suggest similar trends that brominated and iodinated graphitic derivatives are less stable, and that halogenation levels of >~1% Br:C and I:C atomic ratios are difficult to achieve.[143,145,151,152,164-166]

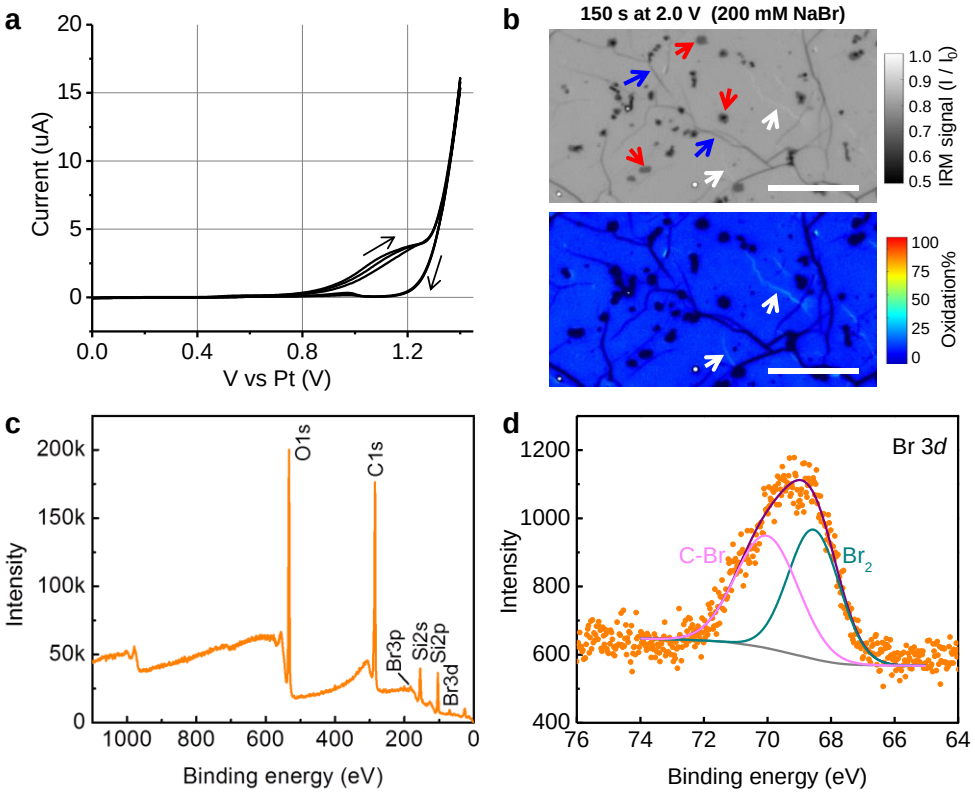

Figure 60. Electrochemical bromination of graphene in an aqueous NaBr solution. (a) Cyclic voltammograms measured with a graphene electrode in a pH = 3 phosphate buffer containing 1 M NaBr. Electrochemical current due to the oxidation of Br^- rose at ~0.8 V (vs. Pt). (b) *In situ* IRM images (top) and the converted map of local oxidation degree (bottom) for a graphene sample on a glass substrate after electrochemical reaction at 2.0 V vs. Pt for 150 s in a pH = 3 phosphate buffer containing 200 mM NaBr. Electrochemical oxidation of graphene was completed suppressed. Arrows: wrinkles (blue), sporadic bilayer islands (red), and minor cracks in the monolayer graphene (white). The IRM signal does not faithfully reflect the local oxidation degree at these structural defects. Scale bars: 10 μm. (c) Survey-mode XPS spectra of monolayer graphene on a Si/SiO_2 substrate after electrochemical reaction at 1.6 V vs Pt for 4 min in a pH = 3 phosphate buffer containing 1 M NaBr. (d) A detailed scan of the Br 3*d* signal. This signal is fitted by two peaks centered at 70.2 eV and 68.5 eV, attributable to the C-Br bond in brominated graphene and physically adsorbed Br_2, respectively.[151,165,166] Quantification of the signal areas indicated a total Br:C atomic ratio of 0.8%, with bonded and adsorbed Br each at ~0.4%.

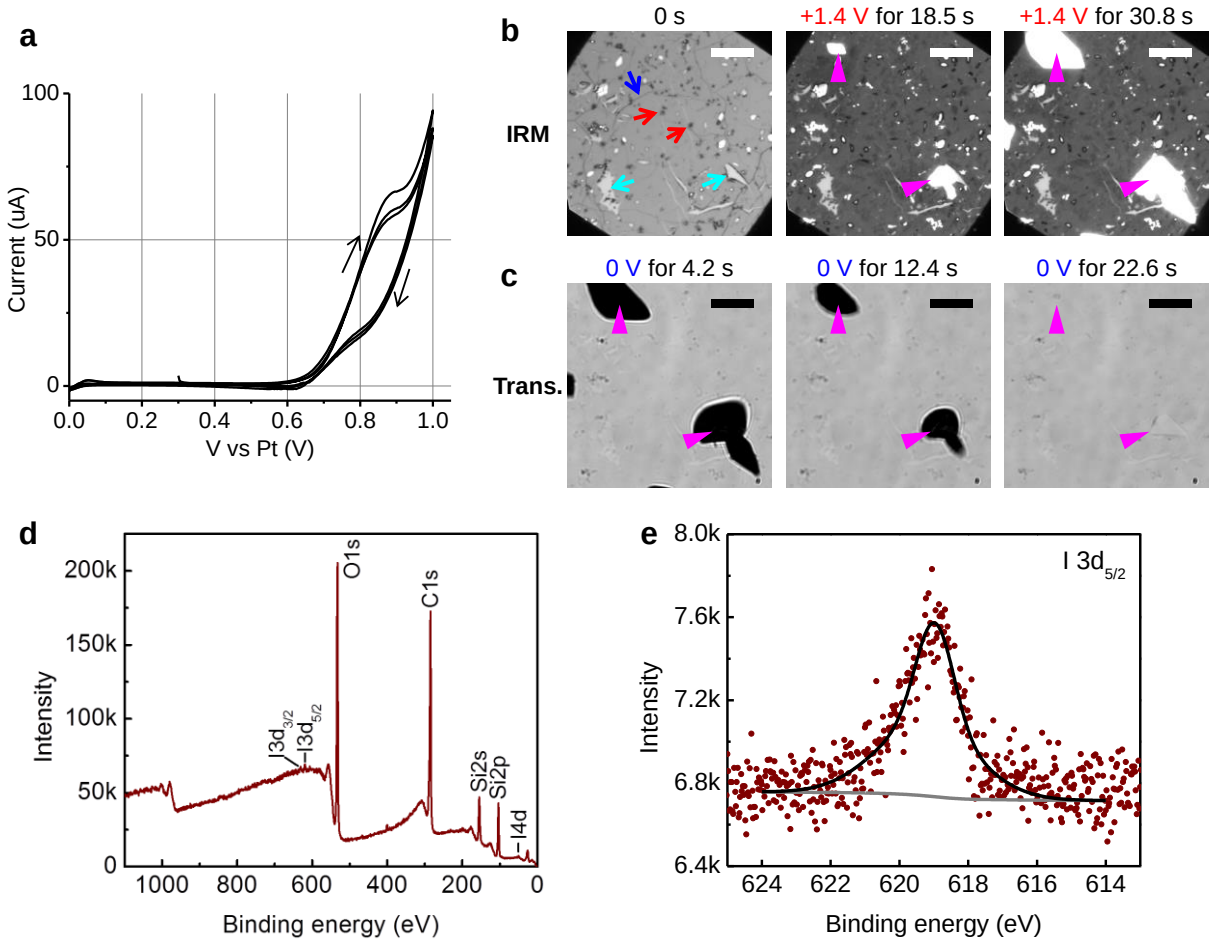

Figure 61. Electrochemical iodination of graphene in an aqueous KI solution. (a) Cyclic voltammograms measured with a graphene electrode in a pH = 3 phosphate buffer containing 200 mM KI. Electrochemical current due to the oxidation of I^- rose at ~0.6 V. (b) *In situ* IRM image for a graphene sample on a glass substrate, before (left) and after electrochemical reaction at 1.4 V (vs. Pt) in a pH = 3 phosphate buffer containing 200 mM KI for 18.5 s (center) and 30.8 s (right). Arrows: wrinkles (blue), sporadic bilayer islands (red), and minor tears (cyan) in the monolayer graphene. Magenta arrowheads: growth of I_2 islands on the graphene surface. The IRM images overall darkened due to the generation of dissolved I_2 and I_3^- in the solution, yet became exceedingly bight locally for the deposited I_2 islands owing to reflection. Scale bars: 10 μm. (c) Same sample, next under transmission microscopy and with the application of a reductive voltage of 0 V (vs. Pt) for 12.4 s and 22.6 s. Magenta arrowheads point to the deposited I_2 islands on the graphene surface, which appeared dark due to the absorption of light, and were quickly reduced under the reductive voltage. Scale bars: 10 μm. (d) Survey-mode XPS spectra of monolayer graphene on a Si/SiO_2 substrate after electrochemical reaction in a pH = 3 phosphate buffer containing 1 M KI at 1.4 V vs. Pt for 4 min. (e) Detailed scan of the I 3 $d_{5/2}$ signal. An I:C atomic ratio of 0.1% was calculated from the areas of I3 $d_{5/2}$ and C 1*s* peaks.

5.3 Conclusion

In summary, we have demonstrated the successful, direct chlorination of monolayer graphene under ambient conditions through the *in situ* electrochemical generation of chlorine radicals at the

graphene surface. By starting with an aqueous NaCl solution, our approach required no toxic chemicals or special equipment, and achieved good, reaction voltage-tunable chlorination of up to 17% Cl:C. While exhibiting strong *p*-doping, the chlorinated graphene maintained good basal-plane integrity and electrical properties. IRM and pH-dependent experiments elucidated the competition between electrochemical chlorination and oxidation processes due to Cl· and OH· radicals, and thus rationalized acidic conditions for optimal chlorination. Electrochemical oxidation in a NaCl-NaN_3 mixture next showed that the generation of N_3· radicals fully suppressed graphene chlorination in favor of azidation, yet we demonstrated a sequential, two-step chlorination-azidation approach to permit facile bi-functionalization. Finally, we showed that the analogous graphene bromination and iodination reactions to be much less viable due to the low reactivity of Br· and I· radicals. Together, the facile chlorination we achieved and the mechanisms we elucidated call for new attention to the radical-mediated electrochemical functionalization of graphene and related nanomaterials.

5.4 Materials and methods

Preparation of monolayer graphene. Monolayer graphene grown on copper foils (ACS Material or Graphene Supermarket) was cut into ~2×10 mm strips, and wet-transferred onto silicon chips coated with a 300 nm thermal oxide layer (SiO_2/Si) or #1.5 glass coverslips, following the standard PMMA-based wet transfer method with a modified RCA cleaning process.[100] After the removal of PMMA using acetone and isopropanol, the graphene strips were contacted at both ends using conductive silver paint.

Electrochemical chlorination of monolayer graphene. Best chlorination results were achieved in 1.5 M NaCl dissolved in a 200 mM pH = 3 potassium phosphate buffer. For examination of the pH dependence of chlorination efficiency, 1.5 M NaCl was dissolved in 18 MΩ Milli-Q water (pH ~ 6) or a 200 mM pH =10 sodium carbonate buffer. A small (~50-80 μL) drop of the NaCl solution was carefully placed at the center of the graphene strip without contacting the silver paint on either ends. An Ag/AgCl counter/reference electrode (3 M NaCl) was then inserted into the solution drop from the top to complete the electrochemical cell. A Keithley 2401 SourceMeter was programmed to apply voltages to graphene versus the Ag/AgCl electrode and record the resultant electrochemical current. To avoid the potential electrochemical oxidation of graphene due to a long-lasting oxidative reaction voltage, chlorination was carried out in two cycles, with each cycle starting with a constant oxidative voltage in the range of 1.4-1.8 V for 2 min, and then followed by a recovery period of 1 min at a reductive voltage at 0 V vs Ag/AgCl. The sample was then rinsed with Milli-Q water and dried in the air. For reaction in the mixed NaCl-NaN_3 solution, 1.5 M NaCl and 200 mM NaN_3 were added into a pH = 7 phosphate buffer, and a constant oxidative voltage of 1.6 V (vs. Ag/AgCl) was similarly applied to the graphene electrode in two 2-min cycles followed by 1-min recovery periods at 0 V. For sequential electrochemical chlorination-azidation, the graphene sample was first chlorinated at 1.6 V (vs. Ag/AgCl) in 1.5 M NaCl in a pH = 3 phosphate buffer as described above, rinsed with Milli-Q water, and then azidated at 1.3 V (vs. Ag/AgCl) in 200 mM NaN_3 in a pH = 7 phosphate buffer for 5 min.

Electrochemical bromination and iodination of monolayer graphene. The electrochemical cells were constructed similarly as above, except that 1 M NaBr and 1 M KI in 200 mM pH = 3 potassium phosphate buffers were used for bromination and iodination, respectively, and the

counter/reference electrode was a Pt wire. A constant voltage of 1.6 V and 1.4 V vs. Pt was applied to graphene for 4 min for bromination and iodination, respectively.

XPS and Raman characterizations. XPS spectra were obtained for samples on SiO_2/Si substrates using a Perkin Elmer PHI 5600 XPS that operated at ~10^{-9} torr with a monochromatic Al Kα (1486.8 eV) X-ray source. The above samples were characterized by both survey-mode (0-1100 eV binding energy range) and high-resolution (15 or 20 eV binding energy window around the peaks of interest) scans. The control NaCl solid sample was prepared by letting dry in the air a ~150 μL drop of 200 mM NaCl aqueous solution on a clean SiO_2/Si substrate. For quantification,[167] the Shirley's algorithm was applied to determine the background when calculating the XPS peak areas. Cl:C, Br:C, and I:C atomic ratios were calculated from the peak areas from high-resolution XPS measurements using the factory-calibrated relative sensitivity factors. O:C atomic ratios were calculated from survey-mode XPS measurements using the factory-calibrated relative sensitivity factors after subtracting the oxygen component from the SiO_2 substrate, which was calibrated to have a fixed O:Si atomic ratio of 2.02±0.01. Raman spectra were recorded with a Renishaw InVia micro-Raman system using a 488 nm laser and a 2400 lines/mm grating.

Electrical and electrochemical characterizations. Graphene electrical properties were characterized through the contacts at the two ends of the graphene strip. A Keithley 2401 SourceMeter repeatedly scanned source-drain voltages through graphene in the range of −20 to +20 mV, and a Keithley 2400 SourceMeter applied electrochemical gating voltages across the Ag/AgCl electrode and graphene (electrolyte was a 200 mM pH = 3 phosphate buffer). Linear *I*-*V* curves were obtained, from the slopes of which conductance was calculated. Cyclic voltammetry was carried out under a three-electrode configuration, using graphene as the working electrode, a Pt wire as the counter electrode, and an Ag/AgCl electrode as the reference electrode. The Keithley 2401 SourceMeter was connected in a 4-wire configuration and programmed to sweep the voltage between the working and reference electrodes and record the resultant electrochemical current between the working and counter electrodes.

Interference reflection microscopy (IRM). For IRM, graphene samples were deposited on #1.5 glass coverslips. IRM was performed as described previously[4] on an Olympus IX73 inverted epifluorescence microscope using a UplanFl 100× oil-immersion objective lens (numerical aperture ~0.9 with iris diaphragm) and a white light source (Olympus U-HGLGPS). The excitation filter was D532/10x (Chroma), the dichroic mirror position was mounted with a 50/50 beam splitter (Chroma 21000), and the emission filter position was left empty. Wide-field images were recorded using an Andor Zyla 4.2 sCMOS camera. For *in situ* monitoring of the electrochemical oxidation of graphene, the IRM signal was converted into the local degree of oxidation, as discussed previously.[14,15] Briefly, the IRM signal depends strongly on the imaginary part of the complex index of refraction of the sample, which is related to the conductivity of the material. The big difference in the refractive indices of graphene and graphene oxide at $n_{Gr} = 2.65 + 1.27i$ and $n_{GO} = 1.75 + 0.17i$ thus leads to substantial IRM contrast. When expressed as $C = I/I_0$, I and I_0 being the absolute IRM signals at the sample and at the bare glass substrate, respectively, $C_{Gr} = 0.73$ for the former and $C_{GO} = 0.97$ for the latter. The local oxidation degree at each pixel, with local IRM contrast measured as $C_{pixel} = I_{pixel}/I_0$, is thus estimated as:[14,15] $(C_{pixel} - C_{Gr}) / (C_{GO} - C_{Gr})$.

Chapter 6: Visible light azidation and chemical patterning of graphene via photoredox catalysis

6.1 Introduction

Whereas chemical modifications offer great promise for expanding the functionalities and potential applications of graphene,[20,22-24,54,103,104,168-172] the chemical inertness of the basal plane limits the available reaction approaches. Spatial patterning of chemical modifications[7,10,33,53,59,173-182] presents yet another level of challenge. Radical reactions provide key routes to graphene functionalization.[20,22,24,54] Our recent work has shown that in aqueous solutions, free radicals electrochemically generated at the graphene surface permit efficient reactions.[15,91,101] In particular, in aqueous NaN_3 solutions, electrochemically generated azidyl radicals ($N_3\cdot$) effectively azidate monolayer graphene, hence a versatile product that enables chemically defined derivations through click chemistry and subsequent bioconjugation.[101]

In this chapter, we report a facile, aqueous solution-based photosensitized pathway for graphene azidation, which removes the need to wire up graphene for electrochemistry while further enabling chemical patterning with low-intensity visible light.

Although free radicals generated from photodissociation have proved valuable for graphene reactions, surface depositions, and patterning,[34,53,59-62,174,177-179] high-power illumination is often required to activate the reactants. Limited choices are available based on the optical absorptions and chemical activities of the specific reactants, and it is often difficult to further convert the functionalized graphene to other chemically defined surface functionalizations.

To achieve efficient photoreaction with visible light, and specifically, to remove one electron from aqueous-phase N_3^- to produce $N_3\cdot$ for graphene azidation and the ensuing versatile click chemistry, we consider single-electron-transfer photosensitizers. To this end, photoredox catalysis, *e.g.*, with tris(bipyridine)ruthenium(II) chloride $[Ru(bpy)_3]Cl_2$, has in recent years emerged as a powerful tool in organic synthesis for driving radical reactions with visible light.[183-185] A critical comparison is recently made between reactions due to photoredox catalysis and electrochemistry,[186] and the generation of nitrogen-centered radicals by photoredox catalysis has been reviewed.[187] Yet, we are unaware of prior attempts to employ photoredox catalysis to activate aqueous N_3^- anions, or to initiate other reactions for graphene and like nanomaterials.

6.2 Results and discussion

In aqueous solutions, $[Ru(bpy)_3]^{2+}$ exhibits a broad absorption band centered at ~450 nm (blue light) due to metal-to-ligand charge transfer. In the presence of a sacrificial oxidant as peroxodisulfate, the resultant triplet excited state loses an electron to yield the potent oxidant $[Ru(bpy)_3]^{3+}$ (Figure 1a). We reason that in an aqueous solution of NaN_3, $[Ru(bpy)_3]^{3+}$ may oxidize the azide anion N_3^- to produce the azidyl radical $N_3\cdot$ (Figure 1a). Indeed, one early study has examined the equilibrium between the $[Ru(bpy)_3]^{3+}/[Ru(bpy)_3]^{2+}$ and $N_3\cdot/N_3^-$ redox pairs, in which $N_3\cdot$ was generated through radiolysis.[188] The same equilibrium should be established if

$[Ru(bpy)_3]^{3+}$ is instead generated from the above photosensitization process. The resultant azidyl radicals may azidate graphene (Figure 62b), as we have demonstrated with electrochemistry.[101]

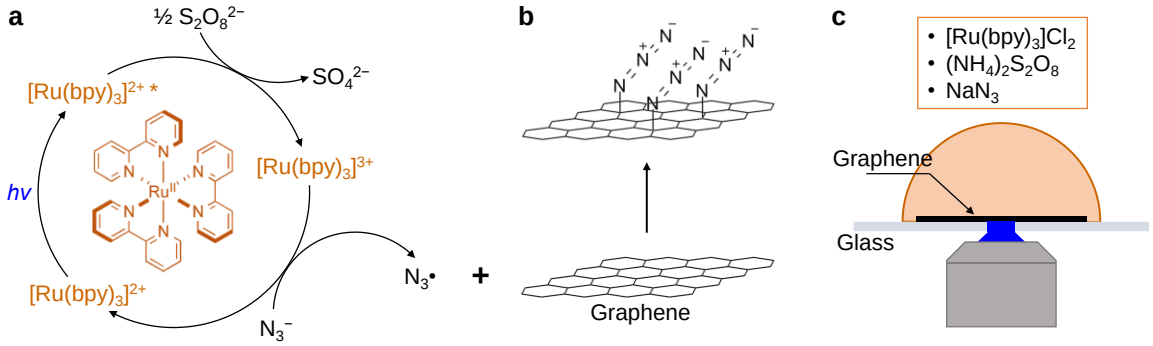

Figure 62. Schematics. (a,b) Reaction mechanisms. (a) Blue light excites $[Ru(bpy)_3]^{2+}$ into a triplet excited state $[Ru(bpy)_3]^{2+*}$, which readily loses one electron to peroxodisulfate to generate the highly active oxidant $[Ru(bpy)_3]^{3+}$. $[Ru(bpy)_3]^{3+}$ oxidizes N_3^- in the solution to azidyl radical (N_3·) and returns to the starting $[Ru(bpy)_3]^{2+}$. (b) The photogenerated N_3· reacts with graphene to produce azidated graphene. (c) Experimental setup: a drop of aqueous solution containing $[Ru(bpy)_3]Cl_2$, $(NH_4)_2S_2O_8$, and NaN_3 is deposited on graphene on a glass coverslip. A region of the sample is evenly illuminated with blue light of preset patterns in the wide field through a microscope objective lens.

Monolayer graphene was deposited on glass substrates and mounted on a standard inverted wide-field epifluorescence microscope. $[Ru(bpy)_3]Cl_2$ was dissolved at 0.1 mM in a pH = 7 aqueous buffer containing 200 mM ammonium persulfate and 200 mM NaN_3. A small drop of this reactant solution was cast on the graphene surface. Using a standard filter cube, blue light was selected from a white lamp and introduced into the objective lens to illuminate the sample in the wide field at low power densities of ~10 mW/cm^2 (Figure 1c). Starting with a 4x low-magnification objective lens, we evenly illuminated an area of ~3 mm diameter, which suited well for the X-ray photoelectron spectroscopy (XPS) characterization of the product. Notably, the illumination led to the visible formation of bubbles: similar behavior has been noted in the electrochemical azidation of graphene,[101] suggesting the generation of excessive azidyl radicals, which self-combine to form N_2 gas ($2\ N_3\cdot \rightarrow 3N_2$).

Figure 63a shows the XPS result of a sample that was illuminated at 40 mW/cm^2 for 15 min (orange curve). Notably, when compared to the untreated graphene (black curve), as well as a control sample that was immersed with the same reactant in the dark (blue curve), a substantial nitrogen 1s peak emerged in the illuminated sample. Examination of the high-resolution spectra (Figure 63b) showed two peaks at 400.3 and 404.3 eV at a ~2:1 ratio, in agreement with our previous results of azidated graphene and markedly different from the starting NaN_3.[101] Quantification of the XPS peak areas yielded an N:C ratio of 13.5% (Figure 63c), close to that is achieved through electrochemistry.[101] Interference reflection microscopy (IRM)[4,14] and Raman spectroscopy indicated little defect generation but enhanced doping after photocatalytic azidation (Figure 64), and electrical measurements showed enhanced conductivity consistent with enhanced doping (Figure 65). These results are also in line with what we previously observed with electrochemically azidated graphene.[101] As additional controls, we further examined samples that underwent the same illuminations in solutions without ammonium persulfate or $[Ru(bpy)_3]Cl_2$, and observed no

noticeable azidation (Figure 66). Together, these results indicate the successful photocatalytic azidation of graphene through our proposed pathway (Figure 62ab).

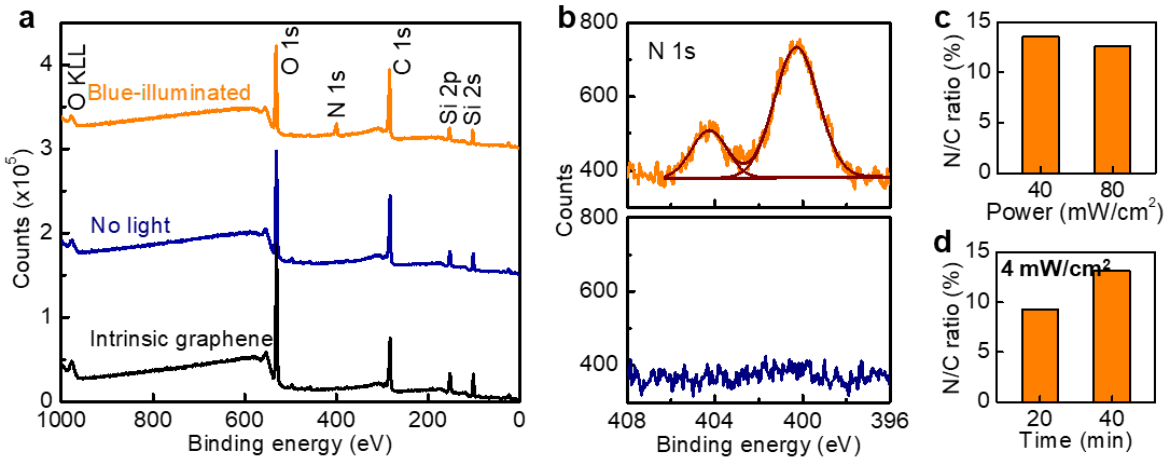

Figure 63. Effective photocatalytic azidation of graphene. (a) Survey-mode XPS results of monolayer graphene on glass substrates, before (back curve) and after (orange curve) 15 min of 40 mW/cm^2 blue-light illumination in the reactant solution, versus a control sample immersed in the same reactant for 15 min without illumination (blue curve). (b) High-resolution nitrogen 1s XPS for the illuminated and control samples. (c,d) The XPS-determined N:C atomic ratios for two samples illuminated for 15 min at 40 and 80 mW/cm^2 (c), and for two other samples illuminated at 4 mW/cm^2 for 20 and 40 min (d), respectively.

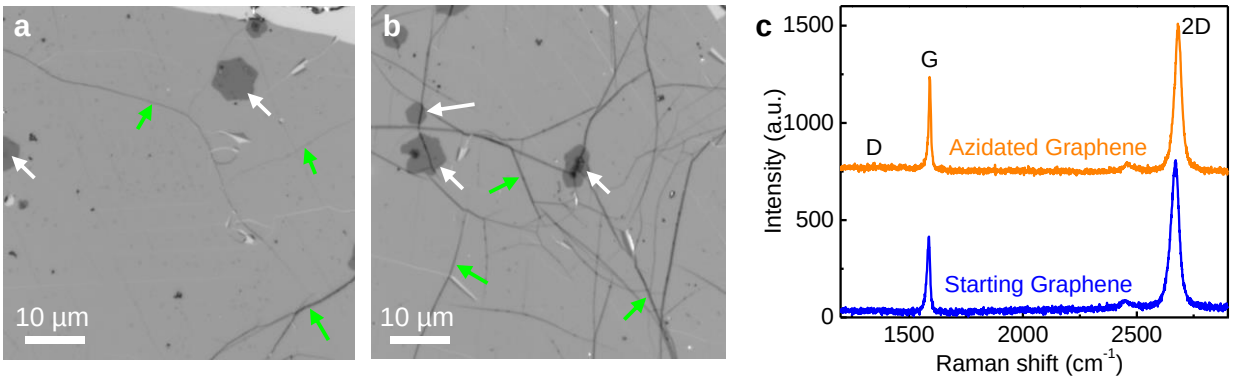

Figure 64. IRM and Raman spectroscopy results. (a,b) IRM images of monolayer CVD graphene samples, as prepared (a) and after photocatalytic azidation (b). No noticeable change in IRM contrast is observed, suggesting no significant oxidation or defect generation. White and green arrows respectively point to occasionally observed bilayer islands and wrinkles in the monolayer graphene. (c) Raman spectroscopy of the two samples. The azidated graphene showed no noticeable increase in the D peak signal but a decrease in the intensity ratio of the 2D peak over the G peak, indicating little defect generation but enhanced doping after azidation.

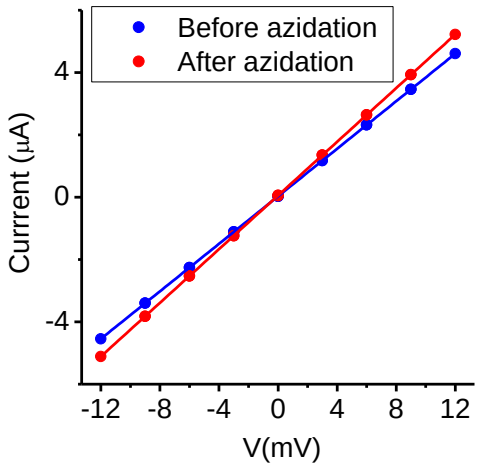

Figure 65. Electrical properties of a monolayer graphene strip before and after photocatalytic azidation. I-V curves were recorded with a Keithley 2400 SourceMeter. Linear fits yielded resistances of 2.62 and 2.33 kΩ before and after photocatalytic azidation, respectively, consistent with enhanced doping after the reaction.

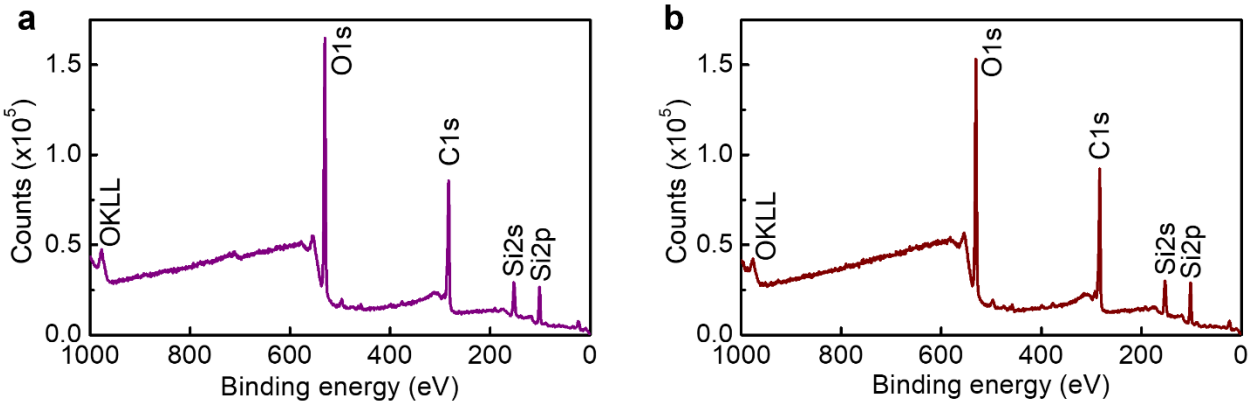

Figure 66. XPS results of additional control samples. (a) A monolayer graphene sample (on a glass substrate) that has gone through the same illumination at 40 mW/cm^2 for 15 min as the azidated sample in Figure 63a, but with $(NH_4)_2S_2O_8$ omitted in the reactant solution. (b) Another control sample after the same illumination, with the reactant solution further excluding $[Ru(bpy)_3]Cl_2$. No noticeable nitrogen peak was observed in either sample.

Reducing the power density to 4 mW/cm^2 still permitted reaction: although 20-min illumination now yielded a lower N:C ratio of 9%, this value increased to 13% when the reaction was extended to 40 min (Figure 63d). Conversely, increasing the illumination power to 80 mW/cm^2 did not further increase the N:C ratio of the product (Figure 63c). Instead, more vigorous bubble formation was noticed, suggesting that excessive azidyl radicals self-combined, analogous to what we observe in electrochemical azidation.[101]

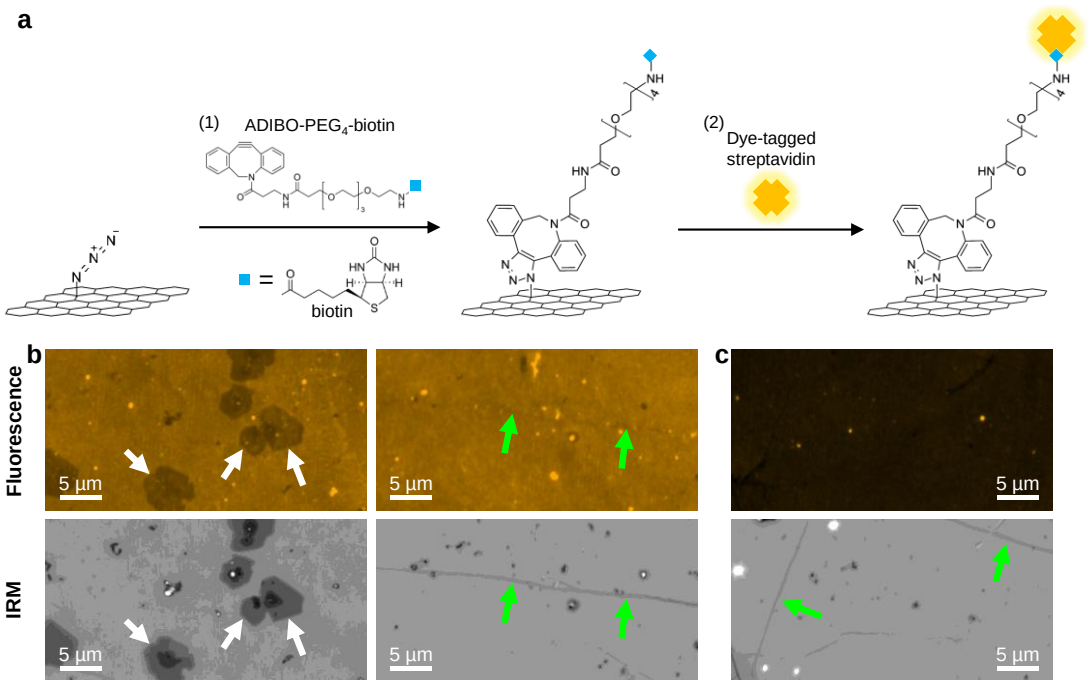

Figure 67. Click chemistry and bioconjugation of the photo-azidated graphene. (a) Schematics: (1) Copper-free cycloaddition with azadibenzocyclooctyne (ADIBO)-PEG4-biotin. (2) The functionalized biotin is next conjugated with fluorescently labeled streptavidin. (b) Fluorescence micrographs of the labeled streptavidin (top) and corresponding interference reflection microscopy (IRM)[4] images (bottom) of the final product. White and green arrows in (b) respectively point to occasionally observed bilayer islands and wrinkles in the monolayer graphene, where reduced fluorescence was observed. (c) Results on a control graphene sample that was not azidated but went through the same labeling process in (a). Green arrows point to wrinkles.

The azidated graphene next allowed click chemistry and biofunctionalization, *e.g.*, copper-free cycloaddition with azadibenzocyclooctyne-PEG4-biotin and subsequent conjugation with dye-labeled streptavidin (Figure 67a). Fluorescence micrographs (Figure 67b) showed spatially uniform functionalization across the graphene monolayer, with reduced signals at bilayer islands and wrinkles due to locally enhanced fluorescence quenching,[128] consistent with our previous results with electrochemically azidated graphene.[101] The N:C ratio of 13.5% we achieved in azidation suggests an azide (and hence biotin) functional group per ~0.6 nm^2 area of the graphene surface, substantially smaller than the size of the streptavidin tetramer (~5×5 nm^2). The achievable labeling density is thus likely limited by the streptavidin size. In comparison, little fluorescence was observed for control graphene samples that were not azidated but went through the same labeling process (Figure 67c).

Our use of photoredox catalysis permitted reaction with visible light at low power levels. The ~10 mW/cm^2 light intensity, readily obtained by applying a color filter to a white lamp, is ~10^7 lower than typical approaches in which ~1 mW laser beams are focused into ~1 μm^2 spots (~1 $mW/\mu m^2$ = 10^5 W/cm^2) for visible-light-induced graphene photoreactions and patterning.[34,62,174,177-179] Although for the spontaneous polymerization of a diazonium at the graphene surface we have previously noted enhanced polymer deposition at a moderate ~0.5 W/cm^2 illumination,[53] here the

azidation reaction was not spontaneous without illumination (Figure 63ab) and was chemically defined toward the graphene surface.

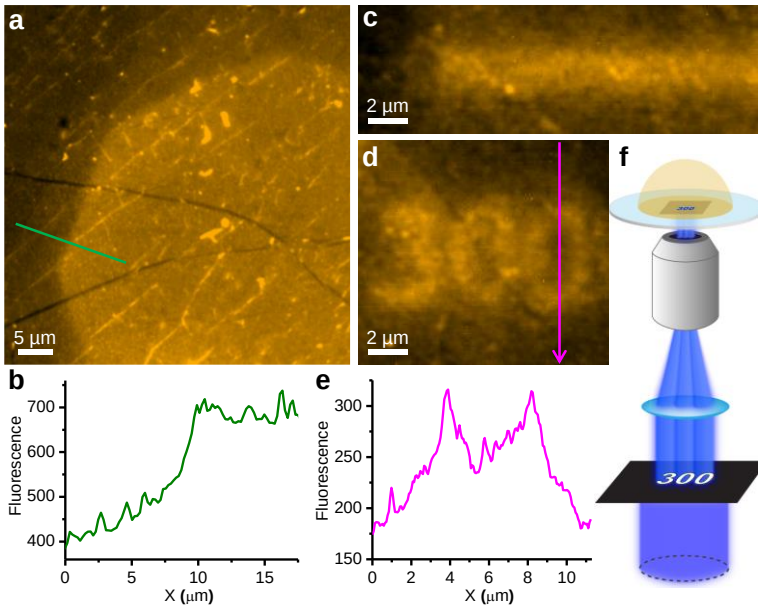

Figure 68. Chemical patterning of graphene functionalization *via* patterned illumination in the wide field. (a) Fluorescence micrograph of a sample after regional photocatalytic azidation and subsequent click chemistry and conjugation with dye-labeled streptavidin. Regional illumination was achieved with the field diaphragm of the microscope. (b) Fluorescence intensity profile along the green line in (a), crossing the boundary of the patterned azidation. (c,d) Patterning micrometer features as a straight line (c) and the text "300" (d). (e) Fluorescence intensity profile along the magenta arrow in (d). (f) Schematic: Defining desired illumination patterns in the wide field by inserting a printed photomask into the expanded illumination beam before the objective lens.

Taking advantage of the low visible light condition of our reaction, we next achieved direct patterning of graphene functionalization through patterned illumination in the wide field, which removes the need for scanning a focused laser beam to achieve high local light intensity in previous photopatterning approaches.[174,177-179] For an initial demonstration, using a 100x objective lens, we illuminated a confined region of the graphene sample in the above reactant, and then fluorescently labeled the sample through click chemistry and biotin-streptavidin conjugation. Fluorescence microscopy showed a distinct polygon pattern of functionalization (Figure 68a), consistent with the field diaphragm of the microscope that defined the illuminated region at the sample. Line profiles across the polygon boundary showed exponentially decaying signals over a few micrometers (Figure 68b), attributable to limited diffusion of the locally generated azidyl radicals.

For finer patterns of specific shapes, we inserted a printed photomask into the expanded illumination beam path of a home-built wide-field microscope, thus projecting predefined illumination patterns to the sample at a 200-fold size reduction (Figure 68f, Materials and methods). The resultant photopatterned azidation thus successfully defined line and text patterns with micrometer-sized features (Figure 68c-e).

6.3 Conclusion

Together, we have demonstrated a powerful yet facile approach for the photocatalytic azidation of graphene. The use of photoredox catalysis enabled efficient azidation with visible light at low power levels: We thus readily achieved azidation with blue light filtered from a white lamp, as well as photopatterning in the wide field without having to focus an intense laser beam into a tight spot. The resultant azidated graphene further enabled chemically defined derivations through click chemistry and subsequent bioconjugation. The examination of alternative photosensitizers and the possible generalization of our approach to other radical reactions for graphene and other surface and nanomaterials systems represent exciting future directions.

6.4 Materials and methods

Photocatalytic azidation of graphene. Monolayer graphene grown on copper foils[42] (ACS Material or Graphene Supermarket) was wet-transferred through a modified RCA cleaning process[100] onto #1.5 glass coverslips as ~5×10 mm pieces. The sample was mounted on a standard inverted wide-field epifluorescence microscope (Olympus IX73). 0.1 mM $[Ru(bpy)_3]Cl_2$ (Sigma 224758), 200 mM ammonium persulfate (Alfa Aesar 54106), and 200 mM NaN_3 (Sigma 71289) were dissolved in a 15 mM pH = 7 phosphate buffer. An ~100 µL drop of this solution was cast on the graphene surface. A standard filter cube on the Olympus IX73 microscope selected blue light from a white lamp (Olympus U-HGLGPS) and introduced it into the objective lens to illuminate a wide field of the sample. The filter cube was commonly used for the fluorescence imaging of Green Fluorescent Protein (GFP). With an excitation filter of ET470/40x (Chroma) and a dichroic mirror of T495lpxr (Chroma), the select-passed wavelength range was ~450-490 nm. When a low-magnification UPlanFL N 4x objective lens was used, a sample area of ~3 mm diameter was evenly illuminated. When a UplanFl 100× oil-immersion objective lens was used, a sample area of ~50 µm diameter was evenly illuminated, with the actual illumination region defined by the adjustable field diaphragm of the microscope. The total illumination power was measured using a photodiode power sensor (S120VC, Thorlabs). By controlling the output level of the U-HGLGPS lamp source (3-25%) and using additional neutral-density filters (Thorlabs), the typical illumination power density at the sample was set to ~10 mW/cm^2 (~0.1 $nW/\mu m^2$), as discussed in the main text. After the reaction, the sample was rinsed with 18 MΩ Milli-Q water and dried in air.

XPS characterization. XPS was performed using a Perkin Elmer PHI 5600 XPS that operated at ~10^{-9} torr with a monochromatic Al Kα (1486.8 eV) X-ray source. A neutralizer was used to discharge accumulated charges from the sample surface. Element compositions were determined from the peak areas using the factory-calibrated relative sensitivity factors.

Cycloaddition and subsequent biotin-streptavidin conjugation of azidated graphene. 0.02 mg ADIBO-PEG_4-biotin (Sigma-Aldrich 760749) was dissolved in 500 µL of 0.1 M potassium phosphate buffer (pH = 7). This solution reacted with both the azidated and control graphene samples in the dark for 1 h. The sample was rinsed with a 0.1 M potassium phosphate buffer three times, and then treated with 3% bovine serum albumin (BSA; Sigma-Aldrich A3059) in Dulbecco's phosphate-buffered saline (DPBS; Corning 21-031-cv) for 30 min. Alexa Fluor 555-conjugated streptavidin (Invitrogen S21381) was constituted as a 2 mg/mL stock solution in DPBS.

2 μL of this solution was added to 400 μL of DPBS containing 3% BSA, and the mixed solution was dropped onto the graphene sample. After 1 h of incubation in the dark, the sample was rinsed with DPBS 3 times, and then rinsed with Milli-Q water and dried in air.

Optical microscopy characterizations. Fluorescence microscopy and interference reflection microscopy (IRM)[4] were performed on an Olympus IX73 inverted epifluorescence microscope using an Olympus UplanFl 100× oil-immersion objective (numerical aperture ~0.9 with iris diaphragm). For fluorescence microscopy of the labeled Alexa Fluor 555-conjugated streptavidin, the excitation filter, dichroic mirror, and emission filter were ET545/25x, zt561rdc-UF1, and ET605/70m, respectively (Chroma). For IRM, the excitation filter was D532/10x (Chroma), the dichroic mirror position was a 50/50 beam splitter (Chroma 21000), and the emission filter position was left empty.

Chemical patterning through patterned illumination in the wide field. The graphene sample on the glass coverslip was mounted on a homebuilt super-resolution microscopy system based on a Nikon Eclipse Ti-E inverted fluorescence microscope.[63] The illumination source was a 488 nm laser (Coherent Sapphire), which was first passed through an acousto-optic tunable fiber (Gooch & Housego, 97-03151-01) for controlling the illumination power before being coupled into a single-mode optical fiber. Output from the fiber was expanded into a collimated beam ~20 mm in diameter and focused to the back focal plane of the objective lens (Nikon CFI Plan Apochromat λ 100×) using a lens of 40 cm focal length (2x of the tube-lens focal length), thus evenly illuminating a wide field ~100 μm in diameter. A printed photomask (Outputcity) was placed at the expanded collimated beam that entered the microscope, so that the printed patterns were projected to the sample plane at a 200-fold size reduction. The same photocatalytic reactant solution as above was cast on the graphene surface, and the patterned illumination was applied for 15 min at a power density of ~100 mW/cm^2 (~1 nW/μm^2) for the lower absorbance of $[Ru(bpy)_3]Cl_2$ at 488 nm.

Conclusions and outlook

The work described in this dissertation is unified under high resolution optical techniques and chemical modifications of graphene.

In part I of this dissertation, we demonstrate the direct optical visualization of *in situ* dynamics of graphene chemistry through interference reflection microscopy. With the outstanding contrast and *in situ* imaging capabilities offered by IRM, we discovered spatially resolved, *in situ* dynamics of a redox reaction, diazonium reaction and solution-enclosing blister generation process of substrate-supported graphene at high spatiotemporal resolution.

In part II of this dissertation, we move to focus on facile chemical modifications of graphene under ambient conditions. Optical characterization techniques including interference reflection microscopy, transmission microscopy, fluorescence microscopy, and Raman spectroscopy are utilized here to help establish the successful modifications of graphene. Our work on graphene azidation and chlorination not only offers facile, accessible paths for the covalent modifications of graphene, but also elucidates valuable radical-mediated mechanisms for the functionalization of graphene and related nanomaterials.

As a concluding remark of this thesis, I would like to briefly introduce our ongoing efforts on the electropolymerization of pyrrole[189-192] on graphene using interference reflection microscopy.

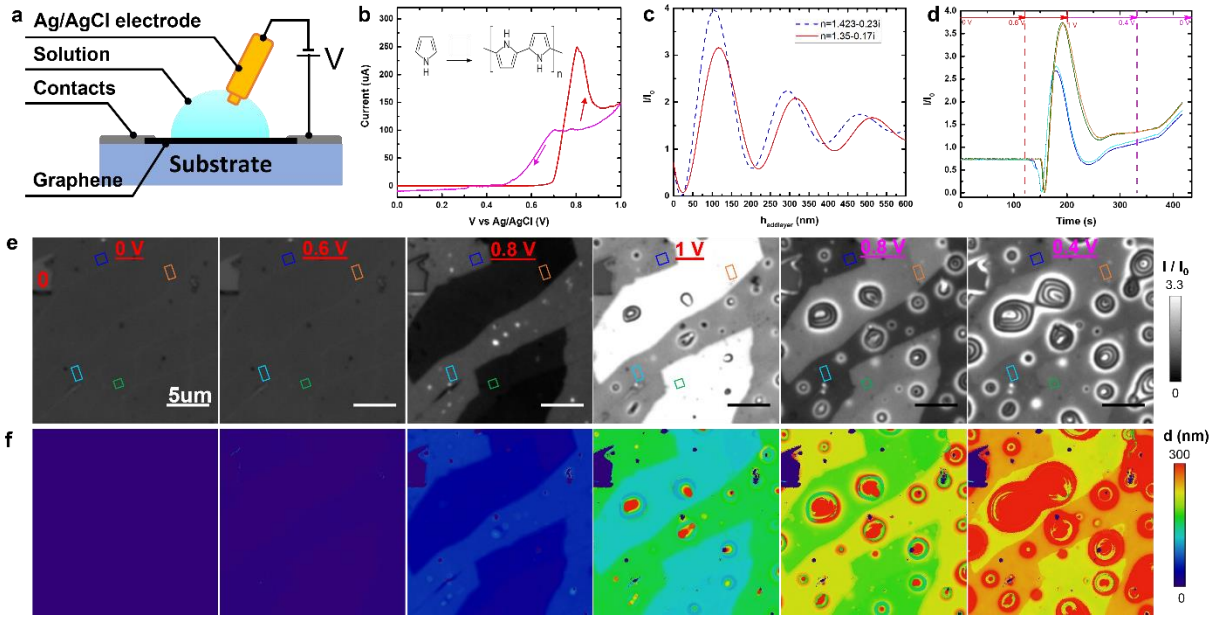

Figure 69. IRM unveils rich spatial heterogeneity of the electropolymerization process of pyrrole on graphene. (a) Schematic of the system. (b) Measured electrochemical current vs. a scanned voltage (5 mV/s) across monolayer graphene and a Ag/AgCl electrode, in 0.1 M pyrrole in 1M NaCl. (c) Predicted IRM signal (light intensity I normalized by the intensity at the bare substrate I_0) for monolayer graphene on glass, as a function of the local polymer height h, for two plausible values of complex index of refraction of the polymer. (d) IRM signal time traces for 4 representative regions in e. (e) Experimental *in situ* IRM images for the electropolymerization process of pyrrole on graphene on a glass substrate at different voltages vs. Ag/AgCl. "0" marks locally exposed glass surface. (e) Converted polymer height maps. Scale bar: 5um.

Figure 69a illustrates our electropolymerization scheme. CVD-grown monolayer graphene was deposited onto glass substrates and fabricated into a working electrode for electrochemistry by electrically contacting at both ends. A ~60 μL drop of 0.1 M pyrrole aqueous solution (in a 1 M NaCl solution) was added to the graphene sample, and the electrochemical cell was completed by inserting an Ag/AgCl (3 M NaCl) counter/reference electrode from the top. A Keithley 2401 SourceMeter provided an anodic voltage across the graphene sample and the Ag/AgCl electrode, which electrochemically oxidized pyrrole molecules in the solution at the graphene surface to generate polymers on graphene electrode. To gain control of the polymerization process, we scanned the voltage at 5 mV/s, and the detected electrochemical current rose rapidly beyond 0.6 V (vs. Ag/AgCl) (Figure 69b). We visualized an unexpected variation of polymer thickness on different graphene flakes in the polymerization process through IRM. Close examination of the IRM images before reaction (Figure 69e) indicated that these flakes were electrically isolated by nanoscale cracks. Similar to the diazonium reaction system in chapter 2, we argue that even though these flakes were fragmented from the same initial graphene sheet, they were possibly inadvertently doped to different levels on the glass surface,[10] and so shifted to different electrochemical potentials that affected the polymerization reactivity. Transfer-matrix analysis[4]

showed that the IRM readout, as presented as local light intensity I divided by the intensity at a direct substrate-solution interface I_0 (I/I_0), would initially drop from ~0.72 to ~0 as the polymer height increases to ~25 nm (Figure 69b). Subsequently, the signal would rapidly rise as the polymer height were increased to ~105 nm, when the signal would drop again with further blister growth (Figure 69b). As we examined the IRM signal time traces of different regions on the graphene sample (Figure 69c), we observed trends consistent with the above features. By following the time traces and comparing them with our prediction in Figure 69b, we converted the IRM data into local height maps of the polypyrrole polymers (Figure 69f). This showed that the polypyrrole first grew as a uniform layer under smaller electrochemical current, and then formed some local clusters as the current increased. After integrating the red portion of the current-time curve in Figure 69b, we estimated a coulombic efficiency of ~69% after the first half of cyclic voltammetry cycle, which is comparable to the polymerization efficiency estimated by Rajeshwar et al[193] for a similar system.

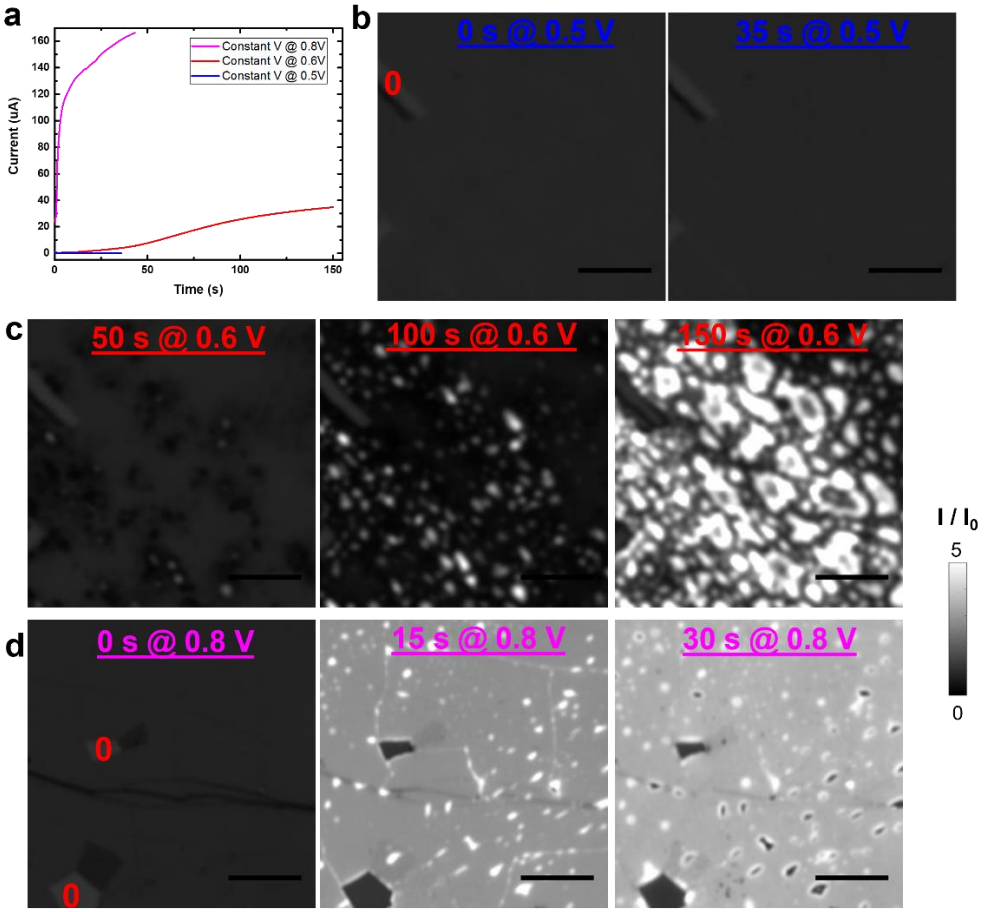

Figure 70. Electropolymerization process of pyrrole on graphene at different voltages. (a) Time-dependent electrochemical current in 0.1 M pyrrole in 1M NaCl, at fixed voltages of 0.8, 0.6, and 0.5 V (vs. Ag/AgCl), respectively. (b) *In situ* IRM images for the electropolymerization process of pyrrole on a graphene sample on a glass substrate, before (left) and after 35 s of voltage application at 0.5 V (vs. Ag/AgCl) in 0.1 M pyrrole in 1M NaCl. (c) *In situ* IRM images for the same sample in b with the application of a voltage of 0.6 V (vs. Ag/AgCl) for 50 s (left), 100 s (center) and 150 s (right). (d) *In situ* IRM images for the electropolymerization process of pyrrole on a different graphene sample on a glass substrate with the application of a voltage of 0.8 V (vs.

Ag/AgCl) for 0 s (left), 15 s (center) and 30 s (right) in 0.1 M pyrrole in 1M NaCl. “0” marks locally exposed glass surface. Scale bar: 5um.

To better understand the electropolymerization process, we examined it at different fixed voltages. Whereas no appreciable polymerization occurred at 0.5 V vs. Ag/AgCl (Figure 70b), under which condition the electrochemical current was negligible (Figure 70a). Substantial polymerization was found at 0.6 V (Figure 70c), for which case the electrochemical current was significant (Figure 70a). Stronger electrochemical current was observed at 0.8 V (Figure 70a). Interestingly, polypyrrole grew to local clusters at 0.6V with smaller electrochemical current (Figure 70c) and grew to a uniform layer at 0.8V with higher electrochemical current (Figure 70d). We next investigated the electropolymerization process of pyrrole on ITO and found that the electropolymerization process was slower compared to that on graphene substrate (Figure 71). At a higher voltage for a longer time, polypyrrole still grew into local clusters rather as a uniform layer, which was possibly due to a lower affinity of polypyrrole and ITO[194,195].

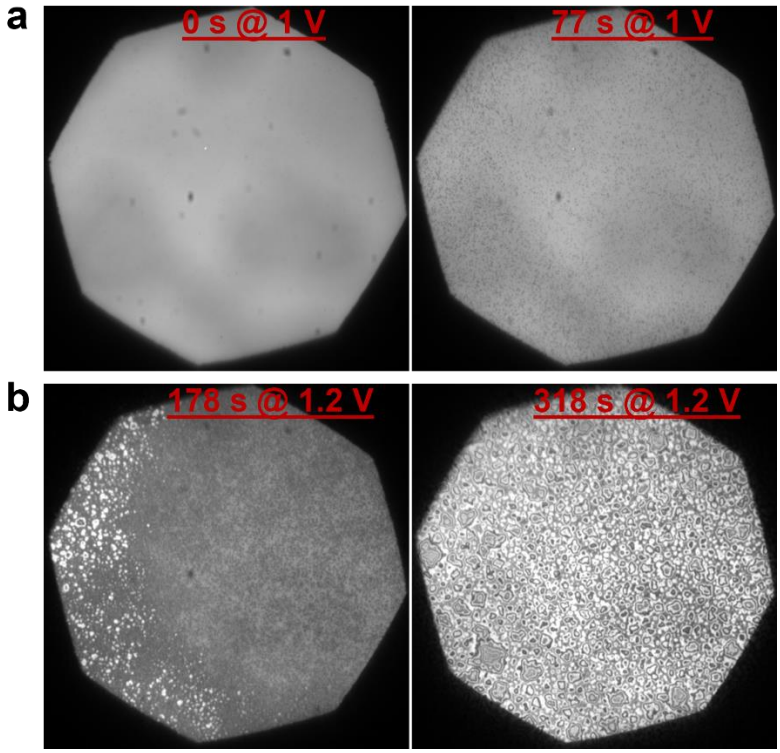

Figure 71. Electropolymerization process of pyrrole on ITO substrate. (a) *In situ* IRM images for the electropolymerization process of pyrrole on an ITO substrate, before (left) and after 77 s of voltage application at 1 V (vs. Ag wire) in 0.1 M pyrrole in 1M NaCl. (b) *In situ* IRM images for the same sample in a with the application of a voltage of 1.2 V (vs. Ag wire) for 178 s (left) and 318 s (right).

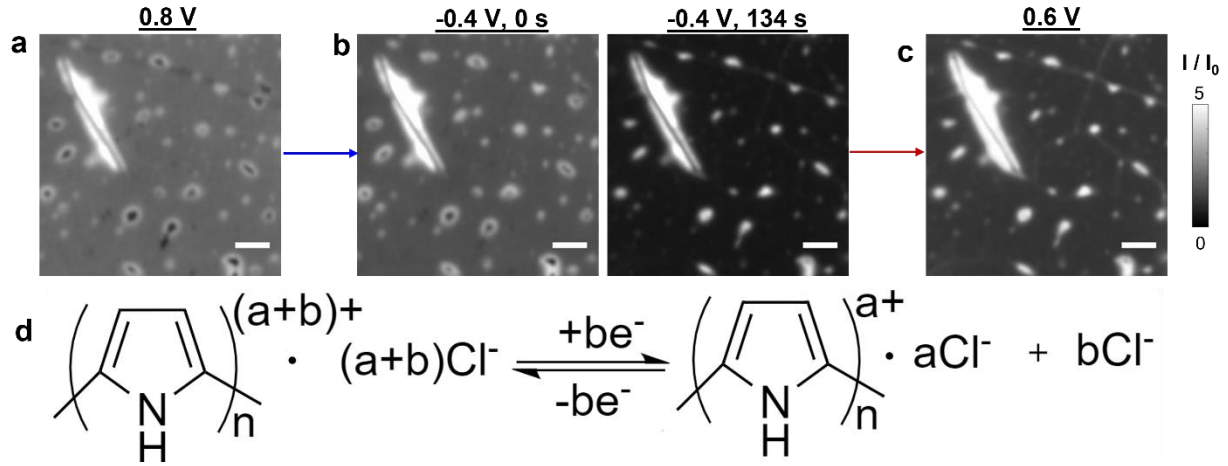

Figure 72. Reversible fast reduction and oxidation of polypyrrole *via* voltage jumping. (a) The IRM image of polypyrrole at oxidative voltage of 0.8 V (vs. Ag/AgCl) (b) The voltage was changed to -0.4 V (vs. Ag/AgCl), and IRM recorded a fast decrease of the polymer signal. (c) The voltage was next changed to 0.6 V (vs. Ag/AgCl), and IRM recorded a fast recovery of the polymer signal. (d) Reaction schemes of the reduction and oxidation of polypyrrole. Scale bars: 2 μm.

We further examined the reduction behavior[196,197] of the grown polypyrrole material (Figure 72). Interestingly, upon reductive voltage, the IRM signal of polypyrrole decreased. As we switched to an oxidative voltage, the IRM signal of polypyrrole quickly jumped back. These results indicated reversible fast reduction and oxidation modulation of polypyrrole material.

Together, these work in this dissertation sheds new light on graphene properties, both in terms of its unique dynamics in different chemical processes and its facile, accessible chemical modification pathways. These developments carry practical implications for understanding the potentials of graphene applications.

References

(1) Curtis, A. S. G. The mechanism of adhesion of cells to glass: A study by interference reflection microscopy. *J. Cell Biol.* **1964**, *20*, 199-215.
(2) Verschueren, H. Interference reflection microscopy in cell biology: Methodology and applications. *J. Cell Sci.* **1985**, *75*, 279-301.
(3) Limozin, L.; Sengupta, K. Quantitative reflection interference contrast microscopy (RICM) in soft matter and cell adhesion. *ChemPhysChem* **2009**, *10*, 2752-2768.
(4) Li, W.; Moon, S.; Wojcik, M.; Xu, K. Direct optical visualization of graphene and its nanoscale defects on transparent substrates. *Nano Lett.* **2016**, *16*, 5027-5031.
(5) Lomeda, J. R.; Doyle, C. D.; Kosynkin, D. V.; Hwang, W. F.; Tour, J. M. Diazonium functionalization of surfactant-wrapped chemically converted graphene sheets. *J. Am. Chem. Soc.* **2008**, *130*, 16201-16206.
(6) Bekyarova, E.; Itkis, M. E.; Ramesh, P.; Berger, C.; Sprinkle, M.; de Heer, W. A.; Haddon, R. C. Chemical modification of epitaxial graphene: spontaneous grafting of aryl groups. *J. Am. Chem. Soc.* **2009**, *131*, 1336-1337.
(7) Hossain, M. Z.; Walsh, M. A.; Hersam, M. C. Scanning Tunneling Microscopy, Spectroscopy, and Nanolithography of Epitaxial Graphene Chemically Modified with Aryl Moieties. *J. Am. Chem. Soc.* **2010**, *132*, 15399-15403.

(8) Koehler, F. M.; Jacobsen, A.; Ensslin, K.; Stampfer, C.; Stark, W. J. Selective chemical modification of graphene surfaces: distinction between single- and bilayer graphene. *Small* **2010**, *6*, 1125-1130.
(9) Sharma, R.; Baik, J. H.; Perera, C. J.; Strano, M. S. Anomalously large reactivity of single graphene layers and edges toward electron transfer chemistries. *Nano Lett.* **2010**, *10*, 398-405.
(10) Wang, Q. H.; Jin, Z.; Kim, K. K.; Hilmer, A. J.; Paulus, G. L. C.; Shih, C. J.; Ham, M. H.; Sanchez-Yamagishi, J. D.; Watanabe, K.; Taniguchi, T. *et al.* Understanding and controlling the substrate effect on graphene electron-transfer chemistry via reactivity imprint lithography. *Nat. Chem.* **2012**, *4*, 724-732.
(11) Paulus, G. L. C.; Wang, Q. H.; Strano, M. S. Covalent electron transfer chemistry of graphene with diazonium salts. *Acc. Chem. Res.* **2013**, *46*, 160-170.
(12) Greenwood, J.; Phan, T. H.; Fujita, Y.; Li, Z.; Ivasenko, O.; Vanderlinden, W.; Van Gorp, H.; Frederickx, W.; Lu, G.; Tahara, K. *et al.* Covalent modification of graphene and graphite using diazonium chemistry: tunable grafting and nanomanipulation. *ACS Nano* **2015**, *9*, 5520-35.
(13) Niyogi, S.; Bekyarova, E.; Itkis, M. E.; Zhang, H.; Shepperd, K.; Hicks, J.; Sprinkle, M.; Berger, C.; Lau, C. N.; deHeer, W. A. *et al.* Spectroscopy of covalently functionalized graphene. *Nano Lett.* **2010**, *10*, 4061-4066.
(14) Wojcik, M.; Li, Y.; Li, W.; Xu, K. Spatially resolved *in situ* reaction dynamics of graphene via optical microscopy. *J. Am. Chem. Soc.* **2017**, *139*, 5836-5841.
(15) Li, W.; Wojcik, M.; Xu, K. Optical microscopy unveils rapid, reversible electrochemical oxidation and reduction of graphene. *Nano Lett.* **2019**, *19*, 983-989.
(16) Geim, A. K.; Novoselov, K. S. The rise of graphene. *Nature Mater.* **2007**, *6*, 183-191.
(17) Novoselov, K. S.; Fal'ko, V. I.; Colombo, L.; Gellert, P. R.; Schwab, M. G.; Kim, K. A roadmap for graphene. *Nature* **2012**, *490*, 192-200.
(18) Dreyer, D. R.; Park, S.; Bielawski, C. W.; Ruoff, R. S. The chemistry of graphene oxide. *Chem. Soc. Rev.* **2010**, *39*, 228-240.
(19) Bekyarova, E.; Sarkar, S.; Niyogi, S.; Itkis, M. E.; Haddon, R. C. Advances in the chemical modification of epitaxial graphene. *J. Phys. D-Appl. Phys.* **2012**, *45*, 154009.
(20) Georgakilas, V.; Otyepka, M.; Bourlinos, A. B.; Chandra, V.; Kim, N.; Kemp, K. C.; Hobza, P.; Zboril, R.; Kim, K. S. Functionalization of graphene: covalent and non-covalent approaches, derivatives and applications. *Chem. Rev.* **2012**, *112*, 6156-6214.
(21) Yan, L.; Zheng, Y. B.; Zhao, F.; Li, S. J.; Gao, X. F.; Xu, B. Q.; Weiss, P. S.; Zhao, Y. L. Chemistry and physics of a single atomic layer: strategies and challenges for functionalization of graphene and graphene-based materials. *Chem. Soc. Rev.* **2012**, *41*, 97-114.
(22) Chua, C. K.; Pumera, M. Covalent chemistry on graphene. *Chem. Soc. Rev.* **2013**, *42*, 3222-3233.
(23) Eigler, S.; Hirsch, A. Chemistry with graphene and graphene oxide-challenges for synthetic chemists. *Angew. Chem.-Int. Edit.* **2014**, *53*, 7720-7738.
(24) Criado, A.; Melchionna, M.; Marchesan, S.; Prato, M. The covalent functionalization of graphene on substrates. *Angew. Chem.-Int. Edit.* **2015**, *54*, 10734-10750.
(25) Dreyer, D. R.; Todd, A. D.; Bielawski, C. W. Harnessing the chemistry of graphene oxide. *Chem. Soc. Rev.* **2014**, *43*, 5288-5301.
(26) Pei, S. F.; Cheng, H. M. The reduction of graphene oxide. *Carbon* **2012**, *50*, 3210-3228.

(27) Chua, C. K.; Pumera, M. Chemical reduction of graphene oxide: a synthetic chemistry viewpoint. *Chem. Soc. Rev.* **2014**, *43*, 291-312.
(28) Stankovich, S.; Dikin, D. A.; Piner, R. D.; Kohlhaas, K. A.; Kleinhammes, A.; Jia, Y.; Wu, Y.; Nguyen, S. T.; Ruoff, R. S. Synthesis of graphene-based nanosheets via chemical reduction of exfoliated graphite oxide. *Carbon* **2007**, *45*, 1558-1565.
(29) Yang, D.; Velamakanni, A.; Bozoklu, G.; Park, S.; Stoller, M.; Piner, R. D.; Stankovich, S.; Jung, I.; Field, D. A.; Ventrice, C. A. *et al.* Chemical analysis of graphene oxide films after heat and chemical treatments by X-ray photoelectron and Micro-Raman spectroscopy. *Carbon* **2009**, *47*, 145-152.
(30) Yuan, J. T.; Ma, L. P.; Pei, S. F.; Du, J. H.; Su, Y.; Ren, W. C.; Cheng, H. M. Tuning the Electrical and Optical Properties of Graphene by Ozone Treatment for Patterning Monolithic Transparent Electrodes. *ACS Nano* **2013**, *7*, 4233-4241.
(31) Ferrari, A. C.; Basko, D. M. Raman spectroscopy as a versatile tool for studying the properties of graphene. *Nat. Nanotechnol.* **2013**, *8*, 235-246.
(32) Liu, L.; Ryu, S. M.; Tomasik, M. R.; Stolyarova, E.; Jung, N.; Hybertsen, M. S.; Steigerwald, M. L.; Brus, L. E.; Flynn, G. W. Graphene oxidation: Thickness-dependent etching and strong chemical doping. *Nano Lett.* **2008**, *8*, 1965-1970.
(33) Ryu, S.; Han, M. Y.; Maultzsch, J.; Heinz, T. F.; Kim, P.; Steigerwald, M. L.; Brus, L. E. Reversible basal plane hydrogenation of graphene. *Nano Lett.* **2008**, *8*, 4597-4602.
(34) Liu, H. T.; Ryu, S. M.; Chen, Z. Y.; Steigerwald, M. L.; Nuckolls, C.; Brus, L. E. Photochemical reactivity of graphene. *J. Am. Chem. Soc.* **2009**, *131*, 17099-17101.
(35) Surwade, S. P.; Li, Z. T.; Liu, H. T. Thermal oxidation and unwrinkling of chemical vapor deposition-grown graphene. *J. Phys. Chem. C* **2012**, *116*, 20600-20606.
(36) Tan, C.; Rodriguez-Lopez, J.; Parks, J. J.; Ritzert, N. L.; Ralph, D. C.; Abruna, H. D. Reactivity of monolayer chemical vapor deposited graphene imperfections studied using scanning electrochemical microscopy. *ACS Nano* **2012**, *6*, 3070-3079.
(37) Zhong, J. H.; Zhang, J.; Jin, X.; Liu, J. Y.; Li, Q. Y.; Li, M. H.; Cai, W. W.; Wu, D. Y.; Zhan, D. P.; Ren, B. Quantitative correlation between defect density and heterogeneous electron transfer rate of single layer graphene. *J. Am. Chem. Soc.* **2014**, *136*, 16609-16617.
(38) Guell, A. G.; Cuharuc, A. S.; Kim, Y. R.; Zhang, G. H.; Tan, S. Y.; Ebejer, N.; Unwin, P. R. Redox-dependent spatially resolved electrochemistry at graphene and graphite step edges. *ACS Nano* **2015**, *9*, 3558-3571.
(39) Blake, P.; Hill, E. W.; Neto, A. H. C.; Novoselov, K. S.; Jiang, D.; Yang, R.; Booth, T. J.; Geim, A. K. Making graphene visible. *Appl. Phys. Lett.* **2007**, *91*, 063124.
(40) Cheon, S.; Kihm, K. D.; Kim, H. G.; Lim, G.; Park, J. S.; Lee, J. S. How to reliably determine the complex refractive index (RI) of graphene by using two independent measurement constraints. *Sci. Rep.* **2014**, *4*, 6364.
(41) Jung, I.; Vaupel, M.; Pelton, M.; Piner, R.; Dikin, D. A.; Stankovich, S.; An, J.; Ruoff, R. S. Characterization of thermally reduced graphene oxide by imaging ellipsometry. *J. Phys. Chem. C* **2008**, *112*, 8499-8506.
(42) Li, X. S.; Cai, W. W.; An, J. H.; Kim, S.; Nah, J.; Yang, D. X.; Piner, R.; Velamakanni, A.; Jung, I.; Tutuc, E. *et al.* Large-area synthesis of high-quality and uniform graphene films on copper foils. *Science* **2009**, *324*, 1312-1314.
(43) Reina, A.; Son, H.; Jiao, L.; Fan, B.; Dresselhaus, M. S.; Liu, Z.; Kong, J. Transferring and identification of single- and few-layer graphene on arbitrary substrates. *J. Phys. Chem. C* **2008**, *112*, 17741-17744.

(44) Nair, R. R.; Blake, P.; Grigorenko, A. N.; Novoselov, K. S.; Booth, T. J.; Stauber, T.; Peres, N. M. R.; Geim, A. K. Fine structure constant defines visual transparency of graphene. *Science* **2008**, *320*, 1308.
(45) Kim, J.; Kim, F.; Huang, J. X. Seeing graphene-based sheets. *Mater. Today* **2010**, *13(3)*, 28-38.
(46) Kyle, J. R.; Ozkan, C. S.; Ozkan, M. Industrial graphene metrology. *Nanoscale* **2012**, *4*, 3807-3819.
(47) Banhart, F.; Kotakoski, J.; Krasheninnikov, A. V. Structural Defects in Graphene. *ACS Nano* **2011**, *5*, 26-41.
(48) Mikhailov, A. S.; Showalter, K. Control of waves, patterns and turbulence in chemical systems. *Phys. Rep.-Rev. Sec. Phys. Lett.* **2006**, *425*, 79-194.
(49) Hummers, W. S.; Offeman, R. E. Preparation of graphitic oxide. *J. Am. Chem. Soc.* **1958**, *80*, 1339-1339.
(50) Fernandez-Merino, M. J.; Guardia, L.; Paredes, J. I.; Villar-Rodil, S.; Solis-Fernandez, P.; Martinez-Alonso, A.; Tascon, J. M. D. Vitamin C is an ideal substitute for hydrazine in the reduction of graphene oxide suspensions. *J. Phys. Chem. C* **2010**, *114*, 6426-6432.
(51) Zhou, T. N.; Chen, F.; Liu, K.; Deng, H.; Zhang, Q.; Feng, J. W.; Fu, Q. A. A simple and efficient method to prepare graphene by reduction of graphite oxide with sodium hydrosulfite. *Nanotechnology* **2011**, *22*, 045704.
(52) Fan, X. B.; Peng, W. C.; Li, Y.; Li, X. Y.; Wang, S. L.; Zhang, G. L.; Zhang, F. B. Deoxygenation of exfoliated graphite oxide under alkaline conditions: a green route to graphene preparation. *Adv. Mater.* **2008**, *20*, 4490-4493.
(53) Li, Y.; Li, W.; Wojcik, M.; Wang, B.; Lin, L.-C.; Raschke, M. B.; Xu, K. Light-assisted diazonium functionalization of graphene and spatial heterogeneities in reactivity. *J. Phys. Chem. Lett.* **2019**, *10*, 4788-4793.
(54) Kaplan, A.; Yuan, Z.; Benck, J. D.; Rajan, A. G.; Chu, X. S.; Wang, Q. H.; Strano, M. S. Current and future directions in electron transfer chemistry of graphene. *Chem. Soc. Rev.* **2017**, *46*, 4530-4571.
(55) Lim, H.; Lee, J. S.; Shin, H. J.; Shin, H. S.; Choi, H. C. Spatially resolved spontaneous reactivity of diazonium salt on edge and basal plane of graphene without surfactant and its doping effect. *Langmuir* **2010**, *26*, 12278-12284.
(56) Pinson, J.; Podvorica, F. Attachment of organic layers to conductive or semiconductive surfaces by reduction of diazonium salts. *Chem. Soc. Rev.* **2005**, *34*, 429-439.
(57) Atkin, J. M.; Berweger, S.; Jones, A. C.; Raschke, M. B. Nano-optical imaging and spectroscopy of order, phases, and domains in complex solids. *Adv. Phys.* **2012**, *61*, 745-842.
(58) Liu, H.; Ryu, S.; Chen, Z.; Steigerwald, M. L.; Nuckolls, C.; Brus, L. E. Photochemical Reactivity of Graphene. *J. Am. Chem. Soc.* **2009**, *131*, 17099-17101.
(59) Li, B.; Zhou, L.; Wu, D.; Peng, H. L.; Yan, K.; Zhou, Y.; Liu, Z. F. Photochemical chlorination of graphene. *ACS Nano* **2011**, *5*, 5957-5961.
(60) Zhang, L.; Zhou, L.; Yang, M.; Liu, Z.; Xie, Q.; Peng, H.; Liu, Z. Photo-induced free radical modification of graphene. *Small* **2013**, *9*, 1134-1143.
(61) Liao, L.; Song, Z. H.; Zhou, Y.; Wang, H.; Xie, Q.; Peng, H. L.; Liu, Z. F. Photoinduced methylation of graphene. *Small* **2013**, *9*, 1348-1352.
(62) Liao, L.; Wang, H.; Peng, H.; Yin, J. B.; Koh, A. L.; Chen, Y. L.; Xie, Q.; Peng, H. L.; Liu, Z. F. van Hove singularity enhanced photochemical reactivity of twisted bilayer graphene. *Nano Lett.* **2015**, *15*, 5585-5589.

(63) Wojcik, M.; Hauser, M.; Li, W.; Moon, S.; Xu, K. Graphene-enabled electron microscopy and correlated super-resolution microscopy of wet cells. *Nat. Commun.* **2015**, *6*, 7384.
(64) Horcas, I.; Fernandez, R.; Gomez-Rodriguez, J. M.; Colchero, J.; Gomez-Herrero, J.; Baro, A. M. WSXM: A software for scanning probe microscopy and a tool for nanotechnology. *Rev. Sci. Instrum.* **2007**, *78*, 013705.
(65) Li, Y.; Wang, B.; Li, W.; Xu, K. Dynamic, spontaneous blistering of substrate-supported graphene in acidic solutions. *ACS Nano* **2022**, *16*, 6145-6152.
(66) Papageorgiou, D. G.; Kinloch, I. A.; Young, R. J. Mechanical properties of graphene and graphene-based nanocomposites. *Prog. Mater. Sci.* **2017**, *90*, 75-127.
(67) Dai, Z.; Liu, L.; Zhang, Z. Strain Engineering of 2D Materials: Issues and Opportunities at the Interface. *Adv. Mater.* **2019**, *31*, 1805417.
(68) Sun, Y. W.; Papageorgiou, D. G.; Humphreys, C. J.; Dunstan, D. J.; Puech, P.; Proctor, J. E.; Bousige, C.; Machon, D.; San-Miguel, A. Mechanical properties of graphene. *Appl. Phys. Rev.* **2021**, *8*, 021310.
(69) Sanchez, D. A.; Dai, Z.; Lu, N. 2D Material Bubbles: Fabrication, Characterization, and Applications. *Trends Chem.* **2021**, *3*, 204-217.
(70) Bunch, J. S.; Verbridge, S. S.; Alden, J. S.; van der Zande, A. M.; Parpia, J. M.; Craighead, H. G.; McEuen, P. L. Impermeable Atomic Membranes from Graphene Sheets. *Nano Lett.* **2008**, *8*, 2458-2462.
(71) Stolyarova, E.; Stolyarov, D.; Bolotin, K.; Ryu, S.; Liu, L.; Rim, K. T.; Klima, M.; Hybertsen, M.; Pogorelsky, I.; Pavlishin, I. *et al.* Observation of Graphene Bubbles and Effective Mass Transport under Graphene Films. *Nano Lett.* **2009**, *9*, 332-337.
(72) Koenig, S. P.; Boddeti, N. G.; Dunn, M. L.; Bunch, J. S. Ultrastrong adhesion of graphene membranes. *Nat. Nanotechnol.* **2011**, *6*, 543-546.
(73) Koenig, S. P.; Wang, L.; Pellegrino, J.; Bunch, J. S. Selective molecular sieving through porous graphene. *Nat. Nanotechnol.* **2012**, *7*, 728-732.
(74) Boddeti, N. G.; Liu, X.; Long, R.; Xiao, J.; Bunch, J. S.; Dunn, M. L. Graphene blisters with switchable shapes controlled by pressure and adhesion. *Nano Lett.* **2013**, *13*, 6216-6221.
(75) Khestanova, E.; Guinea, F.; Fumagalli, L.; Geim, A. K.; Grigorieva, I. V. Universal shape and pressure inside bubbles appearing in van der Waals heterostructures. *Nat. Commun.* **2016**, *7*, 12587.
(76) Ghorbanfekr-Kalashami, H.; Vasu, K. S.; Nair, R. R.; Peeters, F. M.; Neek-Amal, M. Dependence of the shape of graphene nanobubbles on trapped substance. *Nat. Commun.* **2017**, *8*, 15844.
(77) Sanchez, D. A.; Dai, Z.; Wang, P.; Cantu-Chavez, A.; Brennan, C. J.; Huang, R.; Lu, N. Mechanics of spontaneously formed nanoblisters trapped by transferred 2D crystals. *Proc. Natl. Acad. Sci. U.S.A.* **2018**, *115*, 7884-7889.
(78) Dai, Z.; Hou, Y.; Sanchez, D. A.; Wang, G.; Brennan, C. J.; Zhang, Z.; Liu, L.; Lu, N. Interface-Governed Deformation of Nanobubbles and Nanotents Formed by Two-Dimensional Materials. *Phys. Rev. Lett.* **2018**, *121*, 266101.
(79) Xu, K.; Cao, P. G.; Heath, J. R. Graphene visualizes the first water adlayers on mica at ambient conditions. *Science* **2010**, *329*, 1188-1191.
(80) Lee, M. J.; Choi, J. S.; Kim, J.-S.; Byun, I.-S.; Lee, D. H.; Ryu, S.; Lee, C.; Park, B. H. Characteristics and Effects of Diffused Water Between Graphene and a SiO_2 Substrate. *Nano Res.* **2012**, *5*, 710-717.

(81) Kim, H. H.; Yang, J. W.; Jo, S. B.; Kang, B.; Lee, S. K.; Bong, H.; Lee, G.; Kim, K. S.; Cho, K. Substrate-Induced Solvent Intercalation for Stable Graphene Doping. *ACS Nano* **2013**, *7*, 1155-1162.
(82) Li, Q.; Song, J.; Besenbacher, F.; Dong, M. Two-dimensional material confined water. *Acc. Chem. Res.* **2015**, *48*, 119-127.
(83) Fu, Q.; Bao, X. Surface chemistry and catalysis confined under two-dimensional materials. *Chem. Soc. Rev.* **2017**, *46*, 1842-1874.
(84) Hu, S.; Lozada-Hidalgo, M.; Wang, F. C.; Mishchenko, A.; Schedin, F.; Nair, R. R.; Hill, E. W.; Boukhvalov, D. W.; Katsnelson, M. I.; Dryfe, R. A. *et al.* Proton transport through one-atom-thick crystals. *Nature* **2014**, *516*, 227-230.
(85) O'Hern, S. C.; Boutilier, M. S.; Idrobo, J. C.; Song, Y.; Kong, J.; Laoui, T.; Atieh, M.; Karnik, R. Selective ionic transport through tunable subnanometer pores in single-layer graphene membranes. *Nano Lett.* **2014**, *14*, 1234-1241.
(86) Achtyl, J. L.; Unocic, R. R.; Xu, L.; Cai, Y.; Raju, M.; Zhang, W.; Sacci, R. L.; Vlassiouk, I. V.; Fulvio, P. F.; Ganesh, P. *et al.* Aqueous proton transfer across single-layer graphene. *Nat. Commun.* **2015**, *6*, 6539.
(87) Huang, L.; Zhang, M.; Li, C.; Shi, G. Graphene-Based Membranes for Molecular Separation. *J. Phys. Chem. Lett.* **2015**, *6*, 2806-2815.
(88) Wang, L.; Drahushuk, L. W.; Cantley, L.; Koenig, S. P.; Liu, X.; Pellegrino, J.; Strano, M. S.; Bunch, J. S. Molecular valves for controlling gas phase transport made from discrete angstrom-sized pores in graphene. *Nat. Nanotechnol.* **2015**, *10*, 785-790.
(89) Wang, L.; Boutilier, M. S. H.; Kidambi, P. R.; Jang, D.; Hadjiconstantinou, N. G.; Karnik, R. Fundamental transport mechanisms, fabrication and potential applications of nanoporous atomically thin membranes. *Nat. Nanotechnol.* **2017**, *12*, 509-522.
(90) Chaturvedi, P.; Vlassiouk, I. V.; Cullen, D. A.; Rondinone, A. J.; Lavrik, N. V.; Smirnov, S. N. Ionic Conductance through Graphene: Assessing Its Applicability as a Proton Selective Membrane. *ACS Nano* **2019**, *13*, 12109-12119.
(91) Li, W.; Li, Y.; Xu, K. Facile, electrochemical chlorination of graphene from an aqueous NaCl solution. *Nano Lett.* **2021**, *21*, 1150-1155.
(92) Cao, P. G.; Xu, K.; Varghese, J. O.; Heath, J. R. Atomic force microscopy characterization of room-temperature adlayers of small organic molecules through graphene templating. *J. Am. Chem. Soc.* **2011**, *133*, 2334-2337.
(93) Cao, P. G.; Xu, K.; Varghese, J. O.; Heath, J. R. The microscopic structure of adsorbed water on hydrophobic surfaces under ambient conditions. *Nano Lett.* **2011**, *11*, 5581-5586.
(94) Vasu, K. S.; Prestat, E.; Abraham, J.; Dix, J.; Kashtiban, R. J.; Beheshtian, J.; Sloan, J.; Carbone, P.; Neek-Amal, M.; Haigh, S. J. *et al.* Van der Waals pressure and its effect on trapped interlayer molecules. *Nat. Commun.* **2016**, *7*, 12168.
(95) Coleman, V. A.; Knut, R.; Karis, O.; Grennberg, H.; Jansson, U.; Quinlan, R.; Holloway, B. C.; Sanyal, B.; Eriksson, O. Defect formation in graphene nanosheets by acid treatment: an x-ray absorption spectroscopy and density functional theory study. *J. Phys. D-Appl. Phys.* **2008**, *41*, 062001.
(96) Bouleghlimat, E.; Davies, P. R.; Davies, R. J.; Howarth, R.; Kulhavy, J.; Morgan, D. J. The effect of acid treatment on the surface chemistry and topography of graphite. *Carbon* **2013**, *61*, 124-133.

(97) Kim, S. J.; Park, S. J.; Kim, H. Y.; Jang, G. S.; Park, D. J.; Park, J.-Y.; Lee, S.; Ahn, Y. H. Characterization of chemical doping of graphene by in-situ Raman spectroscopy. *Appl. Phys. Lett.* **2016**, *108*, 203111.
(98) Ahn, G.; Ryu, S. Reversible sulfuric acid doping of graphene probed by in-situ multi-wavelength Raman spectroscopy. *Carbon* **2018**, *138*, 257-263.
(99) Hong, Y.; Wang, S.; Li, Q.; Song, X.; Wang, Z.; Zhang, X.; Besenbacher, F.; Dong, M. Interfacial icelike water local doping of graphene. *Nanoscale* **2019**, *11*, 19334-19340.
(100) Liang, X.; Sperling, B. A.; Calizo, I.; Cheng, G.; Hacker, C. A.; Zhang, Q.; Obeng, Y.; Yan, K.; Peng, H.; Li, Q. *et al.* Toward Clean and Crackless Transfer of Graphene. *ACS Nano* **2011**, *5*, 9144-9153.
(101) Li, W.; Li, Y.; Xu, K. Azidated graphene: direct azidation from monolayers, click chemistry, and bulk production from graphite. *Nano Lett.* **2020**, *20*, 534-539.
(102) Yeh, P. *Optical Waves in Layered Media*; Wiley: Hoboken, NJ, 2005.
(103) Ambrosi, A.; Chua, C. K.; Latiff, N. M.; Loo, A. H.; Wong, C. H. A.; Eng, A. Y. S.; Bonanni, A.; Pumera, M. Graphene and its electrochemistry - an update. *Chem. Soc. Rev.* **2016**, *45*, 2458-2493.
(104) Bottari, G.; Herranz, M. A.; Wibmer, L.; Volland, M.; Rodriguez-Perez, L.; Guldi, D. M.; Hirsch, A.; Martin, N.; D'Souza, F.; Torres, T. Chemical functionalization and characterization of graphene-based materials. *Chem. Soc. Rev.* **2017**, *46*, 4464-4500.
(105) Chen, H. W.; Li, C.; Qu, L. T. Solution electrochemical approach to functionalized graphene: History, progress and challenges. *Carbon* **2018**, *140*, 41-56.
(106) Greenwood, J.; Phan, T. H.; Fujita, Y.; Li, Z.; Lvasenko, O.; Vanderlinden, W.; Van Gorp, H.; Frederickx, W.; Lu, G.; Tahara, K. *et al.* Covalent modification of graphene and graphite using diazonium chemistry: tunable grafting and nanomanipulation. *ACS Nano* **2015**, *9*, 5520-5535.
(107) Salvio, R.; Krabbenborg, S.; Naber, W. J. M.; Velders, A. H.; Reinhoudt, D. N.; van der Wiel, W. G. The formation of large-area conducting graphene-like platelets. *Chem.-Eur. J.* **2009**, *15*, 8235-8240.
(108) Eigler, S.; Hu, Y. C.; Ishii, Y.; Hirsch, A. Controlled functionalization of graphene oxide with sodium azide. *Nanoscale* **2013**, *5*, 12136-12139.
(109) Halbig, C. E.; Rietsch, P.; Eigler, S. Towards the synthesis of graphene azide from graphene oxide. *Molecules* **2015**, *20*, 21050-21057.
(110) Walter, T. H.; Bancroft, E. E.; McIntire, G. L.; Davis, E. R.; Gierasch, L. M.; Blount, H. N. Spin trapping in heterogeneous electron transfer processes. *Can. J. Chem.* **1982**, *60*, 1621-1636.
(111) Alfassi, Z. B.; Harriman, A.; Huie, R. E.; Mosseri, S.; Neta, P. The redox potential of the azide/azidyl couple. *J. Phys. Chem.* **1987**, *91*, 2120-2122.
(112) Meldal, M.; Tornoe, C. W. Cu-catalyzed azide-alkyne cycloaddition. *Chem. Rev.* **2008**, *108*, 2952-3015.
(113) Jewett, J. C.; Bertozzi, C. R. Cu-free click cycloaddition reactions in chemical biology. *Chem. Soc. Rev.* **2010**, *39*, 1272-1279.
(114) Escorihuela, J.; Marcelis, A. T. M.; Zuilhof, H. Metal-free click chemistry reactions on surfaces. *Adv. Mater. Interfaces* **2015**, *2*, 1500135.
(115) Wollman, E. W.; Kang, D.; Frisbie, C. D.; Lorkovic, I. M.; Wrighton, M. S. Photosensitive self-assembled monolayers on gold: photochemistry of surface-confined aryl azide and cyclopentadienylmanganese tricarbonyl. *J. Am. Chem. Soc.* **1994**, *116*, 4395-4404.

(116) Collman, J. P.; Devaraj, N. K.; Eberspacher, T. P. A.; Chidsey, C. E. D. Mixed azide-terminated monolayers: A platform for modifying electrode surfaces. *Langmuir* **2006**, *22*, 2457-2464.
(117) Daugaard, A. E.; Hvilsted, S.; Hansen, T. S.; Larsen, N. B. Conductive polymer functionalization by click chemistry. *Macromolecules* **2008**, *41*, 4321-4327.
(118) Sharma, J.; Gora, T.; Rimstidt, J. D.; Staley, R. X-ray photoelectron spectra of the alkali azides. *Chem. Phys. Lett.* **1972**, *15*, 232-235.
(119) Giesbers, M.; Marcelis, A. T.; Zuilhof, H. Simulation of XPS C1s spectra of organic monolayers by quantum chemical methods. *Langmuir* **2013**, *29*, 4782-4788.
(120) Zorn, G.; Liu, L. H.; Arnadottir, L.; Wang, H.; Gamble, L. J.; Castner, D. G.; Yan, M. D. X-ray photoelectron spectroscopy investigation of the nitrogen species in photoactive perfluorophenylazide-modified surfaces. *J. Phys. Chem. C* **2014**, *118*, 376-383.
(121) Delamar, M.; Hitmi, R.; Pinson, J.; Savéant, J. M. Covalent modification of carbon surfaces by grafting of functionalized aryl radicals produced from electrochemical reduction of diazonium salts. *J. Am. Chem. Soc.* **1992**, *114*, 5883-5884.
(122) Allongue, P.; Delamar, M.; Desbat, B.; Fagebaume, O.; Hitmi, R.; Pinson, J.; Savéant, J.-M. Covalent modification of carbon surfaces by aryl radicals generated from the electrochemical reduction of diazonium salts. *J. Am. Chem. Soc.* **1997**, *119*, 201-207.
(123) Andrieux, C. P.; Gonzalez, F.; Savéant, J.-M. Derivatization of carbon surfaces by anodic oxidation of arylacetates. Electrochemical manipulation of the grafted films. *J. Am. Chem. Soc.* **1997**, *119*, 4292-4300.
(124) Zhou, L.; Zhou, L.; Yang, M.; Wu, D.; Liao, L.; Yan, K.; Xie, Q.; Liu, Z.; Peng, H.; Liu, Z. Free radical reactions in two dimensions: a case study on photochlorination of graphene. *Small* **2013**, *9*, 1388-96.
(125) Yang, S.; Bruller, S.; Wu, Z. S.; Liu, Z. Y.; Parvez, K.; Dong, R. H.; Richard, F.; Samori, P.; Feng, X. L.; Mullen, K. Organic radical-assisted electrochemical exfoliation for the scalable production of high-quality graphene. *J. Am. Chem. Soc.* **2015**, *137*, 13927-13932.
(126) Behar, D.; Fessenden, R. W. Electron spin resonance studies of inorganic radicals in irradiated aqueous solutions. II. Radical trapping with nitromethane. *J. Phys. Chem.* **1972**, *76*, 1710-1721.
(127) Li, Y.; Wang, J.; Cai, C. Rapid grafting of azido-labeled oligo(ethylene glycol)s onto an alkynyl-terminated monolayer on nonoxidized silicon via microwave-assisted "click" reaction. *Langmuir* **2011**, *27*, 2437-45.
(128) Kim, J.; Cote, L. J.; Kim, F.; Huang, J. X. Visualizing graphene based sheets by fluorescence quenching microscopy. *J. Am. Chem. Soc.* **2010**, *132*, 260-267.
(129) Chen, F.; Qing, Q.; Xia, J. L.; Tao, N. J. Graphene field-effect transistors: electrochemical gating, interfacial capacitance, and biosensing applications. *Chem.-Asian J.* **2010**, *5*, 2144-2153.
(130) Hansch, C.; Leo, A.; Taft, R. W. A survey of Hammett substituent constants and resonance and field parameters. *Chem. Rev.* **1991**, *91*, 165-195.
(131) Lord, S. J.; Lee, H. L. D.; Samuel, R.; Weber, R.; Liu, N.; Conley, N. R.; Thompson, M. A.; Twieg, R. J.; Moerner, W. E. Azido push-pull fluorogens photoactivate to produce bright fluorescent labels. *J. Phys. Chem. B* **2010**, *114*, 14157-14167.
(132) Wu, J.; Xie, L. M.; Li, Y. G.; Wang, H. L.; Ouyang, Y. J.; Guo, J.; Dai, H. J. Controlled chlorine plasma reaction for noninvasive graphene doping. *J. Am. Chem. Soc.* **2011**, *133*, 19668-19671.

(133) Zhang, X.; Hsu, A.; Wang, H.; Song, Y.; Kong, J.; Dresselhaus, M. S.; Palacios, T. Impact of chlorine functionalization on high-mobility chemical vapor deposition grown graphene. *ACS Nano* **2013**, *7*, 7262-7270.
(134) Zhang, X.; Schiros, T.; Nordlund, D.; Shin, Y. C.; Kong, J.; Dresselhaus, M.; Palacios, T. X-ray spectroscopic investigation of chlorinated graphene: surface structure and electronic effects. *Adv. Funct. Mater.* **2015**, *25*, 4163-4169.
(135) Pham, V. P.; Kim, K. H.; Jeon, M. H.; Lee, S. H.; Kim, K. N.; Yeom, G. Y. Low damage pre-doping on CVD graphene/Cu using a chlorine inductively coupled plasma. *Carbon* **2015**, *95*, 664-671.
(136) Copetti, G.; Nunes, E. H.; Rolim, G. K.; Soares, G. V.; Correa, S. A.; Weibel, D. E.; Radtke, C. Reversibility of graphene photochlorination. *J. Phys. Chem. C* **2018**, *122*, 16333-16338.
(137) Abdelkader, A. M.; Cooper, A. J.; Dryfe, R. A. W.; Kinloch, I. A. How to get between the sheets: a review of recent works on the electrochemical exfoliation of graphene materials from bulk graphite. *Nanoscale* **2015**, *7*, 6944-6956.
(138) Parvez, K.; Wu, Z. S.; Li, R.; Liu, X.; Graf, R.; Feng, X.; Mullen, K. Exfoliation of graphite into graphene in aqueous solutions of inorganic salts. *J. Am. Chem. Soc.* **2014**, *136*, 6083-6091.
(139) Brase, S.; Gil, C.; Knepper, K.; Zimmermann, V. Organic azides: An exploding diversity of a unique class of compounds. *Angew. Chem.-Int. Edit.* **2005**, *44*, 5188-5240.
(140) Horcas, I.; Fernández, R.; Gómez-Rodríguez, J. M.; Colchero, J.; Gómez-Herrero, J.; Baro, A. M. WSXM: A software for scanning probe microscopy and a tool for nanotechnology. *Rev. Sci. Instrum.* **2007**, *78*, 013705.
(141) Nair, R. R.; Ren, W.; Jalil, R.; Riaz, I.; Kravets, V. G.; Britnell, L.; Blake, P.; Schedin, F.; Mayorov, A. S.; Yuan, S. *et al.* Fluorographene: a two-dimensional counterpart of Teflon. *Small* **2010**, *6*, 2877-2884.
(142) Chen, D.; Tang, L. H.; Li, J. H. Graphene-based materials in electrochemistry. *Chem. Soc. Rev.* **2010**, *39*, 3157-3180.
(143) Karlický, F.; Datta, K. K. R.; Otyepka, M.; Zbořil, R. Halogenated graphenes: rapidly growing family of graphene derivatives. *ACS Nano* **2013**, *7*, 6434-6464.
(144) Ambrosi, A.; Chua, C. K.; Bonanni, A.; Pumera, M. Electrochemistry of graphene and related materials. *Chem. Rev.* **2014**, *114*, 7150-7188.
(145) Sturala, J.; Luxa, J.; Pumera, M.; Sofer, Z. Chemistry of graphene derivatives: synthesis, applications, and perspectives. *Chem.-Eur. J.* **2018**, *24*, 5992-6006.
(146) Li, B.; Zhou, L.; Wu, D.; Peng, H.; Yan, K.; Zhou, Y.; Liu, Z. Photochemical chlorination of graphene. *ACS Nano* **2011**, *5*, 5957-5961.
(147) Zhou, L.; Zhou, L.; Yang, M.; Wu, D.; Liao, L.; Yan, K.; Xie, Q.; Liu, Z.; Peng, H.; Liu, Z. Free radical reactions in two dimensions: a case study on photochlorination of graphene. *Small* **2013**, *9*, 1388-1396.
(148) Hossain, M. Z.; Razak, M. B. A.; Noritake, H.; Shiozawa, Y.; Yoshimoto, S.; Mukai, K.; Koitaya, T.; Yoshinobu, J.; Hosaka, S. Monolayer selective methylation of epitaxial graphene on SiC(0001) through two-step chlorination-alkylation reactions. *J. Phys. Chem. C* **2014**, *118*, 22096-22101.
(149) Copetti, G.; Nunes, E. H.; Rolim, G. K.; Soares, G. V.; Correa, S. A.; Weibel, D. E.; Radtke, C. Reversibility of graphene photochlorination. *J. Phys. Chem. C* **2018**, *122*, 16333-16338.

(150) Gopalakrishnan, K.; Subrahmanyam, K. S.; Kumar, P.; Govindaraj, A.; Rao, C. N. R. Reversible chemical storage of halogens in few-layer graphene. *RSC Adv.* **2012**, *2*, 1605-1608.
(151) Zheng, J.; Liu, H. T.; Wu, B.; Di, C. A.; Guo, Y. L.; Wu, T.; Yu, G.; Liu, Y. Q.; Zhu, D. B. Production of graphite chloride and bromide using microwave sparks. *Sci. Rep.* **2012**, *2*, 662.
(152) Poh, H. L.; Simek, P.; Sofer, Z.; Pumera, M. Halogenation of graphene with chlorine, bromine, or iodine by exfoliation in a halogen atmosphere. *Chem. Eur. J.* **2013**, *19*, 2655-2662.
(153) Li, W.; Tan, C.; Lowe, M. A.; Abruña, H. D.; Ralph, D. C. Electrochemistry of individual monolayer graphene sheets. *ACS Nano* **2011**, *5*, 2264-2270.
(154) Valota, A. T.; Kinloch, I. A.; Novoselov, K. S.; Casiraghi, C.; Eckmann, A.; Hill, E. W.; Dryfe, R. A. W. Electrochemical behavior of monolayer and bilayer graphene. *ACS Nano* **2011**, *5*, 8809-8815.
(155) Ejigu, A.; Kinloch, I. A.; Dryfe, R. A. Single stage simultaneous electrochemical exfoliation and functionalization of graphene. *ACS Appl. Mater. Interfaces* **2017**, *9*, 710-721.
(156) Hubert, J.; Poleunis, C.; Delcorte, A.; Laha, P.; Bossert, J.; Lambeets, S.; Ozkan, A.; Bertrand, P.; Terryn, H.; Reniers, F. Plasma polymerization of C_4Cl_6 and $C_2H_2Cl_4$ at atmospheric pressure. *Polymer* **2013**, *54*, 4085-4092.
(157) Jayson, G. G.; Parsons, B. J.; Swallo, A. J. Some simple, highly reactive, inorganic chlorine derivatives in aqueous solution. *J. Chem. Soc., Faraday Trans. 1* **1973**, *69*, 1597-1607.
(158) Liao, C.-H.; Kang, S.-F.; Wu, F.-A. Hydroxyl radical scavenging role of chloride and bicarbonate ions in the H_2O_2/UV process. *Chemosphere* **2001**, *44*, 1193-1200.
(159) Knirsch, K. C.; Schäfer, R. A.; Hauke, F.; Hirsch, A. Mono- and ditopic bisfunctionalization of graphene. *Angew. Chem.-Int. Edit.* **2016**, *55*, 5861-5864.
(160) Chronopoulos, D. D.; Medved, M.; Potsi, G.; Tomanec, O.; Scheibe, M.; Otyepka, M. Tunable one-step double functionalization of graphene based on fluorographene chemistry. *Chem. Commun.* **2020**, *56*, 1936-1939.
(161) Dehnicke, K. The chemistry of the halogen azides. In *Advances in Inorganic Chemistry*; Emeléus, H. J., Sharpe, A. G., Eds.; Academic Press, 1983; Vol. 26; pp 169-200.
(162) Zehavi, D.; Rabani, J. Oxidation of aqueous bromide ions by hydroxyl radicals. Pulse radiolytic investigation. *J. Phys. Chem.* **1972**, *76*, 312-319.
(163) Thomas, J. K. Rates of reaction of the hydroxyl radical. *Trans. Faraday Soc.* **1965**, *61*, 702-707.
(164) Karlicky, F.; Zboril, R.; Otyepka, M. Band gaps and structural properties of graphene halides and their derivates: a hybrid functional study with localized orbital basis sets. *J. Chem. Phys.* **2012**, *137*, 034709.
(165) Jankovský, O.; Šimek, P.; Klimová, K.; Sedmidubský, D.; Matějková, S.; Pumera, M.; Sofer, Z. Towards graphene bromide: bromination of graphite oxide. *Nanoscale* **2014**, *6*, 6065-6074.
(166) Au, H.; Rubio, N.; Shaffer, M. S. P. Brominated graphene as a versatile precursor for multifunctional grafting. *Chem. Sci.* **2018**, *9*, 209-217.
(167) Hofmann, S. *Auger- and X-Ray Photoelectron Spectroscopy in Materials Science*; Springer Berlin: Heidelberg, 2013.
(168) Liao, L.; Peng, H.; Liu, Z. Chemistry makes graphene beyond graphene. *J. Am. Chem. Soc.* **2014**, *136*, 12194-12200.
(169) Plutnar, J.; Pumera, M.; Sofer, Z. The chemistry of CVD graphene. *J. Mater. Chem. C* **2018**, *6*, 6082-6101.

(170) Daukiya, L.; Seibel, J.; De Feyter, S. Chemical modification of 2D materials using molecules and assemblies of molecules. *Adv. Phys.: X* **2019**, *4*, 1625723.
(171) Nandanapalli, K. R.; Mudusu, D.; Lee, S. Functionalization of graphene layers and advancements in device applications. *Carbon* **2019**, *152*, 954-985.
(172) Jeong, J. H.; Kang, S.; Kim, N.; Joshi, R.; Lee, G.-H. Recent trends in covalent functionalization of 2D materials. *Phys. Chem. Chem. Phys.* **2022**, *24*, 10684-10711.
(173) Zhang, L.; Diao, S.; Nie, Y.; Yan, K.; Liu, N.; Dai, B.; Xie, Q.; Reina, A.; Kong, J.; Liu, Z. Photocatalytic Patterning and Modification of Graphene. *J. Am. Chem. Soc.* **2011**, *133*, 2706-2713.
(174) Lee, W. H.; Suk, J. W.; Chou, H.; Lee, J.; Hao, Y.; Wu, Y.; Piner, R.; Akinwande, D.; Kim, K. S.; Ruoff, R. S. Selective-Area Fluorination of Graphene with Fluoropolymer and Laser Irradiation. *Nano Lett.* **2012**, *12*, 2374-2378.
(175) Kirkman, P. M.; Güell, A. G.; Cuharuc, A. S.; Unwin, P. R. Spatial and Temporal Control of the Diazonium Modification of sp^2 Carbon Surfaces. *J. Am. Chem. Soc.* **2014**, *136*, 36-39.
(176) Valenta, L.; Kovaricek, P.; Vales, V.; Bastl, Z.; Drogowska, K. A.; Verhagen, T. A.; Cibulka, R.; Kalbac, M. Spatially Resolved Covalent Functionalization Patterns on Graphene. *Angew. Chem.-Int. Edit.* **2019**, *58*, 1324-1328.
(177) Wei, T.; Al-Fogra, S.; Hauke, F.; Hirsch, A. Direct Laser Writing on Graphene with Unprecedented Efficiency of Covalent Two-Dimensional Functionalization. *J. Am. Chem. Soc.* **2020**, *142*, 21926-21931.
(178) Edelthalhammer, K. F.; Dasler, D.; Jurkiewicz, L.; Nagel, T.; Al-Fogra, S.; Hauke, F.; Hirsch, A. Covalent 2D-Engineering of Graphene by Spatially Resolved Laser Writing/Reading/Erasing. *Angew. Chem.-Int. Edit.* **2020**, *59*, 23329-23334.
(179) Bao, L.; Zhao, B.; Yang, B.; Halik, M.; Hauke, F.; Hirsch, A. Hypervalent Iodine Compounds as Versatile Reagents for Extremely Efficient and Reversible Patterning of Graphene with Nanoscale Precision. *Adv. Mater.* **2021**, *33*, e2101653.
(180) Rodriguez Gonzalez, M. C.; Leonhardt, A.; Stadler, H.; Eyley, S.; Thielemans, W.; De Gendt, S.; Mali, K. S.; De Feyter, S. Multicomponent Covalent Chemical Patterning of Graphene. *ACS Nano* **2021**, *15*, 10618-10627.
(181) Wei, T.; Hauke, F.; Hirsch, A. Evolution of Graphene Patterning: From Dimension Regulation to Molecular Engineering. *Adv. Mater.* **2021**, *33*, 2104060.
(182) Wei, T.; Liu, X.; Kohring, M.; Al-Fogra, S.; Moritz, M.; Hemmeter, D.; Paap, U.; Papp, C.; Steinrück, H.-P.; Bachmann, J. *et al.* Molecular Stacking on Graphene. *Angew. Chem.-Int. Edit.* **2022**, *61*, e202201169.
(183) Koike, T.; Akita, M. Visible-light radical reaction designed by Ru- and Ir-based photoredox catalysis. *Inorg. Chem. Front.* **2014**, *1*, 562-576.
(184) Shaw, M. H.; Twilton, J.; MacMillan, D. W. C. Photoredox Catalysis in Organic Chemistry. *J. Org. Chem.* **2016**, *81*, 6898-6926.
(185) McAtee, R. C.; McClain, E. J.; Stephenson, C. R. J. Illuminating Photoredox Catalysis. *Trends Chem.* **2019**, *1*, 111-125.
(186) Tay, N. E. S.; Lehnherr, D.; Rovis, T. Photons or Electrons? A Critical Comparison of Electrochemistry and Photoredox Catalysis for Organic Synthesis. *Chem. Rev.* **2022**, *122*, 2487-2649.

(187) Kwon, K.; Simons, R. T.; Nandakumar, M.; Roizen, J. L. Strategies to Generate Nitrogen-centered Radicals That May Rely on Photoredox Catalysis: Development in Reaction Methodology and Applications in Organic Synthesis. *Chem. Rev.* **2022**, *122*, 2353-2428.
(188) DeFelippis, M. R.; Faraggi, M.; Klapper, M. H. Redox potentials of the azide and dithiocyanate radicals. *J. Phys. Chem.* **1990**, *94*, 2420-2424.
(189) Kim, Y. T.; Collins, R. W.; Vedam, K.; Allara, D. L. Real Time Spectroscopic Ellipsometry: In Situ Characterization of Pyrrole Electropolymerization. *Journal of The Electrochemical Society* **1991**, *138*, 3266.
(190) Sadki, S.; Schottland, P.; Brodie, N.; Sabouraud, G. The mechanisms of pyrrole electropolymerization. *Chem. Soc. Rev.* **2000**, *29*, 283-293.
(191) Davies, A.; Audette, P.; Farrow, B.; Hassan, F.; Chen, Z.; Choi, J.-Y.; Yu, A. Graphene-Based Flexible Supercapacitors: Pulse-Electropolymerization of Polypyrrole on Free-Standing Graphene Films. *The Journal of Physical Chemistry C* **2011**, *115*, 17612-17620.
(192) Wolfart, F.; Dubal, D. P.; Vidotti, M.; Holze, R.; Gomez-Romero, P. Electrochemical supercapacitive properties of polypyrrole thin films: influence of the electropolymerization methods. *J. Solid State Electrochem.* **2016**, *20*, 901-910.
(193) Bose, C. S. C.; Basak, S.; Rajeshwar, K. Electrochemistry of poly(pyrrole chloride) films: a study of polymerization efficiency, ion transport during redox and doping level assay by electrochemical quartz crystal microgravimetry, pH and ion-selective electrode measurements. *The Journal of Physical Chemistry* **1992**, *96*, 9899-9906.
(194) Kim, S.; Jang, L. K.; Park, H. S.; Lee, J. Y. Electrochemical deposition of conductive and adhesive polypyrrole-dopamine films. *Sci Rep* **2016**, *6*, 8.
(195) Lo, M.; Diaw, A. K. D.; Gningue-Sall, D.; Aaron, J. J.; Oturan, M. A.; Chehimi, M. M. The role of diazonium interface chemistry in the design of high performance polypyrrole-coated flexible ITO sensing electrodes. *Electrochem. Commun.* **2017**, *77*, 14-18.
(196) Hepel, M. Composite polypyrrole films switchable between the anion- and cation-exchanger states. *Electrochim. Acta* **1996**, *41*, 63-76.
(197) Yuan, Y. J.; Adeloju, S. B.; Wallace, G. G. In-situ electrochemical studies on the redox properties of polypyrrole in aqueous solutions. *Eur. Polym. J.* **1999**, *35*, 1761-1772.